

**LOW TEMPERATURE LASER-INDUCED SELECTIVE AREA
GROWTH OF COMPOUND SEMICONDUCTOR**

SUDARSAN UPPILI

**B.Sc, Madurai University, 1981
B.E, Indian Institute of Science, 1984**

**A dissertation submitted to the faculty
of the Oregon Graduate Institute of Science and Technology
in partial fulfillment for the degree
Doctor of Philosophy
in
Materials Science**

April, 1990

The dissertation "Low temperature laser-induced selective area growth of compound semiconductors" by SUDARSAN UPPILI has been examined and approved by the following Examination Committee:

Raj Solanki, Thesis Advisor
Professor

William E. Wood, Thesis Advisor
Professor

Robert M. Drosd
Adjunct Professor

Jack H. Devletian
Professor

I dedicate this dissertation to my father

ACKNOWLEDGEMENTS

I am most grateful to my advisors, Professors Raj Solanki and William E. Wood for encouraging me to undertake this research. Professor Solanki equipped me initially with a delight for laser chemical processing, then guided my research from start to finish. I owe to him a debt of gratitude much greater than I have paid. My appreciation goes to Professor Wood for allowing me to work on an inter-departmental project with Applied Physics and Electrical Engineering department.

I enjoyed the discussions with Dr. Robert Drosd during the course of the work. I thank Professors Raj Solanki, William Wood, Jack Devletian, and Dr. Robert Drosd for serving on my examination committee.

I appreciate very much the invaluable co-operation I received from Nyles Cody and Taner Dosloglou. I thank Devanathan, Parthasarathy, Rajesh Digde, Vivek Dikshit, and Ajay Chadda for their assistance during compiling of this dissertation. My special thanks goes to Devanathan for keeping a constant watch on my lunch time.

Very special thanks go to my mother, brothers and sister for their years of support and encouragement.

CONTENTS

	Page
TITLE PAGE	i
APPROVAL PAGE	ii
DEDICATION	iii
ACKNOWLEDGEMENTS	iv
TABLE OF CONTENTS	v
LIST OF FIGURES	vii
ABSTRACT	xii
1 INTRODUCTION	1
2 BACKGROUND	6
2.1 Epitaxial Growth of Compound Semiconductors	6
2.2 Coherent sources for Laser-Assited Deposition	7
2.3 Approaches to Laser-Assited Deposition	10
2.4 Laser Configuration	16
2.5 Photo-Epitaxy	17
2.6 Laser-Solid Interaction	23
3 EXPERIMENT	33
3.1 Direct-Write of GaP Using Argon Ion Laser	33
3.2 Excimer Laser-Assited Epitaxy	36

4	RESULTS AND DISCUSSION	41
4.1	Argon Ion Laser-Induced Selective Growth of GaP	41
4.2	Homoepitaxial Growth	41
4.3	Selective Area Heteroepitaxy of GaP on Silicon	60
4.4	Excimer Laser-Assited Selective Epitaxy of GaP	63
4.5	Homoepitaxy of GaP	65
4.6	Observation of Pseudo-Five-Fold Symmetry in GaP	89
4.7	Heteroepitaxial Growth of GaP on GaAs	95
4.8	Comparison of Homo- and Heteroepitaxial Defect Structures	97
4.9	Formation of Periodic Structures During Excimer Laser-Induced Heteroepitaxy	107
4.10	Excimer-Laser-Induced Heating: In-situ Electrical Conductivity Measurements	126
5	CONCLUSION	150
6	FUTURE WORK	152
7	REFERENCES	155
8	BIOGRAPHICAL NOTE	164

LIST OF FIGURES

Figure		Page
1	Basic elements of an optical fiber transmission link	2
2	Typical fluorescence and free-running laser emission (a) KrF, (b) ArF, (c) XeF, and (d) XeCl	12
3	Schematic showing deposition of material onto a solid interface by pyrolytic deposition and photolytic deposition	13
4	Potential energy curves for the electronic ground state and excited states showing different cases of dissociation	15
5	Schematics of the process steps for epitaxial growth from vapor precursors	20
6	Schematic illustration of the elementary photoexcitation processes, carrier equilibration mechanisms, and electron-phonon interactions in a semiconductor exposed to laser irradiation with energy $h\nu > E_g$	27
7	Schematics of the 'direct-write' experimental arrangement	34
8	Schematics of the excimer-laser assisted deposition set-up	37
9	Schematics of TEM cross-section sample preparation procedure	40
10	SEM micrograph of polycrystalline GaP grown using a stationary argon ion laser beam	43
11	SEM micrograph of a laser deposited GaP line	43
12	Plot of area under the curve (from profilometry) vs. peak height of the deposit	45
13	Plot of epitaxial growth vs the number of scans (multiple) at 2, 3, and 4 Torr TMG partial pressures	46

14	Schematic of the projected laser profile on the spine of ridge (deposit)	48
15	Plot of calculated peak temperature profile vs deposit peak height for different laser powers	50
16	SEM micrographs of GaP deposit after (a)10 scans and (b) 35 scans	52
17	Plot of calculated peak temperature profile vs deposit peak height for different beam radii	53
18	Transmission electron diffraction of the laser deposited GaP	54
19	Schematic of the auger area scan	55
20	Auger spectrum of the laser deposited GaP at (a) area 1, (b) area 2, and (c) area 3 corresponding to Figure 19	56
21	(a) Schematic of the auger line scan and (b) auger line profiles of oxygen and carbon across the deposit	58
22	Plot of the dependence of growth rate on the laser scan speed	59
23	SEM micrograph of laser deposited GaP lines on Si	62
24	Nomarski micrograph of a GaP pad grown on Si	62
25	TEM diffraction pattern of a GaP microstructure on Si	62
26	Comparison of trimethylgallium absorption as a function of temperature. Pressure = 0.3 Torr, path length = 7.5 cm	67
27	Mass spectrum obtained during laser irradiation in the presence of tertiarybutylphosphine. Note the absence of peak at the mass 90 corresponding to TBP	67
28	Plot of growth rate of GaP versus the substrate temperature at 0.06 and 0.11 J/cm ² laser energy density	68
29	SEM micrograph of GaP deposited at 300°C	70
30	Cross-sectional TEM micrograph of the above deposit showing a cracked interface	70
31	(a) Cross-sectional TEM view of the thermally grown (500C) GaP film and (b) its corresponding transmission electron diffraction pattern showing the fine grain polycrystallinity	71

32	SEM micrograph of the laser sputtered GaP deposit	72
33	Plot of growth rate vs. laser repetition rate at laser energy density of 0.11 J/sq.cm and 500 °C	33
34	Plot of growth rate vs. laser energy density	75
35	(a) Cross-sectional TEM view of the excimer laser assisted grown (500C) GaP film showing the epitaxial growth. (b) Transmission electron diffraction pattern along [110] zone axis	76
36	Cross-sectional TEM micrograph of GaP grown away from the center of the beam spot. (b) Electron diffraction pattern along [110] zone axis showing a degree of polycrystallinity	78
37	(a) Bright field cross-sectional TEM view of the epitaxial GaP grown at 14 Torr total pressure (b) diffraction pattern along [110] zone axis	80
38	Weak beam (111) -g, g image of the film grown at 14 Torr showing the absence of twins on (111)	81
39	C-V characteristics of a p-n diode fabricated using laser epitaxy	85
40	I-V characteristics of the p-n diode	88
41	SEM Micrograph showing the elongated pyramid-like structures with polycrystalline crest	91
42	Cross-sectional TEM micrograph of a cone. The top portion is polycrystalline and the bottom is single crystal	92
43	Selected area diffraction of the lower portion of the cone	92
44	(a) Selected area diffraction pattern of the polycrystalline portion of the cone. (b) Its corresponding schematic	92
45	Schematic of TEM cross-section sample orientation	96
46	(a-d) Cross-sectional TEM micrographs showing the defect structure in homoepitaxial GaP under four different reflections: (a) 022, (b) 400, (c) 222, and (d) 222	98
47	Cros-sectional TEM micrographs showing the defect structure in GaP grown on GaAs, under four different reflections: (a) 022, (b) 400, (c) 222, and (d) 222. The arrows indicate twins	100
48	Heteroepitaxial GaP sample tilted to reveal twins	101

49	Cross-sectional TEM micrograph of GaP/GaAs tilted to reveal the interface	101
50	Plot of temperature rise for a single laser pulse on a GaP substrate at 500C	103
51	SEM micrograph of periodic ripple structures on epitaxial GaP grown on (100) GaAs	51
52	Plan-view TEM micrograph of GaP showing poor spatial coherence of the periodic structure	109
53	SEM micrograph showing the jagged ripple structure observed at the outer edge of the deposited	111
54	SEM micrograph of the faint periodic structure formed on bare GaAs	111
55	Plot of calculated laser-induced temperature rise in GaAs and corresponding depth vs. the laser energy density	114
56	Cross-sectional TEM micrograph of the ripple structures showing (a) the dislocations as indicated by the arrows and (b) the voids formed at the ripple interface	117
57	(a) Plan-view TEM of the ripples along [100] zone axis and electron diffraction patterns from the (b) rippled and (c) perturbed regions	119
58	(a) Bright field and (b) dark field TEM image of the ripple obtained using a part of the transmitted spot streak	120
59	Microdiffraction from (a) close to the edge of the ripple and (b) from the center of the ripple	122
60	Plot of chemical composition across the ripple structure	123
61	TEM micrograph showing planar defects across ripples	124
62	Schematic of the electrical conductance measurement set-up	128
63	Plot of voltage drop across the load resistor vs. time for single pulse irradiation	129
64	Conductance calibration curve	131
65	Plot of conductance vs. time for different laser pulse rates	133
66	Plot of average temperature rise vs. laser pulse rate	134

67	Plot of conductance of GaP at 190°C vs. time for different laser pulse rates	135
68	Effect of hydrogen cooling on GaP conductance	137
69	Effect of helium cooling on GaP conductance at different chamber pressures	138
70	Comparison of hydrogen and helium cooling of GaP	139
71	Comparison of presence of hydrogen, hydrogen+TBP, and hydrogen + TBP + TMG on GaP conductance	141
72	Effect of helium window purge at zero bias	143
73	Effect of laser energy density at zero bias	145
74	Effect of laser pulse rate at zero bias	146
75	Effect of substrate temperature at zero bias	147

ABSTRACT

Low Temperature Laser-Induced Selective Area Growth of Compound Semiconductor

Sudarsan Uppili, Ph.D.
Oregon Graduate Institute of Science and Technology, 1990

Supervising Professors: Raj Solanki and William E. Wood

Laser-induced epitaxial growth of gallium phosphide has been investigated as a low temperature, spatially selective process using both pyrolytic and photo-lytic reaction. A focussed beam from an argon ion laser operating at 514.5 nm was used to 'direct-write' epitaxial microstructures of homoepitaxial GaP using a pyrolytic process. The precursors were trimethylgallium (TMG) and tertiarybutylphosphine (TBP), a new phosphorous donor. Dependence of the epitaxial growth on several deposition parameters was examined.

An ArF excimer laser has also been used to achieve homoepitaxy and heteroepitaxy of gallium phosphide on gallium arsenide at 500°C using TMG and TBP as the precursor gases. Dependence of homoepitaxial growth of GaP on several parameters is examined. The crystalline properties of the film were determined using transmission electron microscopy (TEM). It was found that at 500°C, in the presence of laser radiation, higher growth rate and superior crystalline properties were achieved compared to purely thermal metalorganic chemical vapor deposition under the same conditions. Electrical properties of p-n diodes fabricated via Zn doping have also been examined.

Defect structures in excimer laser-assisted epitaxial GaP on (100) GaP and

(100) GaAs have been examined using TEM. It was found that that the dominant defect structures in homoepitaxy were dislocations and stacking faults whereas the major defects in heteroepitaxy were twins. Differential plastic deformation-induced stresses are believed to be responsible for the high density of twins in heteroepitaxy.

Periodic structures were obtained using nominally unpolarized excimer laser radiation, during heteroepitaxial growth of GaP on GaAs. Both crystalline properties and chemical composition of these structures have been examined. The strong periodic structure observed on GaP grown on GaAs was attributed to the initial melting of the substrate during film growth. Microanalysis showed modulation in composition in the ripple structure resulting from the thermal variation caused by the optical interference during growth.

Electrical conductivity measurements of GaP during pulsed laser irradiation indicated that in the absence of gases, there was appreciable heating of the semiconductor. However, a very small quantity of hydrogen or helium cooled the substrate appreciably. This suggested that the average temperature rise of the substrate was not an important factor in the temperature calculations used in the present investigation.

1. INTRODUCTION

Thin film compound semiconductor structures are used extensively in many modern electronic, magnetic, optical and energy-related devices. In these applications a detailed understanding of thin-film properties and their dependence on structure composition, and patterning is indispensable. Full control of film preparation, combined with modern physical analyses, is essential in advancing our knowledge about submicron structures in VLSI electronics and about near-surface phenomena and interfacial properties.

Interest in III-V compound semiconductors stems largely from the ability to separately manipulate energy band gap and lattice spacing by composition control. This has allowed fabrication of devices utilizing heterojunctions for the control of electron transport, e.g., the double-heterojunction (DH) lasers, high-efficiency solar cells, GaAs bipolar transistors, superlattices, and modulation-doped GaAs MESFETS.

Heteroepitaxial growth of compound semiconductors with spatial selectivity offers attractive possibilities of integrating optical devices with electronic circuits on a single wafer. An example of one such structure is shown in Fig.1, where an optical emitter or detector made of GaAs is integrated with a Si logic device on a silicon substrate. Of the conventional film growth techniques, neither Molecular Beam Epitaxy (MBE) nor Metallorganic Vapor Phase Epitaxy (MOVPE) offer any kind of growth selectivity unless the substrate is physically patterned before

OPTICAL INTERCONNECTS

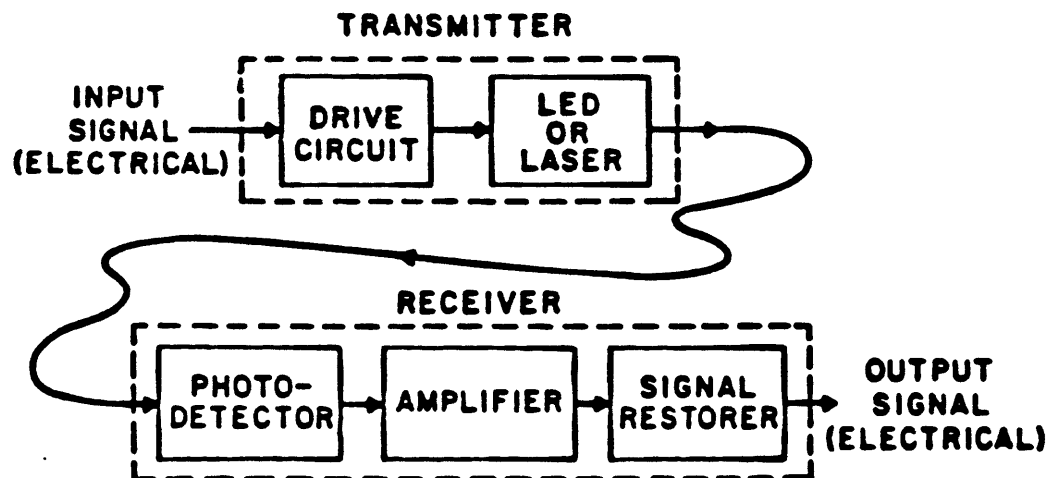
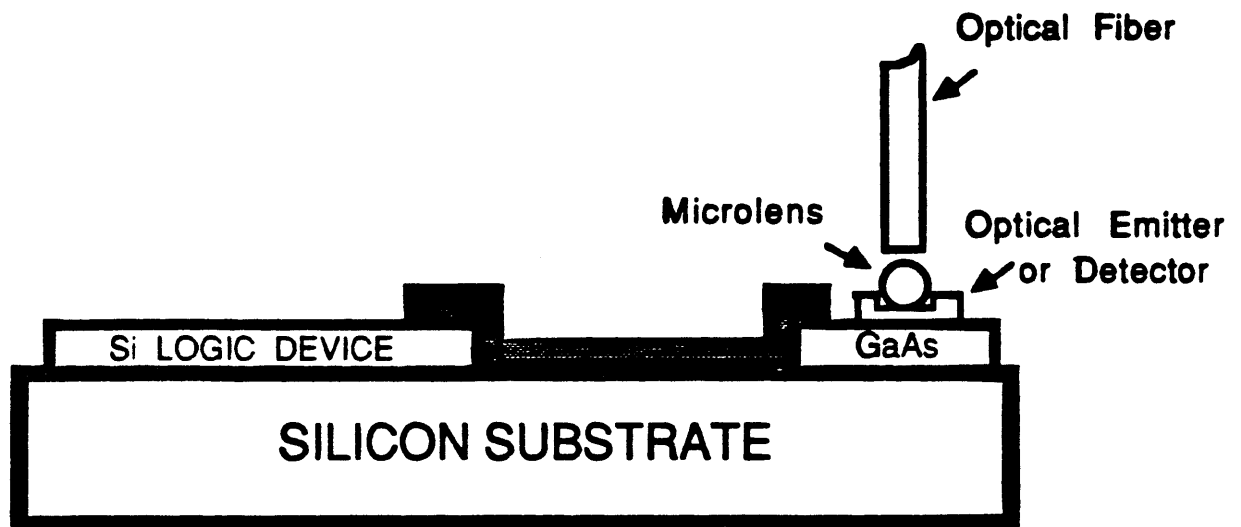


Figure 1. Basic elements of an optical fiber transmission link.

growth. This means additional processing steps before and after the growth process, leading to the introduction of undesirable defects on the substrate. Laser-stimulated microfabrication process has emerged as a unique technology that offers selective area growth of semiconductors without any extra processing steps. At present, discrete solid-state lasers comprised of double heterostructures or quantum wells are encapsulated in optoelectronic devices. These structures will require selective area etching and deposition, which could be realized with a laser based technology with either writing or projection imaging.

MOVPE of III-V compounds normally requires temperatures that are considerably above pyrolysis thresholds in order to allow sufficient surface mobility for single crystal epitaxial growth rather than polycrystalline growth. In the MOVPE heteroepitaxial growth of III-V on Si, there exists a lattice mismatch and a stress in the epitaxial film after the substrate is cooled to room temperature because of the thermal expansion mismatch between the film and the substrate. This stress also leads to severe cracking problems in the film and one way of reducing the severity of the problem is to allow epitaxial growth at low temperatures.

In the past few years, the photo-excited technique has been receiving increasing attention for low temperature processing. In this process, fewer defects are generated due to lack of excess energies, unlike plasma excitation. Chemical pathways are well defined and hence a specific radical or ion can be selectively formed by choosing the proper photon energy. Photo-excited processes can be carried out at low temperatures and are expected to be easily monitored and controlled. From an applications point of view, selective and (in many cases) non-thermal chemistry, accompanied by micrometer spatial resolution can be

applied in fabrication of microelectronic devices.

Lasers serve as the most versatile sources of monochromatic beams for initiating photochemical processes. A laser is used either as a focused beam to deliver photon energy onto a small area or as broad beam for large area processing. Unlike other beam technologies, e.g., ion and electron beams, lasers are not required to operate in a vacuum, thus providing greater flexibility in beam delivery to the reaction site. In-situ process monitoring, diagnostics, and controlling are additional capabilities in laser processing since the fluorescence due to laser-chemical interactions gives details about the reaction pathways.

In this work laser-assisted selective area growth of gallium phosphide at low temperatures was investigated. Two different techniques were studied by choosing lasers with different output characteristics. In the first part of the investigation an argon ion laser was used for direct deposition of the semiconductor, by scanning the beam on a substrate. Deposition was achieved through mostly localized pyrolysis of the precursor gases. Effect of various operating parameters on the selective area growth was investigated. The second part of the study involved the use of an excimer laser to achieve low temperature selective epitaxy. Suitable masking of the excimer laser beam can lead to selective epitaxy under optimized operating conditions. The 193nm output from the excimer laser is strongly absorbed by the metallorganic precursors resulting in their photo-dissociation. Also, there is transient heating during the pulsed laser irradiation of the substrate. Thus, the process is both photolytic and photothermal in nature. The effect of various operating parameters on the crystalline quality of the deposits was investigated using a scanning transmission electron microscope. P-N junctions were fabricated by doping GaP with zinc during growth. Junction

characteristics were analyzed using C-V and I-V plots. The electrical conductivity of GaP varies strongly with temperature because of its large band gap (2.27 eV). Hence, in order to investigate the average temperature rise of the substrate during excimer laser irradiation, the electrical conductivity of the semiconductor was also investigated.

2. BACKGROUND

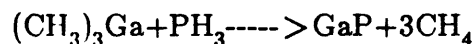
2.1: EPITAXIAL GROWTH OF COMPOUND SEMICONDUCTORS

Multilayer epitaxial structures can be grown by liquid-phase epitaxy (LPE), molecular beam epitaxy (MBE), or metalorganic vapor phase epitaxy (MOVPE). MBE has become a useful experimental tool for deposition of very high-quality films and superlattices with 10Å period. The MBE technique of single crystal film growth employs beams of atoms and molecules impinging in vacuum on a heated substrate. Single crystal substrate heating is generally required to produce enough surface mobility of the atoms to grow single crystal films in epitaxial register with the substrate. Shutters in front of the sources interrupt growth to allow layered structures to be formed. Electron diffraction may simultaneously be observed on the screen to monitor the epitaxial growth.

The other important and more widely used film growth technique for compound semiconductors is metalorganic vapor phase epitaxy (MOVPE). The control over $\text{Al}_{(1-x)}\text{Ga}_x\text{As}$ device structures afforded by a vapor deposition technique was the original driving force behind the development of MOVPE. The need for complex heterojunction devices continues to motivate the current research.

In the MOVPE process, room temperature vapors of organometallic compounds are used to transport at least one of the primary film constituents. The reactant gases decompose over a heated substrate and thus thin film growth

occur. The exact chemical decomposition pathways in MOVPE are not yet clearly understood. The nature of the reactions are in part determined by the dynamics of the gases, that is, the velocity and temperature profiles in the vicinity of the susceptor and the subsequent concentration and thermal gradients that are established. The reaction pathways, of course, are also strongly influenced by the choice of precursor chemicals. Alkyls of the group III metals, and hydrides of the group V elements usually are used as the precursor species in MOVPE. Dilute vapors of these chemicals are transported at or near room temperature to a hot zone where a pyrolysis reaction occurs. For example, the formation of Gallium Phosphide is described by



The extension of MOVPE to other alloy systems can be viewed as the generalization of the above reaction and even larger variations of the technique are possible when alternative precursors and compounds are considered as well. In some cases group V alkyls are substituted for hydrides. The group IV and VI hydrides often serve as n-type dopant sources, though the alkyl counterparts are also effective. Group II alkyls can be used as p-dopants. Photoepitaxy of III-V semiconductors is mainly as a modification to MOVPE in order to achieve either lower growth temperatures (normal pyrolytic range 600-900°C) or selective area epitaxy.

2.2: COHERENT SOURCES FOR LASER-ASSISTED DEPOSITION

A laser generally consists of two components: an active medium that produces optical gain under proper pumping conditions and an optical resonator

that consists of a pair of mirrors with specific radii of curvature and reflectivities to provide optical feedback and output coupling (1-3). The laser medium can be pumped by several excitation mechanisms such as gas discharge, optical pumping, or electrical current to induce population inversion. The parameters that characterize a laser source are its emission wavelength, spectral bandwidth, power, beam size, and beam divergence. For pulsed laser, pulse energy and pulse width are also important parameters. In the present study, two types of lasers were employed and their characteristics are discussed below

2.2.1: ION LASERS

The high-power coherent radiation in the visible and UV range from ion lasers make them the most attractive photon sources for direct-write applications. The common ion lasers are Argon(Ar), Krypton (Kr), and Xenon (Xe) with power levels varying from milliwatts to several watts. Ion lasers, as the name implies, use an ionized gas as the lasing medium maintained with an electrical discharge in a plasma. Basically they are four-level systems, where the excited states of the ions are involved in the lasing process. Excitation is a two-collision process: the first collision ionizes the atom and the second provides the necessary excitation. A visible argon laser can be frequency doubled to generate cw UV output at 257nm using the nonlinear optical crystals like ADP and KDP. However, the conversion efficiency of such a process is very low and the output is usually about 10mW. Recently, a 100mW UV frequency-doubled argon laser at 257nm has become commercially available from Spectra Physics Inc.

2.2.2: EXCIMER LASERS

Excimer lasers are both powerful and efficient optical sources utilizing electronic transitions in rare gas halide (RGH) molecules to produce intense pulses of ultraviolet light. Formed by gas phase chemical reactions in a chemical discharge, these diatomic RGH species are bound in the electronically excited upper laser level, but dissociate upon reaching the ground state, the lower laser level. This leads to nearly complete regeneration of the original gases in the laser after each discharge, allowing many output pulses to be produced from a single fill of the laser's reservoir.

The term, excited dimer, refers to a molecule that is bound only in an excited electronic state, but unbound in the ground state. As a result, emission from an excimer laser has a relatively broad emission bandwidth. This reduces the temporal coherence of radiation from an excimer laser. In addition, the presence of a large number of transverse modes in an excimer laser cavity scrambles the speckle noise that frequently is observed in images from coherent radiation.

Commercial excimer lasers provide photon energies in the UV range from 6.4 eV (ArF) to 3.5 (XeF), with typical pulsewidths from 10 to 25 nsec. They are pumped by electrical discharge or by e-beams (4) and high output is desired. UV or x-ray preionization schemes are used in excimer lasers. The pulse-to-pulse amplitude stability is typically between 3% to 5%, and pulse-to-pulse temporal jitter from a reference signal is about 2nsec.

The spectral bandwidth is an important parameter for high resolution lithography because of chromatic aberration. The spectral linewidths of free-running excimer lasers are typically several tens of nanometers. Typical fluorescence and stimulated emission spectra from free-running ArF, KrF, XeCl, and

XeF lasers are shown in Fig.2. The spectral linewidths can be narrowed using a variety of methods including intracavity etalons, prisms, gratings, and apertures.

An excimer laser is typically operated at a high Fresnel number (more than several thousands); a stable resonator would therefore produce a multimode beam with a large beam divergence. To obtain a high output energy and a low divergence, unstable resonator configurations are commonly used in excimer lasers.

2.3: APPROACHES TO LASER-ASSISTED DEPOSITION

The two techniques for laser deposition, which use gas-phase reactants are thermochemical (pyrolytic deposition) and photochemical (photolytic deposition). In the former (Fig.3a) the substrate is heated to decompose gases above it. In the latter (Fig.3b) the precursor molecules either in gas phase or adsorbed on the substrate surface are dissociated.

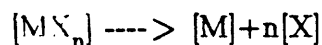
The very different laser chemical interactions in these two approaches result in different advantages and disadvantages in the pattern transfer process. For example, pyrolytic deposition can not be used when the substrate melting temperature is much lower than the temperature necessary for significant gas decomposition. However, photolytic deposition usually requires a deep UV laser source because most useful parent precursor molecules require absorption of photons with wavelengths in the 200 - 300nm range to initiate the dissociative process. This is further discussed below.

2.3.1: PYROLYTIC PROCESS

In direct writing of microstructures using pyrolytic process, a laser beam is focused through a sample cell window onto an absorbing surface. The laser

wavelength is chosen so that the light is not absorbed by the gas, but instead is used to heat only the substrate. In practice, visible light is used usually from an argon ion laser. For visible laser wavelengths, the lack of gas-phase absorption means it is possible in principle, to vary the gas density without altering the heat input to the substrate. Deposition at the surface is governed by the surface heating and the density of the reactant gases.

Laser-induced pyrolytic deposition processes under consideration are based on thermal decomposition reactions of the form:



where MX_n is the reactant gas molecule (e.g., a metal alkyl), M is the metal atom being deposited, and X is a product gas of the reaction. The process can be thought of as involving 5 steps:

1. Diffusion of reactants into the reaction zone
2. Adsorption of reactants
3. Pyro/photo activation of molecules near or at the surface
4. Surface diffusion for film growth
5. Product gas formation and desorption from the surface

At low temperatures, the rate-limiting step of the process is usually step (3); at higher temperatures, where the decomposition becomes substantial, (1) becomes the rate-limiting step.

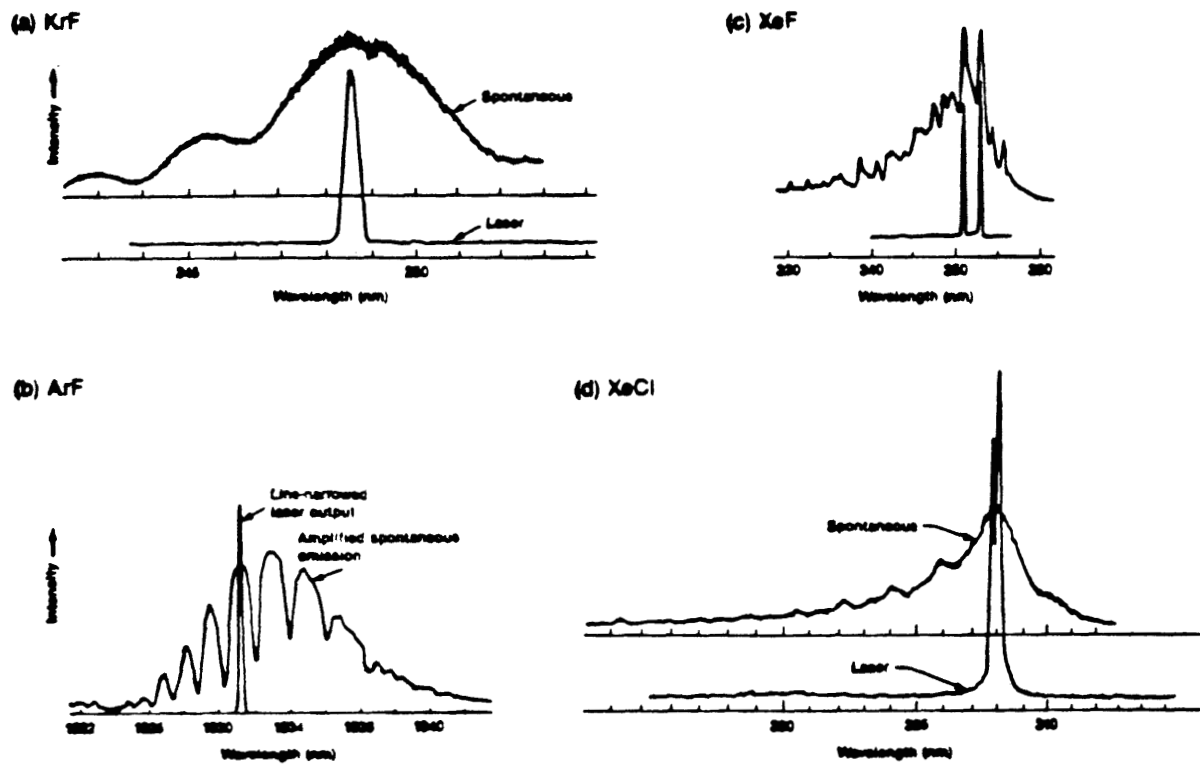


Figure 2. Typical fluorescence and free-running laser emission spectra (a) KrF, (b) ArF, (c) XeF, and (d) XeCl.

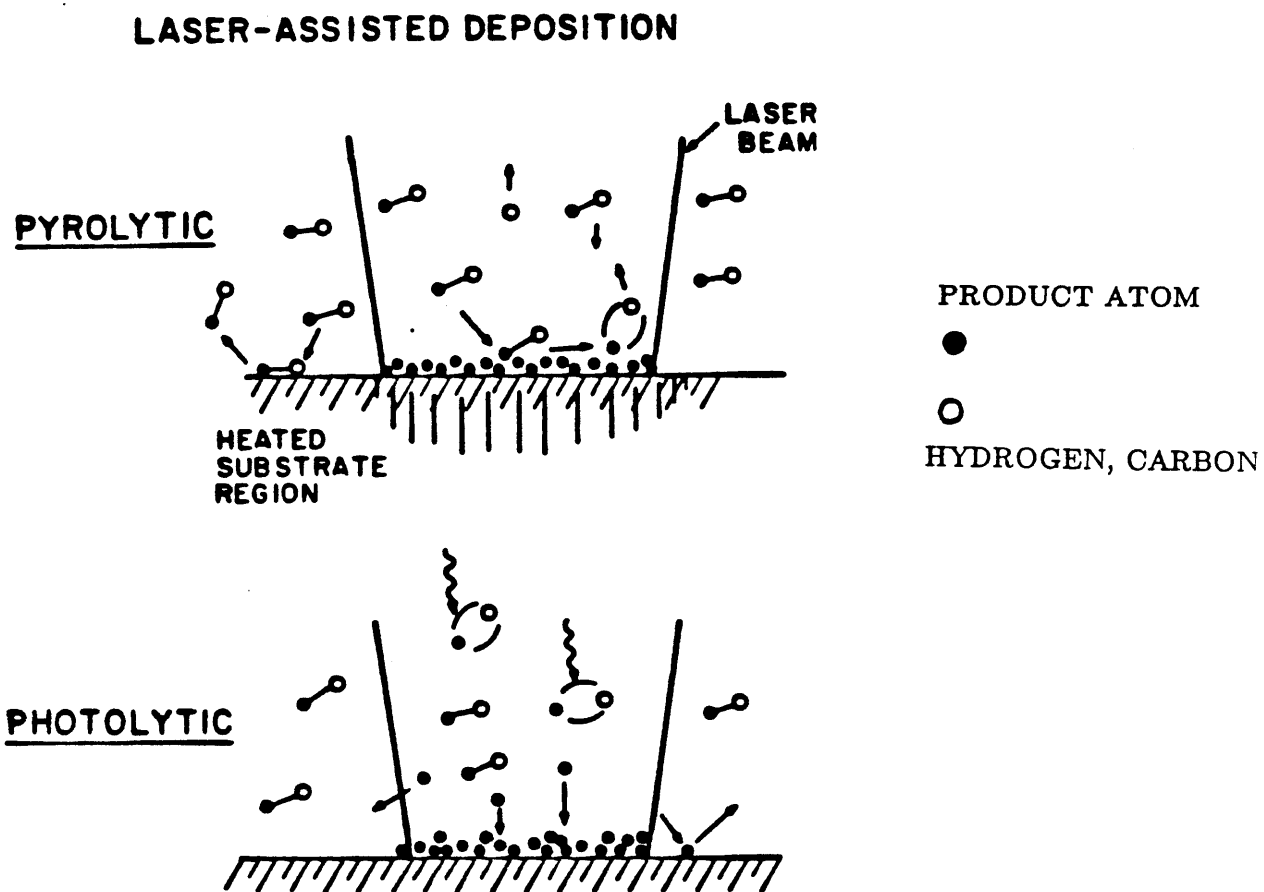


Figure 3. Schematic showing deposition of material onto a solid interface by pyrolytic deposition (top) and photolytic deposition (bottom).

2.3.2: PHOTOLYTIC PROCESS

In a photochemical deposition, an ultra-violet photon initiates a chemical reaction that causes the deposition of material on a nearby solid surface. Typically, the surfaces are chemically passive to the reactants, although in some cases chemisorption can be important. The photochemical reaction can be initiated in the gas or adsorbed phase, or in combination of both. The microstructure and spatial extent of the deposited material typically depend on the gas and surface kinetic processes and the nucleation phenomena on the solid surface.

In the photolytic process, chemical bond breaking is through dissociative electronic excitations, which are located in the visible or UV spectral range or selective multiphoton excitations by means of IR radiation.

Single or multiphoton dissociation is nonthermal in nature. Dissociative electronic excitations of molecules can be broadly classified into four cases based on single or multiphoton processes. Such processes are, in general, accompanied by simultaneous excitations of vibrational and rotational translations.

Considering four characteristic cases of single-photon excitations, the potential energy curves for ground and excited state are shown in Fig.4. According to Frank-Condon principle (5), transitions always occur vertically between maxima in $|\psi_1|^2$ and $|\psi_2|^2$ where $|\psi_i|^2$ are the corresponding vibrational wave functions in the lower and upper electronic states.

In a UV photon-precursor molecule interaction, supposing the excited level is unstable as shown in Fig.4a, the molecule dissociates within 10^{-13} and 10^{-14} sec typically. Clearly, relaxation and energy transfer between gas molecules is unlikely within the short time, taking into consideration their velocity and mean

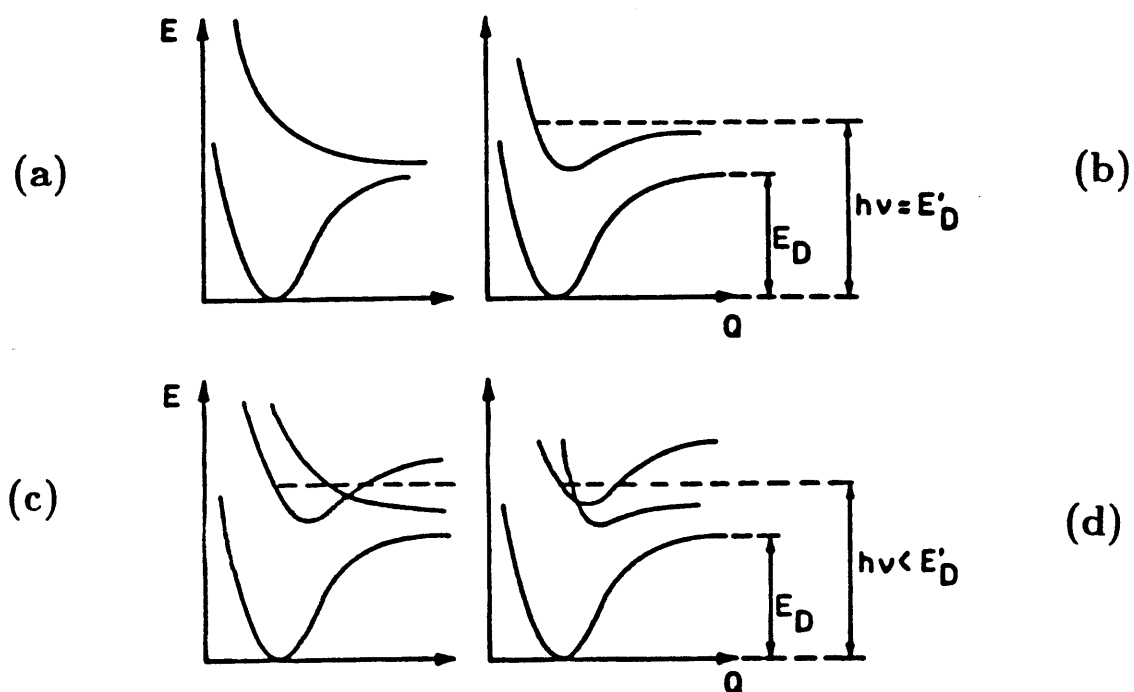


Figure 4. Potential energy curves for the electronic ground state and excited states showing different cases of dissociation. Here, E_D is the energy of dissociation and $h\nu$ the photon energy. Vibrational and rotational energy levels are not included in the curves.

free path.

In Fig.4b an excited electronic state is stable and dissociation occurs only for $h\nu > E_d$. However, in many cases dissociation is observed even for $h\nu < E_d$ and this is called spontaneous predissociation. Dissociation occurs before the dissociation limit of the initially excited state by transitions to another unstable (c) or less stable (d) electronic state. Such transitions become possible if a mixing of states near crossings of potential curves occur. Predissociation is frequent in diatomic molecules in the time scale between 10^{-6} and 10^{-12} second.

2.4: LASER CONFIGURATION

Laser photon-gas-solid interactions depend on the way the laser beam is configured with respect to the substrate. Essentially, two different experimental configurations are possible and they are chosen based on the process requirement.

2.4.1: PARALLEL ILLUMINATION

As the name implies, laser beam is in a parallel configuration with respect to the substrate. This process geometry makes use of the photolytic decomposition of the precursor gases and diffusion of gas species to the substrate for film growth. The film composition depends on sticking and sorption processes of the photo-products on the substrate and growing film. This process is mainly used as a low temperature growth technique for dielectric films over large areas and it offers no spatial selectivity.

2.4.2: PERPENDICULAR ILLUMINATION

The laser beam is incident on the sample surface, usually in a perpendicular configuration. This process geometry favors both gas and surface decomposition of the reactant gases depending on the laser wavelength and power. Catalytic effects due to the laser beam have also been observed in addition to changes in nucleation kinetics and diffusion. Also the process offers a very high degree of selectivity.

2.5: PHOTO-EPITAXY

Photoepitaxy encompasses all photolytic and photo-thermal processes that can be used to modify the VPE reactions, either by means of decomposition of the precursors or in interaction with the surface to provide sufficient atom mobility necessary for epitaxial growth. This, of course, covers a wide range of processes using photon sources in the infrared, visible, or UV. These sources can be either lasers or incoherent lamps.

2.5.1 CLASSIFICATION FOR PHOTOEPITAXIAL GROWTH

1. Photomodified epitaxy: This includes laser-enhanced doping and laser-induced change in composition. No change in growth rate of epitaxial material occurs in the illuminated region but this can be used as way of achieving selective area control for semiconductor device processing.
2. Photoenhanced epitaxy: This process brings about an enhancement of the growth rate that is attributed to photolytic or photothermal processes.
3. Photoinduced epitaxy: This can simply defined as epitaxial growth only in

the illuminated region with no deposition outside this region. As with photoenhanced epitaxy, this can be a result of photolytic or photothermal reactions.

A list of reported epitaxial growth is shown in Table I, indicating the semiconductor material, radiation used, and classification. A large number of the epitaxial processes shown in Table I involve both photothermal and photolytic processes. The relevance of various processes to epitaxy can be seen in the schematic representation of the epitaxial growth shown in Fig.5. Laser interaction can be used to modify any part of this chain of processes by either enhancing the substrate or vapor temperature or by inducing photolytic reactions at any one or more of these stages. Examples of both processes are tabulated in Table I.

In the laser-induced epitaxial growth process, the enhanced deposition is usually confined to the area of illumination and would therefore be suitable for patterning. To provide sufficient energy for surface mobility and at the same time avoiding thermal decomposition and subsequent depositions in the unilluminated areas, the growth temperature is generally maintained at or below 400°C for most of the metallorganic precursor gases used in III-V and II-VI epitaxy.

2.5.2: PULSED LASER EPITAXY

2.5.2.1: EXCIMER LASER EPITAXY

Excimer laser-induced epitaxy can be viewed as a two-stage process where the first pulse decomposes the precursors and the second pulse heats up the substrate and provides the energy for surface diffusion of the adatoms that had

TABLE I : Semiconductor Materials Grown By Photoepitaxy

Reference [#]	Semi-conductor	Radiation	Photo-modified	Photo-enhanced	Photo-induced	Photo-thermal	Photo-lytic
Eden (6)	Ge	KrF			X		X
Ishitani (7)	Si	ArF, KrF, Hg-Xe		X		X	X
Karam (8)	Ga(As,P)	Ar ⁺			X	X	
Balk (9)	GaAs	Lp Hg arc, ArF, KrF			X		X
Doi (10)	GaAs	Ar ⁺		X			X
Kukimoto (11)	GaAs	ArF	X				X
Kisker (12)	CdTe	Lp Hg arc		X			X
Donnelly (13)	GaAs, InP	ArF			X	X	X
Irvine (14)	HgTe, CMT	Hg Hg arc			X		X
Morris (15)	CMT	ArF			X		X
Bicknell (16)	CdTe	Ar ⁺	X				X
Roth (17)	GaAs	Nd-YAG		X		X	

SCHEMATICS OF PROCESS STEPS FOR EPITAXIAL GROWTH FROM VAPOR PRECURSORS

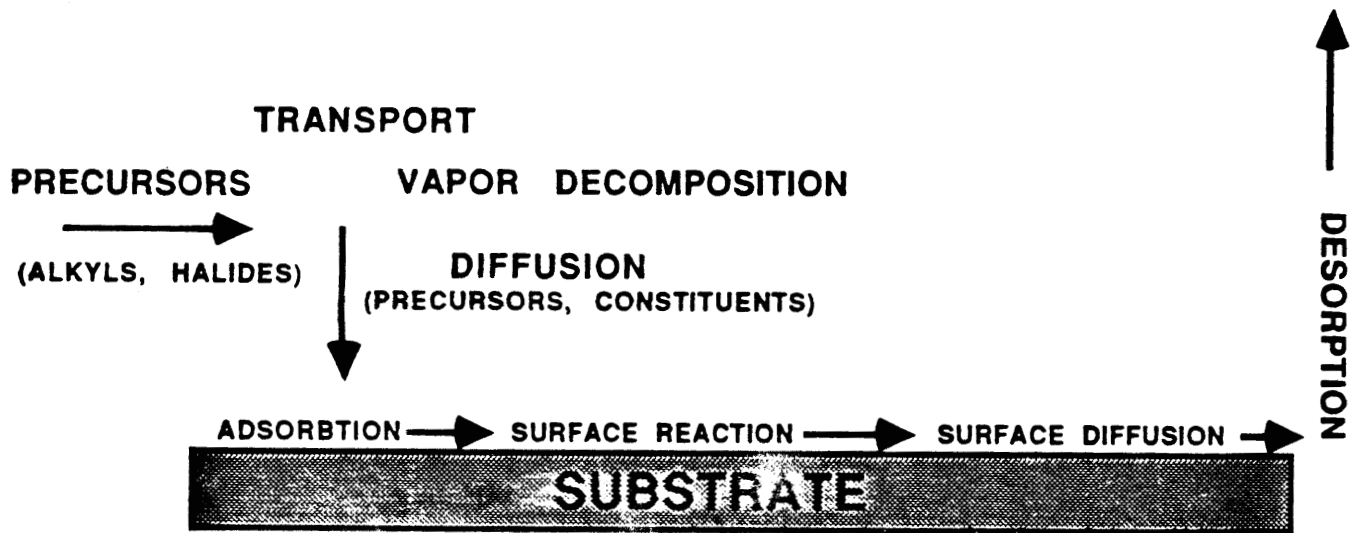


Figure 5. Schematics of the process steps for epitaxial growth from vapor precursors

impinged on the substrate. Some of the relevant literature in the excimer laser epitaxial process is reviewed and discussed in this section.

Excimer laser-assisted epitaxial growth of InP was reported by Donnelly et al. (13,18). An excimer laser (193nm), illuminating the substrate, decomposed the precursor molecules in the volume of the beam for the duration of the laser pulse. The substrate temperature was below the pyrolysis temperature of the precursors and the film was grown in only the illuminated regions. The precursors used were the adducts $(\text{CH}_3)_3\text{InP}(\text{CH}_3)_3$ with additional $\text{P}(\text{CH}_3)_3$, diluted with H_2 . At low laser fluences ($<0.03\text{J}/\text{cm}^2$) the deposited layer was not epitaxial and the estimated substrate temperature rise was below 300°C . Good-quality epitaxy was observed for fluences around $0.1\text{J}/\text{cm}^2$, where the transient heating was calculated to be around the melting point for InP of 1070°C . The high transient temperature reordered atoms on the surface and overcame poor nucleation that would otherwise have arisen from vapor-nucleated InP.

Laser-modified epitaxy has been reported by Kukimoto et al. (11). Selective area controls of carrier concentrations in GaAs and alloy compositions in AlGaAs have been studied by irradiating a specific area of the substrate with an ArF excimer laser during MOVPE growth. At substrate temperatures ranging from 600°C to 800°C , the growth rate was not influenced by the laser excitation, although surface morphology was remarkably improved at lower temperatures. An increase or decrease of carrier concentration in the selectively irradiated area of GaAs epitaxial layer was achieved. It was also demonstrated that the Al content of AlGaAs layers was higher in the irradiated area than in the unirradiated area.

2.5.2.2: Nd:YAG LASER EPITAXY

In the absence of photochemical dissociation of the precursors, pulsed laser irradiation of the surface at low temperatures will enhance both decomposition rate and surface mobility. Roth et al. (17) used a Nd:YAG laser (530nm) to irradiate the surface of GaAs for low temperature MOCVD using TMG and AsH₃ precursors. Laser light did not effect any photochemical dissociation in the gas phase, since neither of the precursors absorb strongly at 530nm. The growth rate enhancement observed was ascribed to an increased pyrolysis of the precursors due to laser heating. However, the laser pulses were of sufficiently short duration that enough precursor molecules did not arrive at the substrate while it was illuminated to cause a significant enhancement of growth rate. The explanation given for the enhancement lies in the adsorption of precursor molecules during the "off" periods, which are then pyrolyzed in the "on" periods. The implication of this argument is that the adsorption is much higher than would be expected for a physisorbed Langmuir film of the precursors at these temperatures.

2.5.3 CW LASER EPITAXY

Instead of a pulsed laser, a cw argon ion laser could be used to locally heat the substrate to enhance photothermal growth. This was the technique adopted by Karam et al.(8) to "direct-write" epitaxial GaAs structures by scanning the laser beam on a substrate. Thick films were grown by multiple scanning of the beam. The disadvantage of such a process was the large processing times and hence a poor throughput.

Laser-enhanced MOVPE can be taken a step further to chop a laser beam so that a surface-adsorbed layer can be exposed to radiation resulting in

decomposition. Doi et al. (10) used this modulation technique to induce atomic layer epitaxy (ALE) of GaAs. The concept of ALE is to grow alternate layers of Ga and As resulting in a very high quality crystal. In the laser-ALE technique the precursors of TMG and AsH_3 were introduced alternatively into the growth chamber. Significant growth enhancement from $0.33\mu\text{m}$ to $1.07\mu\text{m}$ at 500°C when the laser was on during the TMG cycle while it was absent with the laser on during the AsH_3 cycle. Also, growth enhancement was greater when n-GaAs was used instead of p-GaAs or semi-insulating GaAs. The mechanism for enhancement was described as a photo-assisted catalytic effect, where TMG pyrolysis was enhanced on an arsenic surface under 514-nm argon ion laser radiation. compositions in AlGaAs

2.6 LASER-SOLID INTERACTION

2.6.1 ELECTRONIC PHENOMENA

Absorption mechanisms:

Five distinct mechanisms or processes for the absorption of light by semiconductors can be identified (19):

1. Photons with energy ($h\nu$) much less than the band-gap energy (E_g) can excite lattice vibrations directly.
2. Free or nearly-free carriers can be excited by absorption of light with $h\nu > E_g$; such carriers will always be present as a result of finite temperatures and/or doping.
3. An induced metallic-like absorption due to free carriers generated by the laser irradiation itself can occur.

4. For photon energies $> E_g$, absorption will take place by direct and/or indirect (phonon-assisted) excitation of electron-hole pairs.
5. Absorption induced by broken symmetry of the crystalline lattice is possible.

Mechanism [1] will play a significant role for laser radiation in the wavelength range corresponding to lattice vibrations; for example, CO₂ laser radiation at $\lambda = 10.6\mu\text{m}$ couples very efficiently to lattice vibrations of many materials. However, this mechanism has not proved particularly useful for laser processing of semiconductors and will not be considered further here.

Mechanism [2] is involved in the absorption of laser radiation of all wavelengths but is particularly crucial for laser photon energies less than E_g in heavily doped indirect band gap semiconductors like silicon and gallium phosphide.

Mechanism [3] which will produce an intensity-dependent α , where α is the absorption coefficient, may be of considerable potential importance at the photon densities used in pulsed laser processing, especially for wavelengths near the indirect band gap and/or for very short duration pulses. The equilibrium density of free carriers generated by the laser irradiation and hence the importance of mechanism [3], depends on the carrier recombination rate and it appears that this rate is so rapid that in the nanosecond regime of pulse durations, mechanism [3] is relatively unimportant compared to [4] in determining α for laser radiation well above the indirect band gap in GaP.

The largest contribution to α (for nanosecond pulses) for radiation with $h\nu > E_g$ in indirect band gap semiconductors which have not been heavily damaged arises from mechanism [4]. Mechanism [5] is quite important in laser annealing

of ion-damaged semiconductor surfaces in which α may easily be increased by an order of magnitude or more over the crystalline value.

For photon energies much greater than the band gap of the semiconductor, α is virtually independent of both the temperature and the state of the material, since the contributions to α of nonlinear free-carrier absorption is almost certainly insignificant for these short wavelengths. More precisely, α is already so large that further increases are unimportant.

After the laser energy has been absorbed by the electronic system, the following processes may redistribute the energy:

1. carrier collisions
2. plasmon production
3. electron-hole recombination by an Auger process
4. electron-hole creation by impact ionization (the inverse of 3) and
5. phonon emission.

The first four processes result in the redistribution of the energy among the carriers, while the last process results in transfer of energy to the lattice, thus raising its temperature.

Although there are still some minor discrepancies between the work of various groups, it would appear that the sequence of events, on a subnanosecond time scale, initiated by an intense laser pulse of energetic photons is reasonably clear. These events are illustrated schematically in Fig.6, which is adapted from von Allmen (20). The initial events in the absorption process are band-to-band electronic transitions indicated by event 'a' on the Fig.6. A small fraction of the

absorbed energy may be transferred to the lattice by phonon emission but the more likely events are free carrier absorption by the excited electrons (b and c) followed by electron-electron collisions. These collisions produce a thermal equilibrium distribution about energy kT_e , where T_e is the electron temperature, (cross-hatched area on diagram), with T_e much greater than the lattice temperature, in times of the order of 10^{-14} sec. The electron and hole populations are brought into thermal equilibrium with one another at about the same time through impact ionization and Auger recombination. The schematic illustration of these events in Fig. 6 indicates that there is transfer of energy between the electrons and holes without any dissipation of the energy of the carrier system. Phonon emission on the time scale of 10^{-12} sec transfers energy to the lattice and heats it to the melting point in a few picoseconds. Simultaneously, the density of carriers decays (and therefore the plasmon frequency decreases) by way of Auger recombination. On a much longer time scale, a very low density of electrons at the bottom of the conduction band can radiatively recombine with the remaining holes in the valence band, producing a weak, long-lived emission. This picture clearly implies that heating model calculations in which it is assumed that transfer of the laser energy from the electronic system to the lattice occurs in times comparable to, or less than, the pulse duration should remain valid even in the picosecond regime.

2.6.2: LASER-SOLID INTERACTION: HEATING THEORY

In the previous section the photon-electron interactions were described and it is clear that the creation of phonons occur in very short time. A natural consequence of this process is heating of the solid and the theory of heat conduction is

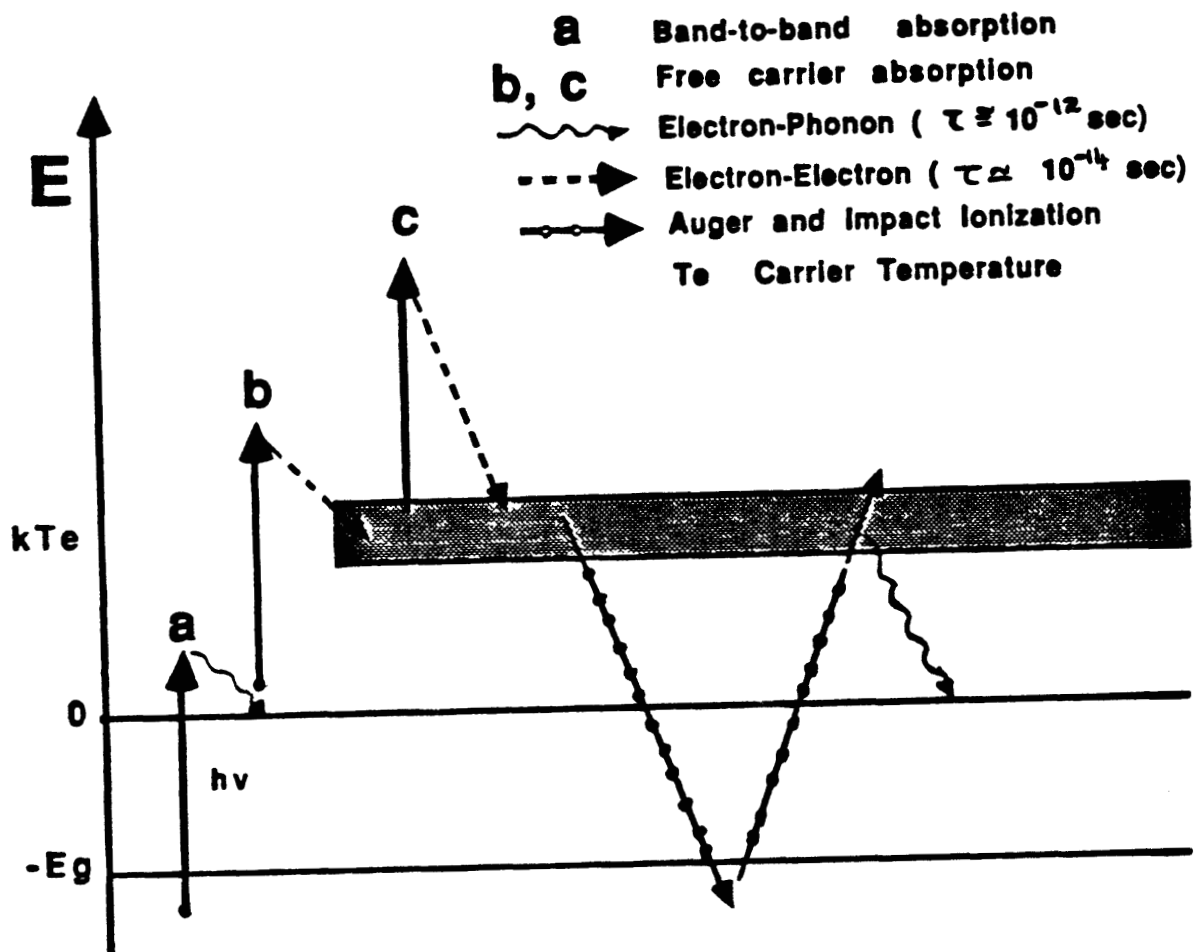


Figure 6. Schematic illustration of the elementary photoexcitation processes, carrier equilibration mechanisms, and electron-phonon interactions in a semiconductor exposed to laser radiation with $h\nu > E_g$. Adopted from von Allmen (1980).

described in the following sections for both pulsed and cw laser interactions.

2.6.2.1: PULSED LASER HEATING

In this case, the feature size is large compared to the thermal diffusion length; alternatively, the time scale of interest is short compared to the time for lateral diffusion across the feature size of interest. Under these conditions heat, first deposited in the near surface, is transported in to the bulk largely by one-dimensional heat conduction according to

$$J(z,t) = -k_T \Delta T(z,t) \quad (2.1)$$

$$\rho C_P dT/dt = -dJ/dz \quad (2.2)$$

where the z axis points perpendicular into the substrate. Here, J is the heat flux, T is the temperature, and k_T and C_P are the thermal conductivity and heat capacity, respectively (21).

The thickness l_o of the near-surface region that is initially heated up by a short laser pulse (typically 5-100 nsec) is equal to the optical absorption length l_{opt} , or the thermal diffusion length $l_T = \sqrt{D_T \tau_{pulse}}$ during the pulse width τ_{pulse} , whichever is greater: $l_o = \text{Max}(l_{opt}, l_T)$. For the case of metals (strong absorbers), the optical absorption depth is much shorter than the thermal diffusion length during the pulse, so that $l_o \rightarrow l_T$ except for very short (sub-picosec) laser pulses. For semiconductors and insulators in the infrared (weak absorbers), however, the optical absorption depth can be greater, so that $l_o \rightarrow l_{opt}$. For semiconductors above their band gaps (intermediate absorbers), the two thicknesses may be comparable. Unless melting occurs, the maximum tem-

perature rise ΔT_{\max} in this layer is determined approximately by

$$\rho C_p l_o \Delta T_{\max} = I(1-R) \quad (2.3)$$

where I is the incident laser fluence (in J/cm^2), $I(1-R)$ is the absorbed laser fluence and R is the optical reflectance of the solid.

Thermally enhanced chemistry will, of course, only occur while the surface is hot. Except for the shortest laser pulses and the highest thermal conductivity materials, the surface is hot for a duration determined not by the temperature rise time (approximately the laser pulse width itself), but rather by the temperature fall time. This fall time is in turn determined by heat diffusion into the bulk after the pulse. The dependence of the temperature distribution on depth z , and time t , assuming the pulse to be centered at $t=0$, is characterized approximately by the (half) Gaussian (21)

$$T(t) = T_{\text{Sub.}} + \Delta T(z=0,t) \exp \left[- \left(\frac{z}{l_o + \sqrt{4D_T t}} \right)^2 \right] \quad (2.4)$$

with the time-dependent skin temperature change

$$\Delta T(z=0,t) = l_o / (l_o + \sqrt{4D_T t}) \Delta T_{\max} \quad (2.5)$$

The temperature fall time is seen to be approximately

$$\tau_{\text{fall}} = l_o^2 / 4D_T \quad (2.6)$$

typically much longer than the temperature rise time. This fall time, rather than the pulse width itself, is the main determinant of the duration of the reaction enhancement due to laser irradiation.

Often, in the event of a phase change (solid to liquid transformation) that may occur at high fluences, surface chemistry is enhanced considerably. In this event, the important quantities are fluence threshold for melting the maximum molten layer thickness, and the duration of the surface melt. All these quantities have been modelled and reported in literature for pulsed laser melting of silicon; the simple estimates derived in that work should be applicable to other materials, however.

2.6.2.2: CW LASER HEATING

Direct Writing: Heat Diffusion in Three Dimensions

For focussed radiation from a cw laser beam, the thermal diffusion problem is three-, rather than one-dimensional. In that case, it has been shown by Lax (22) that for cw irradiation by a Gaussian beam of waist-size ω_0 (radial intensity distribution $I_0 \exp(-(r/\omega)^2)$), the steady-state increase in the surface temperature distribution is

$$\Delta T(r, t=\infty) = \frac{1}{\sqrt{\pi}} \int_0^{\pi} \frac{1}{2} J_0(\lambda r / \omega_0) \exp(-\lambda^2 / 4) d\lambda \quad (2.7)$$

Where J_0 is the Bessel function of order 0. For most of practical purposes, this may be approximated by a Gaussian with a lateral spatial extent larger by $\sqrt{\pi}$ than the original intensity distribution, or

$$\Delta T(r, t=\infty) = \Delta T_0 \exp(-r^2 / \pi \omega^2) \quad (2.8)$$

Here, ΔT_0 , is the peak temperature increase at spot center, is given by

$$\Delta T_o = \Delta T(r=0, t=\infty) = P(1-R)/(2\sqrt{\pi}K_T\omega_o) \quad (2.9)$$

where P is the incident power and R is the optical reflectance. These equations are valid in the steady state, which is reached on a time scale approximately equal to the diffusion time over one spot size, $\tau_o = \omega_o/4D_T$

2.6.3: LASER MATERIAL INTERACTION: MEASUREMENT TECHNIQUES

Effect of pulsed laser irradiation on a substrate can be studied using in-situ and post-irradiation techniques. These techniques are discussed below.

1. Conventional post-irradiation measurements such as Scanning and transmission electron microscopy (SEM and TEM), scanning auger electron spectroscopy, Rutherford backscattering (RBS) and sheet electrical properties measurements; and
2. Time-resolved measurements during and immediately after pulsed laser irradiation, including measurements of optical reflectivity and transmission, electrical conductivity, as well as structure and/or temperature sensitive measurements such as pulsed Raman scattering, X-ray diffraction measurements of lattice strain, optical second harmonic generation, and electron diffraction.

During the investigation of laser-assisted film growth, SEM and TEM have been extensively used for film characterization. The only in-situ measurements carried out were the electrical conductivity measurements of the semiconductor during pulsed laser irradiation to determine the effect of the laser pulsing at high rates on the temperature rise.

Results and discussion are compiled in chapter 4 which is followed by a summary, conclusion, and future work.

3. EXPERIMENT

3.1 DIRECT-WRITE OF GaP USING ARGON ION

3.1.1 EXPERIMENTAL SET-UP

The experimental configuration used for direct deposition of GaP structures is sketched in Fig.7. The 514.5 nm output from an Argon ion laser first passes through a beam expander and then is steered into a multi-element f/5.6 focusing lens. The lens was mounted on a precision X-Y stage, which can be translated a maximum of 2 inches along each axis by stepper motors in increments of 0.1 μm . By programming the motions of the stepping motors it was possible to 'write' various geometric patterns. Typically 3 mm long lines and 500X500 μm pads were grown. An IR sensitive vidicon camera allowed us to visually monitor the location of the deposition and in-process growth. An AlGaAs IR diode was used for illumination of the sample for video observation. The substrates were placed in a stainless steel reaction cell which had a quartz window. The cell was designed to accommodate 2-inch diameter substrates. The gas manifold and the deposition cell were heated to about 120°C to avoid any condensation of the precursor gases, especially on the window. A Baratron pressure measuring gauge was attached to the manifold. All the depositions reported below were obtained under static gas conditions.

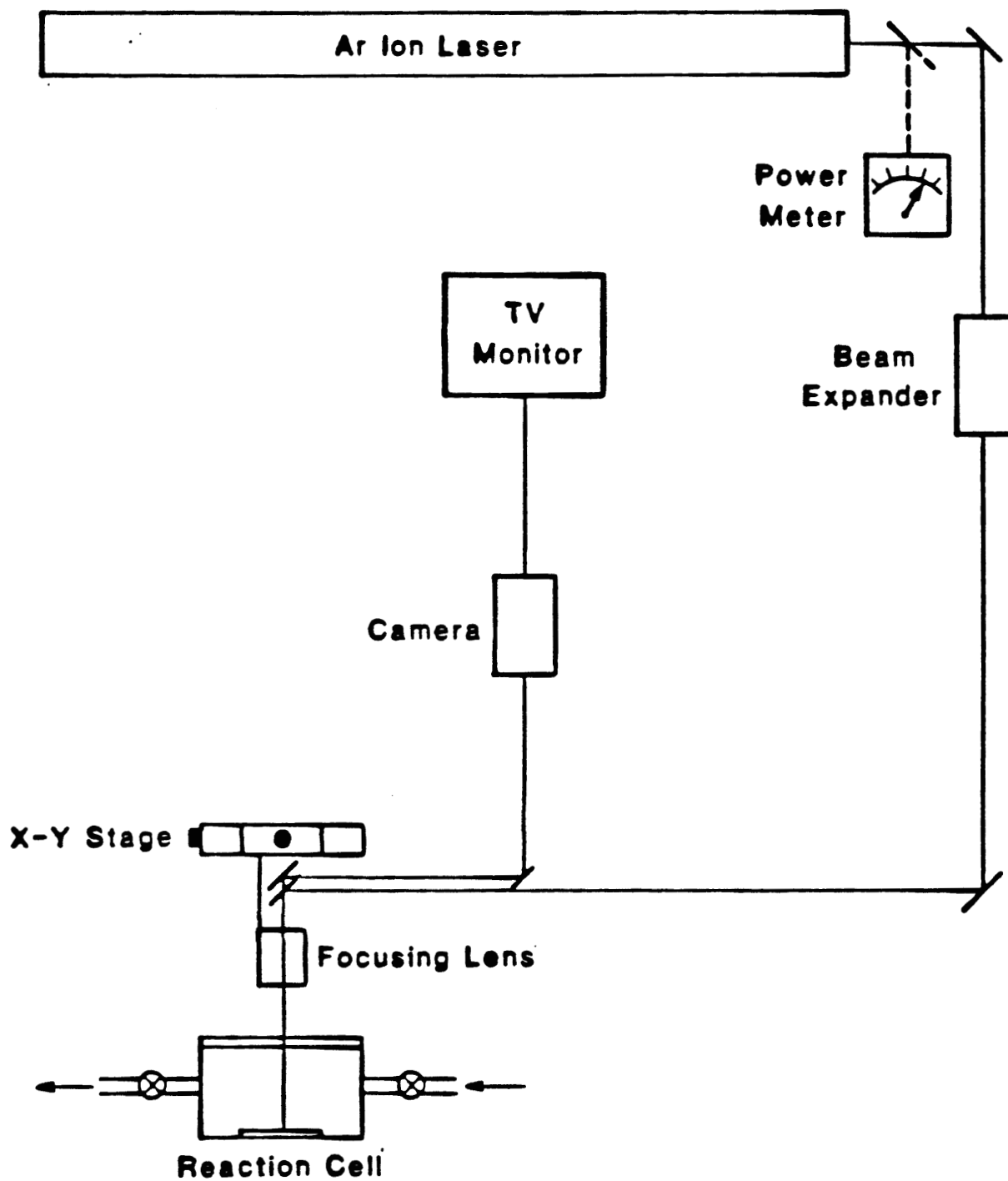


Figure 7. Schematics of the 'direct-write' experimental arrangement.

3.1.2 GROWTH PROCEDURE

The precursor gases for deposition of GaP were electronic grade trimethyl gallium (TMG) and tertiarybutyl phosphine (TBP), which is a relatively new phosphorous source. TBP was selected over phosphine due to lower safety risks (23). Once the cell was filled with appropriate partial pressures of the precursors, its pressure was brought up to one atmosphere with hydrogen. Several different substrates have been examined.

Liquid encapsulated Czochralski (LEC) GaP substrates were used, which were first degreased in organic solvents, followed by a one minute etch in a 10:1:1 mixture of $\text{H}_2\text{SO}_4:\text{H}_2\text{O}_2:\text{H}_2\text{O}$. This was followed by a DI water rinse and dry blowing with nitrogen before they were loaded into the deposition cell.

Selective area deposition of GaP on Si was also investigated. The (100) oriented silicon substrates were first etched in 10% HF, followed by deionized water rinse and dried by blowing nitrogen before they were loaded into the deposition cell.

The removal of native oxide on silicon was investigated using three approaches. The first method involved a photochemical approach where after pumpdown, the cell was first backfilled with 4 Torr Cl_2 . The substrates were then irradiated with a medium pressure, microwave excited mercury lamp. At a substrate temperature of about 150°C , the etch rate was about 500 Å/min. After etching, the cell was purged with hydrogen before the precursor gases were introduced. The second technique involved prescanning the area on which epigrowth was desired with the laser at high power (1W) in order to thermally desorb the native oxide. The third approach also involved thermal desorption (in presence of hydrogen) and proved to be the simplest. The substrates were irradiated by high

intensity tungsten-halogen lamps and the thermal cycle consisted of raising the temperature to 850°C for half an hour and then cool down to 200°C. Following the oxide removal, the reactant gases were introduced into the reactor.

3.2 EXCIMER LASER-ASSISTED EPITAXY

3.2.1 EXPERIMENTAL SET-UP

The laser deposition system used for this investigation consisted of an excimer laser and a stainless steel deposition chamber. A detailed schematic of the experimental set-up is shown in Fig.8. High purity hydrogen is first passed through a back pressure valve to reduce the pressure to 2 psi. This hydrogen was bubbled through the metallorganic sources which were kept in a constant temperature bath. Hydrogen from the output port of the metallorganic bottles was passed through mass flow controllers (MKS system) at set values. The outputs from the mass flow controllers were mixed in a manifold before being fed into the reactor. Dilution hydrogen was flowed through another mass flow controller before mixing with the precursor gases in the manifold.

The 193nm output from an ArF laser (Questek 2000) was focused to a 2 x 7 mm² spot size onto a substrate which was placed in the reactor. The laser was operated at a pulse rate of 50 Hz with a power lock which maintained a constant output power. The substrate was placed on a stage whose temperature could be varied from ambient to 600°C. The UV radiation entered the reactor through a sapphire window, which was kept clear of deposits with a hydrogen purge system. The gases were passed through a thermal cracker which was maintained at 700°C, in order to dissociate any unreacted precursors.

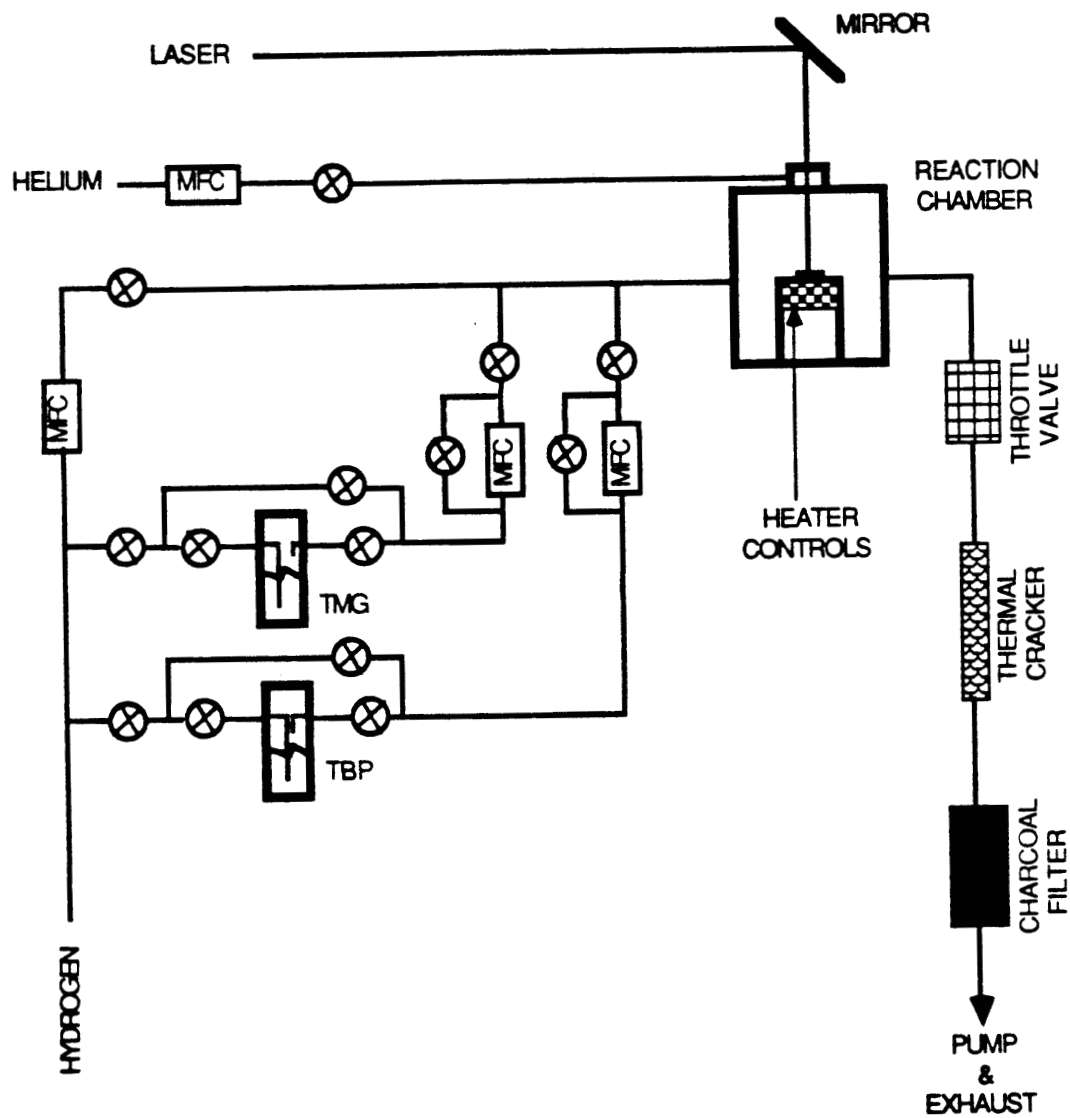


Figure 8. Schematics of the excimer-laser assisted deposition set-up.

3.2.2 GROWTH PROCEDURE

The (100) oriented sulphur doped ($N_D = 10^{16} \text{cm}^{-3}$) GaP substrates were first degreased in organic solvents and then etched in a 5:1:1 solution of $\text{H}_2\text{SO}_4:\text{H}_2\text{O}:\text{H}_2\text{O}_2$. This was followed by rinsing in deionized water and blowing dry with nitrogen before they were loaded into the deposition cell. The cell was evacuated to 10^{-4} Torr before the flow of precursor gases was started.

The precursor gases were electronic grade trimethylgallium (TMG) and tertiarybutylphosphine (TBP), which is a new phosphorous source. TBP was selected due to its significantly lower toxicity compared to phosphine [9]. Hydrogen was flowed through TMG(-15°C) and TBP(5°C) bubblers and the flow rates of the carrier gas (H_2) plus the organometallics were 3 sccm and 24 sccm, respectively. The P/Ga ratio was 3.2. Zinc doping was achieved by flowing dimethyl zinc (50 ppm in He) during the epigrowth. The reactor pressure was typically 30 torr, unless stated otherwise.

3.2.4 TRANSMISSION ELECTRON MICROSCOPY

A Hitachi H-800 analytical electron microscope equipped with LaB_6 filament was used to observe the crystal defect structures in the thin film semiconductor samples and their chemical composition was analyzed using a scanning transmission electron microscope (STEM) together with a Tracor/Northern TN 5500 EDS system. The acceleration voltage of 200 KeV and filament current of 20 μA were the observation conditions.

The wafers were cut into 2.5 mm squares and bonded on a Gatan grinder using crystalbond supplied by Aremco Product and ground to about 30 μm thickness with 600 mesh Buehler grinding paper. Crystalbond was dissolved using

acetone. At this stage, since the samples were fragile that it was almost impossible to pick them up using tweezers. Therefore filter paper was inserted below the Gatan grinder before dissolving the Crystalbond in acetone. The samples, then dropped slowly on the paper when the Crystalbond dissolved. The paper was then removed from the acetone and dried in air. A tiny amount of epoxy was smeared on a 3mm Cu grid which had a 1mm hole at the center. The Cu grid was picked up using tweezers and laid softly on the sample. The sample with grid was dried for 3 hours and ion milled using a Ion Tech ion milling unit.

The basic technique of cross-sectional sample preparation is well established in the literature (24). Two wafers were stacked face to face using the commercially available epoxy mixture supplied by Hardman Inc. and cured for 3 hours at 200°F (Fig. 9). Stacks were cut cross-sectionally into 0.5 mm thick square pieces using a Isomet low speed diamond saw manufactured by Buehler. Further steps were same as for the plan-view sample preparation, however, ion-milling was carried out from both sides of the sample.

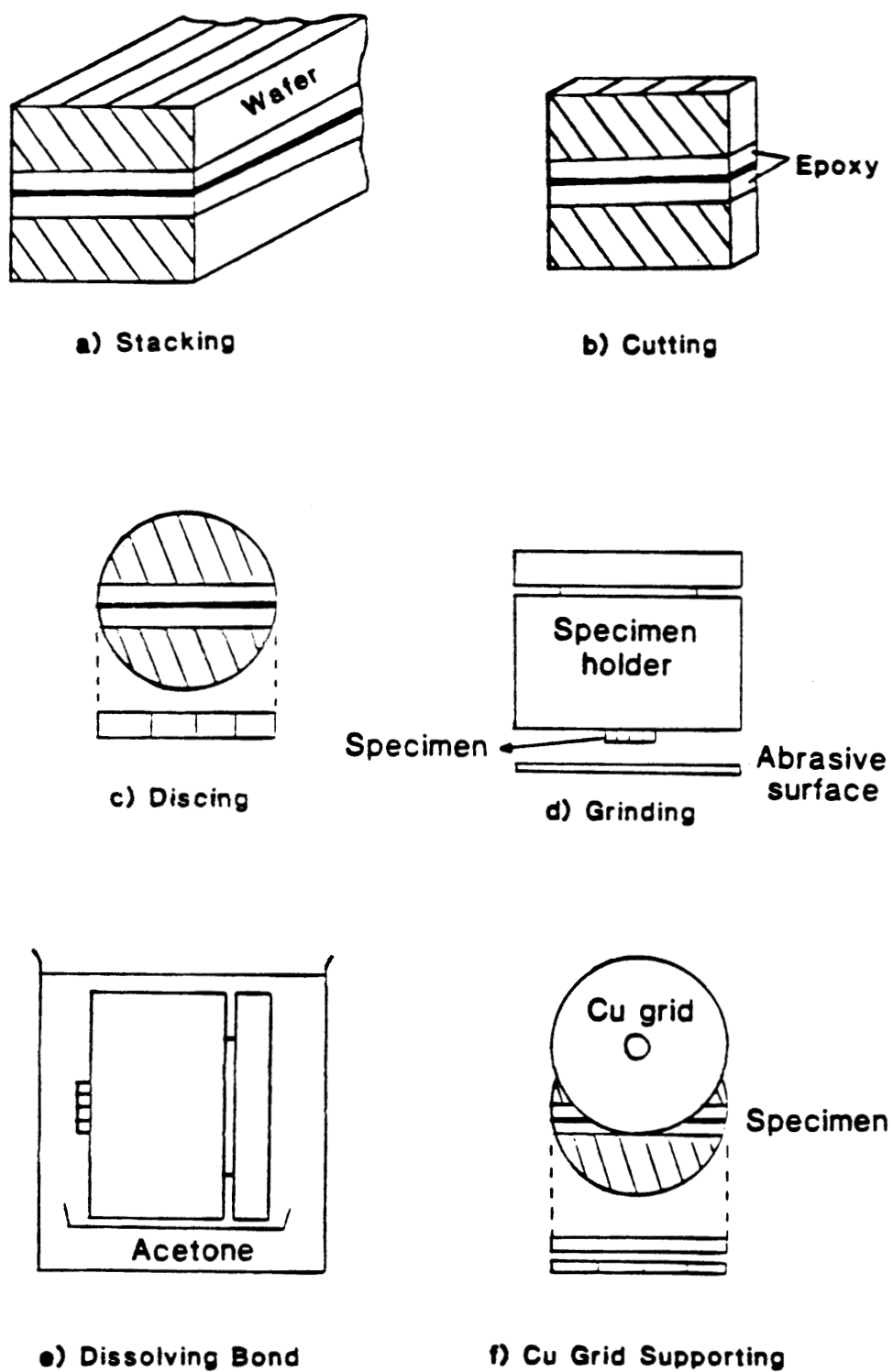


Figure 9. Schematics of TEM cross-section sample preparation procedure.

4. RESULTS AND DISCUSSION

4.1 ARGON ION LASER-INDUCED SELECTIVE AREA GROWTH OF GaP

4.1.1 INTRODUCTION

Laser-induced reactions have been successfully used for deposition of a wide range of materials. An important attribute of this process is the high spatial resolution deposition that can be achieved without the use of photolithography. An application of this technique for epitaxial growth of GaP microstructures for potential optoelectronic applications is described below.

'Direct-writing' of metals and elemental semiconductors have been reported extensively in literature (25-35). The deposition process usually involves the use of a scanning argon ion laser on a substrate that is kept in the ambient of reactant gases. The laser either locally heats the substrate and the thermal energy is transferred to the surrounding gases which dissociate to initiate nucleation and growth process (pyrolysis) or photolytically dissociates the adsorbed layer leading to selective area growth (photolysis). Here, we have adopted the former approach to obtain selective area epitaxial growth of GaP.

4.2 HOMOEPITAXIAL GROWTH

The precursor gases for deposition of GaP were electronic grade trimethyl gallium (TMG) and tertiarybutyl phosphine (TBP). Several different substrates

have been examined. In the first part homoepitaxial growth of GaP is discussed and in the second results obtained on the heteroepitaxy on Si is presented. When the laser beam was held stationary on the substrate, pyrolytic decomposition of the precursor gases occurred leading to the deposition of stoichiometric, polycrystalline GaP as shown in Fig.10. This was our first laser-assisted deposit of the semiconductor.

One of the first series of experiments involved examination of the partial pressures of the precursor gases. As expected, the growth rates increased with partial pressures at constant laser conditions. For example, at TMG partial pressure of 12 torr, V/III ratio of 15 and laser power of 2W, GaP depositions over 2 microns thick were obtained with a single scan. These depositions were obtained on several different substrates, including Si and GaAs. However, these deposits proved to be polycrystalline. Obviously the growth rates had to be reduced in order to obtain epitaxial films. This was achieved by reducing the concentrations of the precursors and using low power, multiple laser scans.

Smooth and continuous epitaxial lines and pads (by raster scanning) were deposited over a range of scan speeds (50 - 125 μm) and laser power (1 to 2 W) at TMG partial pressures of 2 to 4 torr and V/III ratio range of 10 to 20. The growths were stoichiometric over this V/III ratio range.

The thickness of the deposits were measured using a Dektak profilometer that made use of a 2 μm tip stylus. An example of a direct-write structure is shown in Fig.11, which is a scanning electron micrograph. An end view of this structure measured about 6.3 μm wide at the base and 2.5 μm high. Gaussian curve fit to profilometer data showed reasonable agreement, especially for the bottom half of the deposit. The top half of the deposit was slightly narrower



Figure 10. SEM micrograph of polycrystalline GaP grown using a stationary argon ion laser beam.

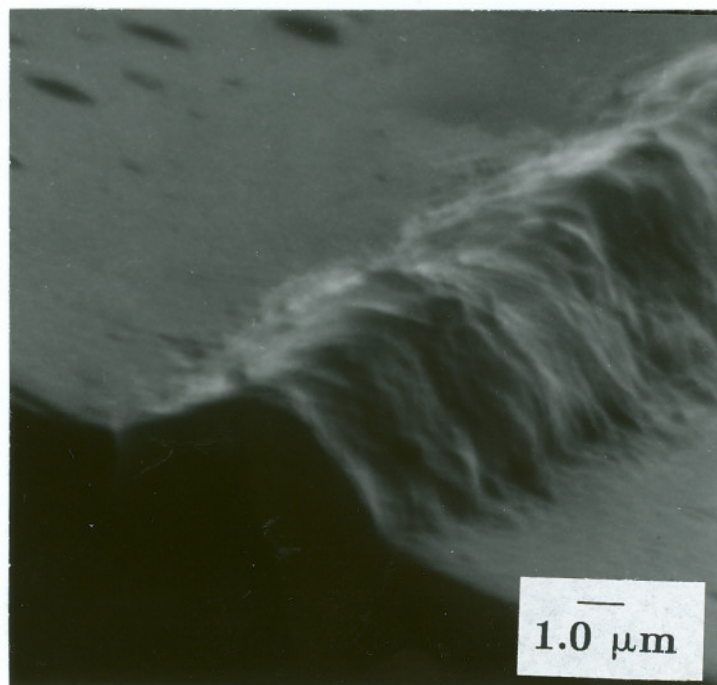


Figure 11. SEM micrograph of a laser deposited GaP line

than the gaussian profile. This was not surprising since TEM_{00} mode of the laser was providing the thermal energy. The areas under these profiles (calculated by the profilometer) were proportional to their heights (Fig.12). Therefore the amount of deposition is represented in terms of their heights. An exception to this was at high laser where double peaks were observed.

The thickness of the deposits as a function of the number of scans is shown in Fig.13, where the scan speed was $100 \mu\text{m}/\text{sec}$, V/III ratio of 10, and laser power of 0.4 W. It can be seen that initially the growth per scan was relatively high, however it gradually decreased. One possible reason for levelling off of the growth/scan is the depletion of reactants. For a typical deposit of height $2 \mu\text{m}$, the cross-sectional area calculated by the profilometer was about $15 \mu\text{m}^2$. For a typical scan length of 2000μ , the volume of the deposited material is $3 \times 10^{-4} \text{ cm}^3$. Usually ten such scans were taken for each filling of the gases. Therefore the total volume of GaP deposited was $3 \times 10^{-7} \text{ cm}^3$. Assuming the theoretical density of GaP ($4.13 \text{ gr}/\text{cm}^3$),

the total weight of the deposits was 1.3×10^{-6} gram. In this deposit, the weight of gallium was 9.1×10^{-7} grams which corresponds to 8×10^{16} gallium atoms. Now, considering 1 Torr of TMG at 360K, number density of the gas is given by

$$n = 9.65 \times 10^{18} P/TV \quad (4.1)$$

where P is the vapor pressure of the gas. T is the temperature in K and V is the volume of the cell. This correspond to $2.6 \times 10^{18} \text{ atoms}/\text{cm}^3$ which about 10^3 times the number of Ga atoms in the deposit. Hence the depletion of the precursor gases was not the reason for levelling off of the deposit with increasing number of scans. One of the reasons for the slowing of the growth was the decrease in laser

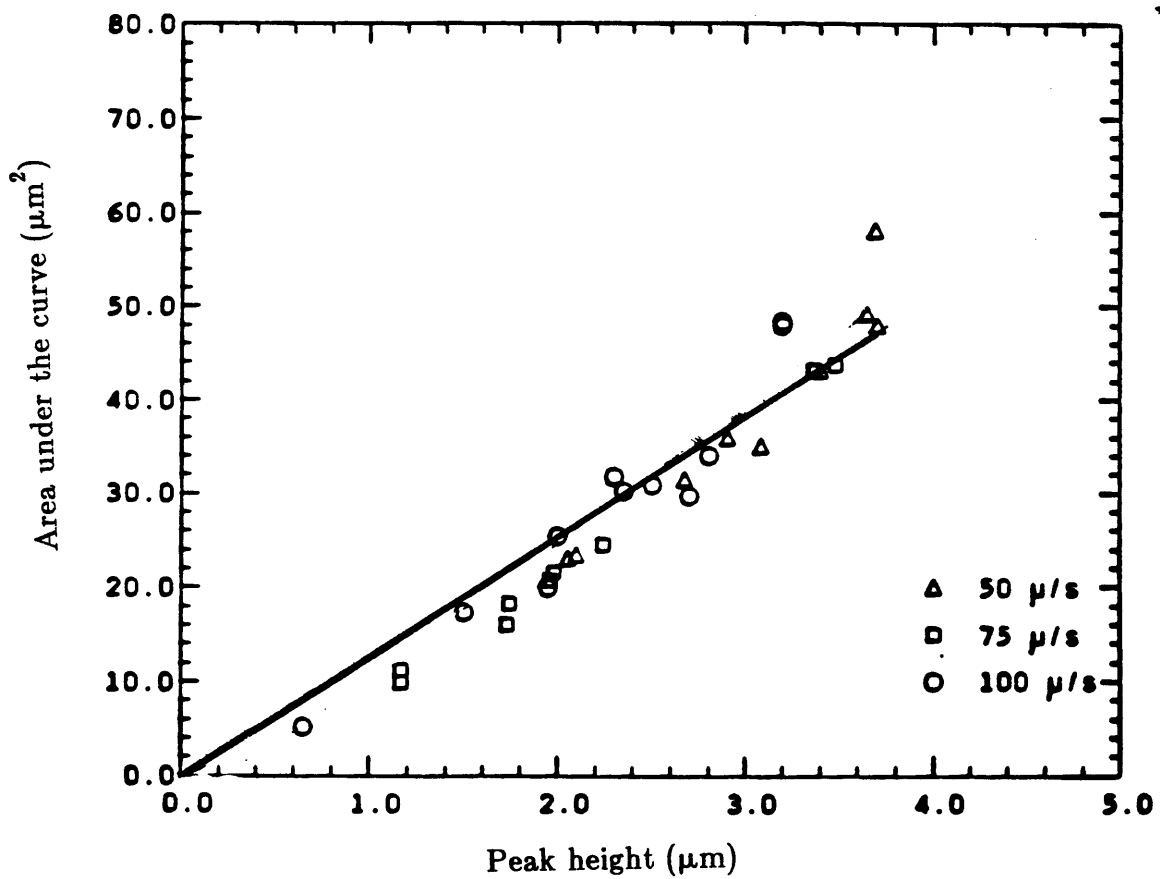


Figure 12. Plot of area under the curve (from profilometry) vs. peak height of the deposit.

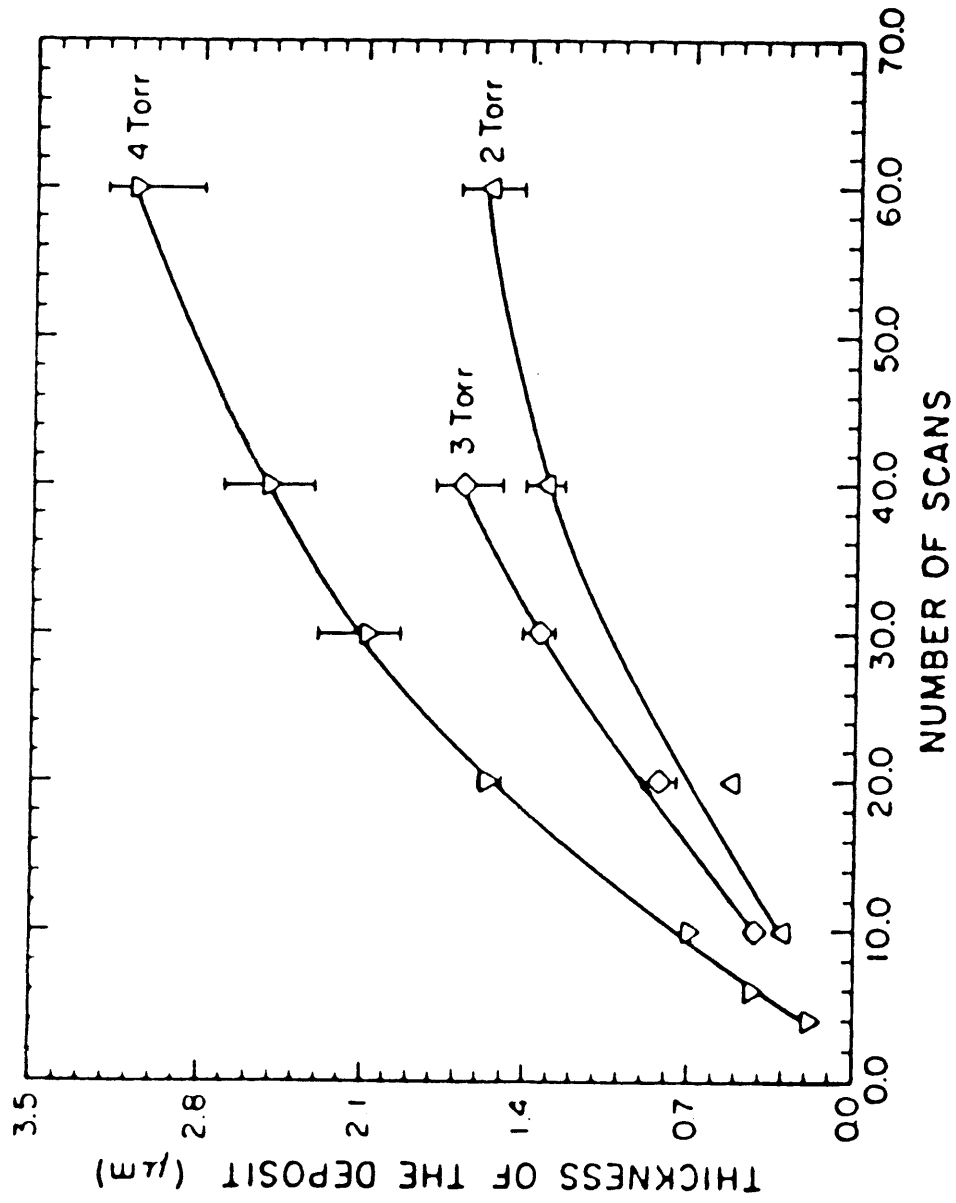


Figure 13. Plot of epitaxial growth vs the number of scans (multiple) at 2, 3, and 4 Torr TMG partial pressures.

intensity. This can be visualized by considering the projection of a circular area on the spine of a ridge structure (Fig.14). As the growth progresses, the height of the ridge increases which further increases the projected area on it. This has been modelled by assuming a perfectly gaussian shaped deposition profile as discussed below.

Consider an equation for a Gaussian curve with the variance σ

$$y = 1/(\sigma\sqrt{2\pi}) \exp(-x^2/(2\sigma^2)) \quad (4.2)$$

Since the deposit is fairly Gaussian shaped, peak height of the deposit, h is given by

$$h \Big|_{x=0} = 1/(\sqrt{2\pi}\sigma) \quad (4.3)$$

Rewriting eq. 4.2 in terms of h yields

$$y = h \exp(-\pi x^2 h^2) \quad (4.4)$$

Referring to Fig.14, the arc length (l) from $-r_y$ to r_y over the gaussian curve will give the major axis $(2r_y)$ of a 90° ellipse whose minor axis is the diameter of the laser beam $(2r_x)$. The arc length (l) $(2r_y)$ is given by

$$2r = \int_{-r_x}^{r_x} \sqrt{1+(dy/dx)^2} \quad (4.5)$$

or

$$r_y = \int_0^{r_x} \sqrt{1+4\pi^2 h^6 x^2 \exp(-\pi^2 h^4 x^4)} \quad dx \quad (4.6)$$

Equation 4.6 was numerically integrated using simpsons rule for different peak heights of the Gaussian profile. Referring to Fig.14, using the integrated arc length (r_y) , a normalized radius of the projected laser beam was calculated using

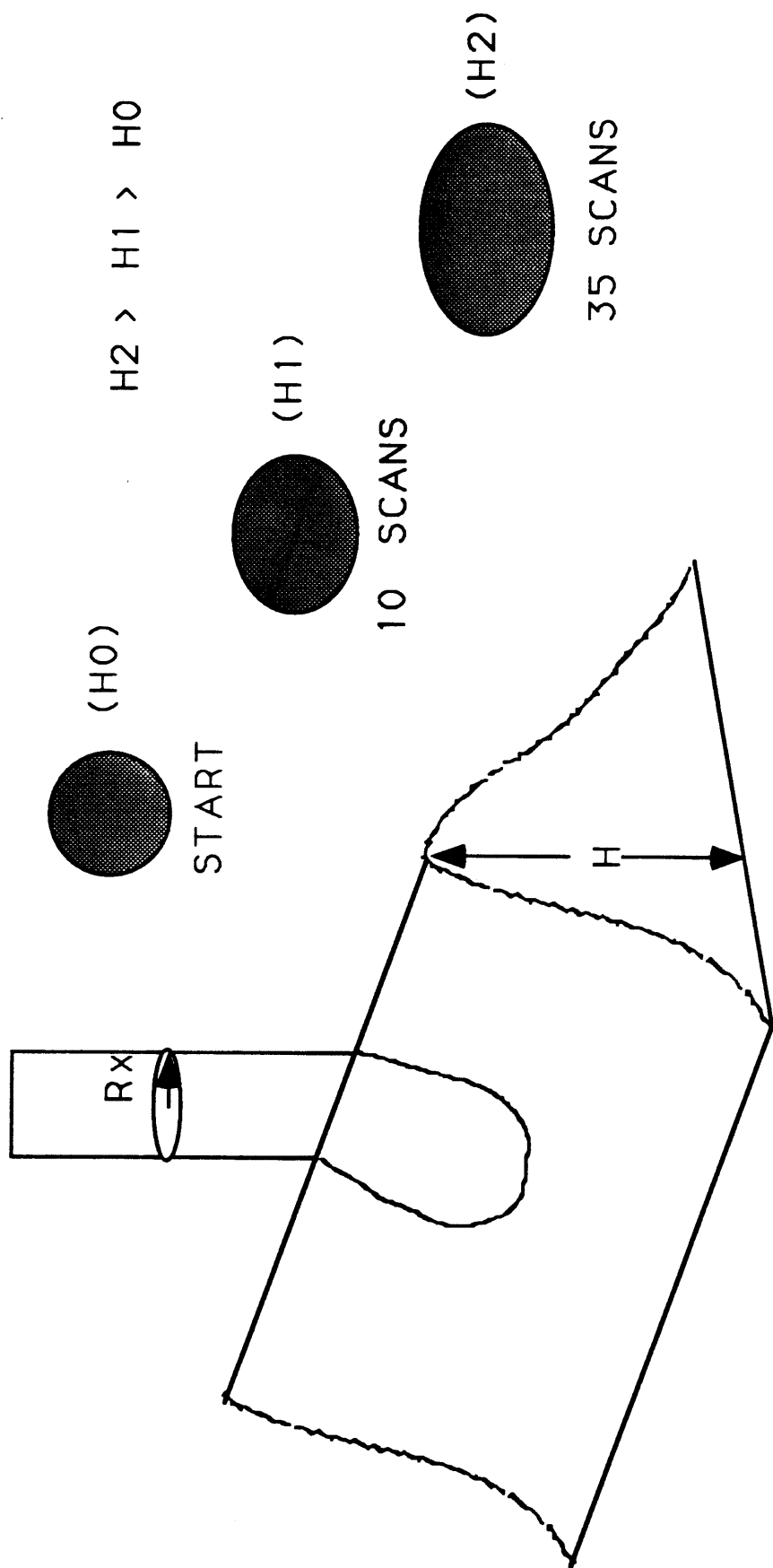


Figure 14. Schematic of the projected laser profile on the spine of ridge (deposit).

the expression

$$r = \sqrt{r_x r_y} \quad (4.7)$$

This normalized radius was used in the calculation of peak temperature and the temperature profiles as a function of laser power for different peak heights. The peak temperature is given by the expression

$$T_{\max} = P(1-R)/(2\pi^{1/2}K(T_o)) \quad (4.8)$$

where the term $P = p/r$ is the incident laser power per characteristic radius unit, R is the reflectivity, and $K(T_o)$ is the thermal conductivity at the starting substrate temperature. The peak temperature calculated for different deposit heights is shown in Fig.15. It is evident that the temperature dropped non-linearly for increasing deposit peak height. Assuming the growth rate is proportional to the temperature rise, a drop in growth rate is expected for increasing deposit height (In the laser microchemical processing, 3-D diffusion of molecules to and from the reaction zone becomes effective while in large area processing only the component normal to the substrate is relevant. Therefore transport limitations in the laser chemical processing will arise only at much higher temperature i.e., kinetically controlled regime is extended to higher temperatures. Hence the growth rate in the above discussion was assumed to follow an arrhenious relation). Thus the growth per scan slowed down for increasing number of scans. To illustrate the significance of the increasing projected area during growth, SEM micrographs of the deposits after 10 and 40 scans are shown in Fig.16a & 16b, which clearly show the evolution of the ridge structure. A plot of peak temperature as a function of deposit height for different beam radius is shown in Fig.17. In the above model, when the beam radius is varied for a particular laser power,

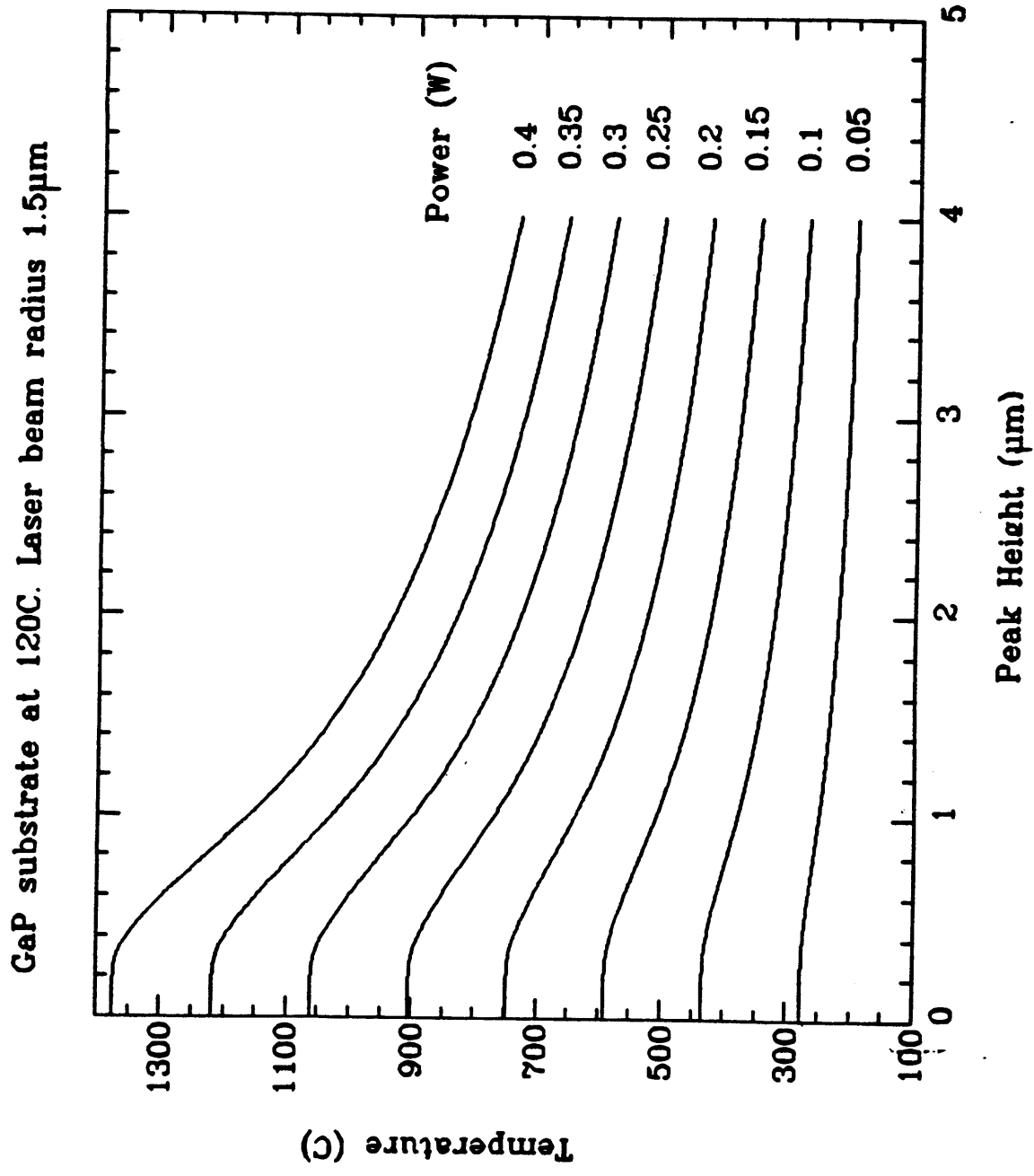
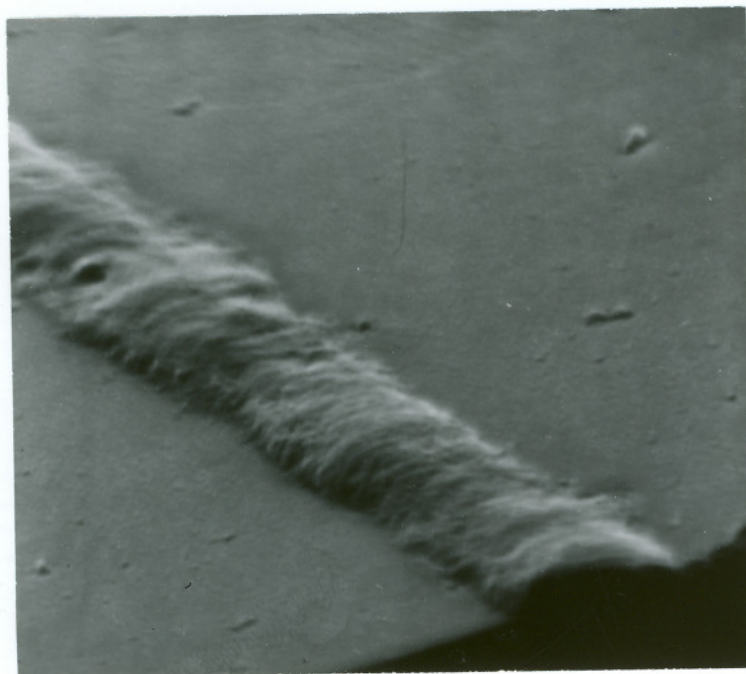


Figure 15. Plot of calculated peak temperature profile vs deposit peak height for different laser powers.

the temperature change with deposit height was less drastic with increasing r_x . Hence in order to avoid the growth rate change during growth with increasing deposit thickness, both the laser power and spot diameter should be optimized to yield minimum temperature change. In general, this is expected to happen for large spot sizes, like $50\mu\text{m}$, however, the resolution of the process is compromised.

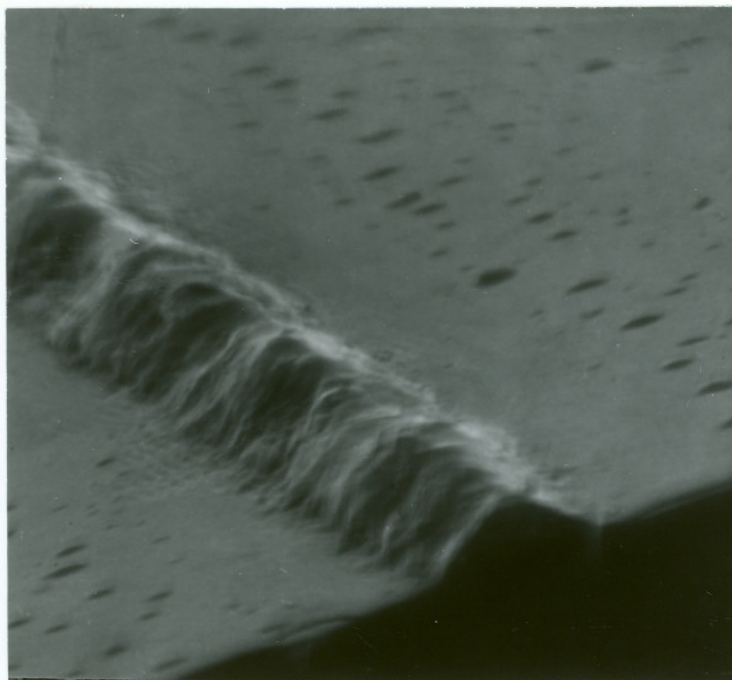
The crystalline properties of the direct-write structures were too small to be examined with an X-ray diffractometer available to us, therefore transmission electron microscopy (TEM) was utilized. Cross-sectional samples were prepared using the standard procedure which includes ion milling. Fig.18 shows a typical electron diffraction pattern of the laser deposited GaP, which verifies epitaxial growth. TEM micrographs have also provided interesting information about defects in the substrate and in the epigrowth. For example, a relatively large number of defects are seen in the far wings of the cross-sectional profile of the deposited structure. This is probably due to low growth temperatures due to the gaussian profile of the laser.

Scanning auger analysis was carried out to determine the carbon and oxygen concentrations in the deposit since the phosphorous source is a metallorganic instead of the conventional hydride, phosphine. Fig.19 is a schematic of a GaP line drawn on GaP that was analyzed. The auger data obtained after 2 minutes of argon sputtering from the three areas marked in the micrograph are shown in Fig.20 a,b&c. Regions 1 and 2 showed substantial concentrations of carbon and oxygen, while the deposit showed negligible amounts. Carbon and oxygen line scans across the deposit as indicated in Fig.21a are shown in Fig.21b. Both C and O concentrations were lower in the deposit than in the substrate. Also, oxygen



(a)

5.0 μm



(b)

Figure 16. SEM micrographs of GaP deposit after (a) 10 scans and (b) 35 scans.

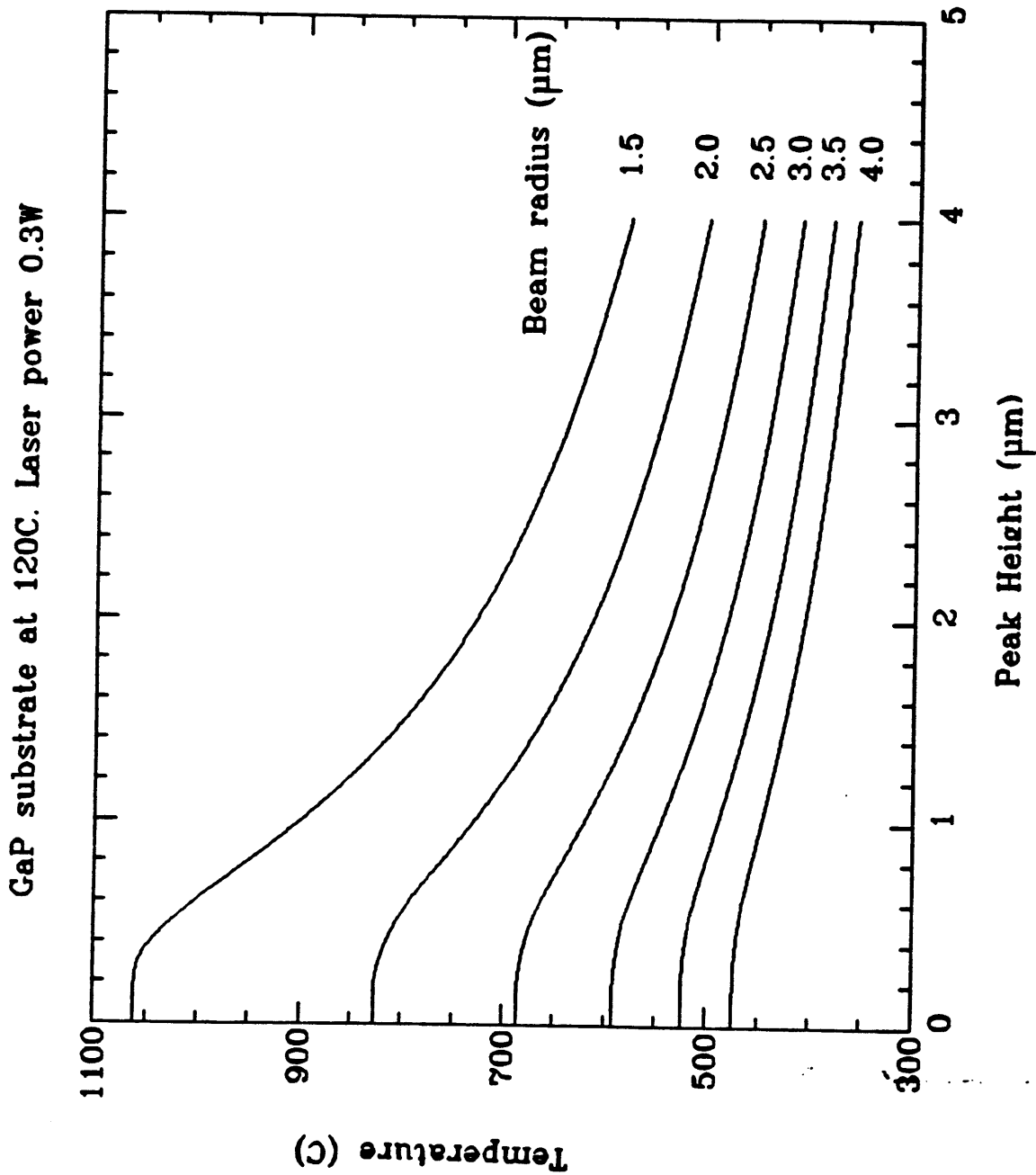


Figure 17. Plot of calculated peak temperature profile vs deposit peak height for different beam radii.



Figure 18. Transmission electron diffraction of the laser deposited GaP. The zone axis is [100].

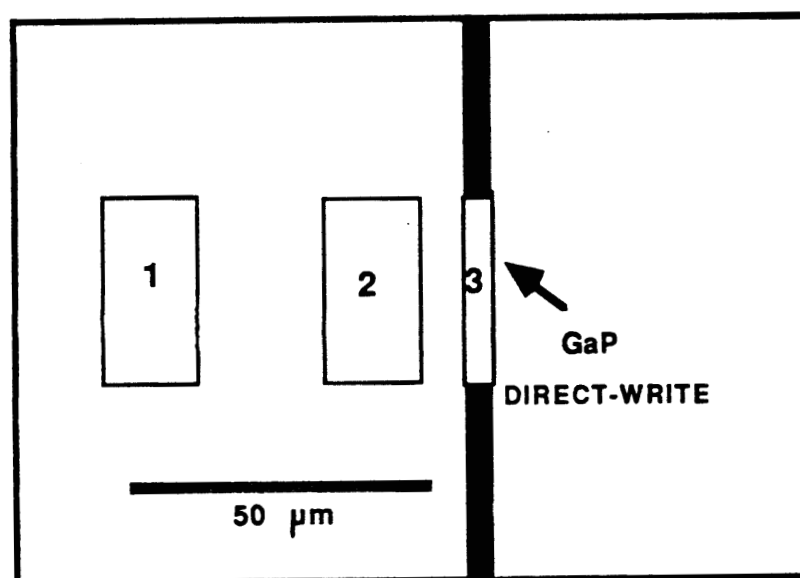
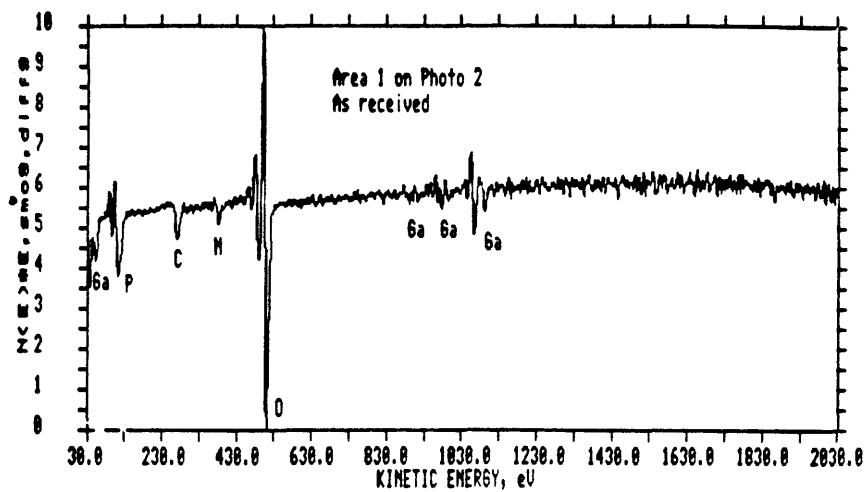
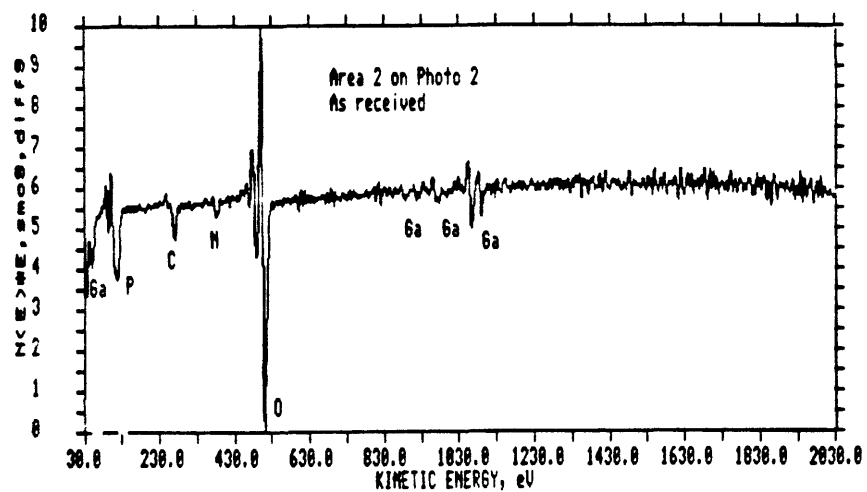


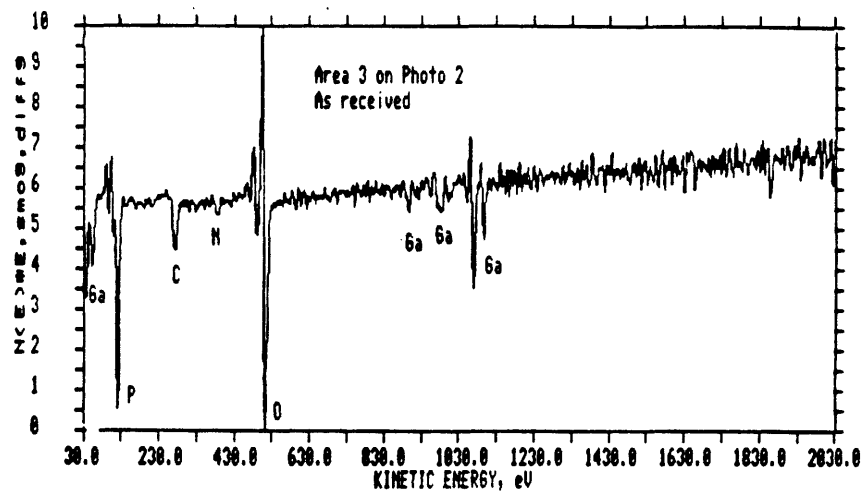
Figure 19. Schematic of the auger area scan



(a)



(b)



(c)

Figure 20. Auger spectrum of the laser deposited GaP at (a) area 1, (b) area 2, and (c) area 3 corresponding to Figure 19.

showed a peak corresponding to the center of the deposit indicating that the deposit probably melted resulting in increased oxygen solubility. Here, it is pertinent to note that the free energy of formation for the gaseous products of carbon and hydrogen i.e., CH_4 , C_2H_6 , etc are increasingly negative with temperature. Hence the extremely high temperatures achieved during the growth is believed responsible for the very low carbon concentration.

Another important growth parameter was the scan speed. Fig.22 shows the dependence of the growth at 3 different scan speeds. At $50 \mu\text{m}/\text{sec}$, although the initial growth rate is high, the profile becomes rough and irregular after a large number of scans. As the scan speed was increased, the profiles became smoother. The data in Fig.22 were obtained at TMG pressure of 4 torr, V/III ratio of 10, and 1 W laser power. Under these conditions best profiles were obtained at a scan speed of $100 \mu\text{m}/\text{sec}$. At higher speeds the lines grown were discontinuous. Other parameters examined included the laser power and the substrate orientation. The epitaxial growth rate initially increased with the laser power and then drops. For example, at TMG partial pressure of 3 torr, V/III ratio 15, and scan speed $100 \mu\text{m}/\text{sec}$, the growth/scan first increased with laser power, then stayed approximately even between 0.9 to 1.2 W range, and then started to drop again. At higher laser powers the cross-sectional profile has a dip in the middle.

All the results reported above were obtained on (100) GaP orientation. Besides (100), (111) orientation was also examined. For the first few scans (10), the growth/scan of the two orientations was about the same. However, as the thickness of the deposit increased with the number of scans, the growth rate on (100) was higher than that on (111) orientation. For example, under the conditions of Fig.13 and a scan speed of $100 \mu\text{m}/\text{sec}$, a corresponding thickness on

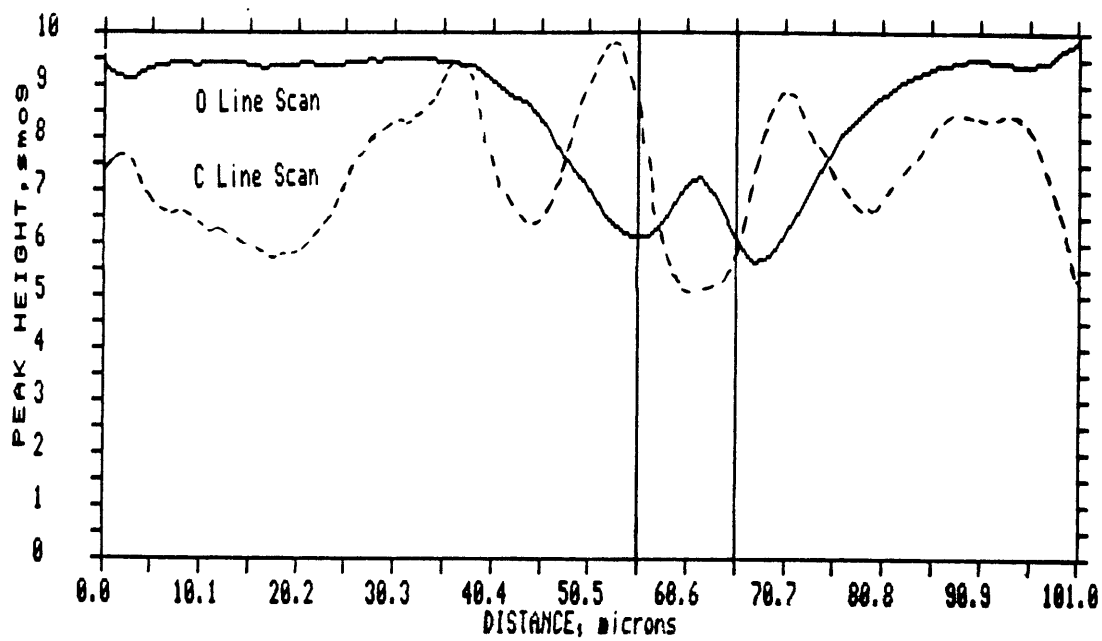
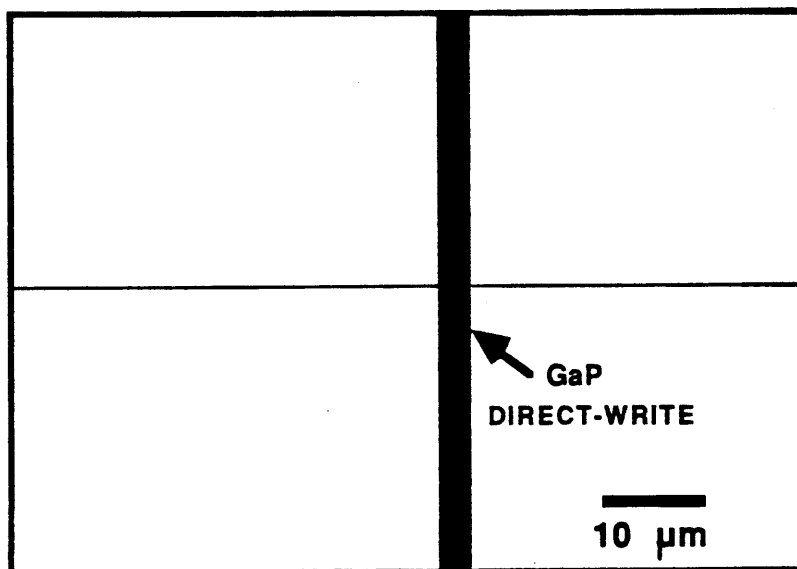


Figure 21. (a) Schematic of the auger line scan and (b) auger line profiles of oxygen and carbon across the deposit.

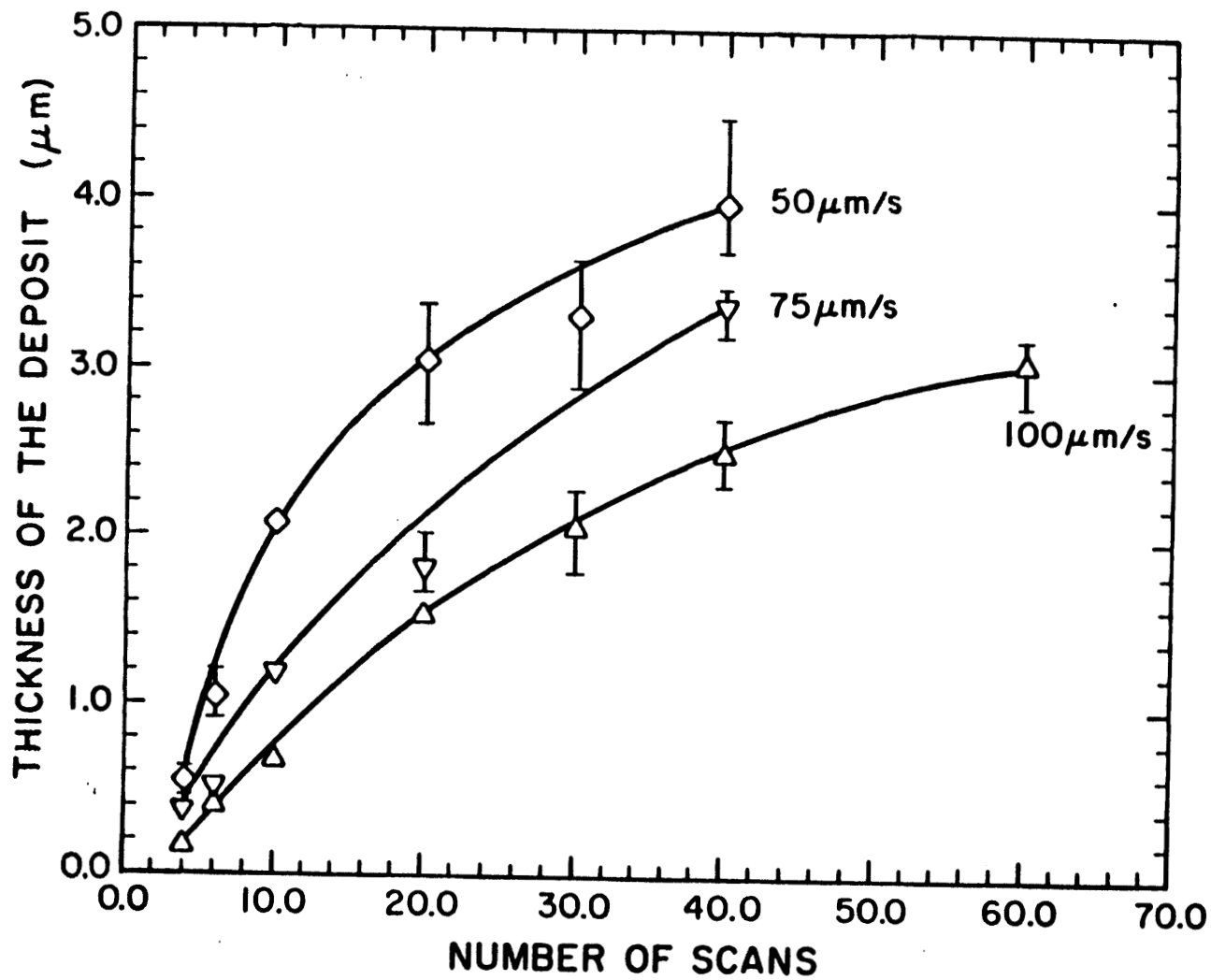


Figure 22. Plot of the dependence of growth on the laser scan speed.

(111) orientation was $2.4\mu\text{m}$ after 60 scans.

4.3 SELECTIVE AREA HETEROEPITAXY OF GaP ON SILICON

4.3.1 INTRODUCTION

Heteroepitaxy of III-V compounds on silicon is of interest for fabrication of monolithic optoelectronic integrated circuits. Here a laser induced deposition process for heteroepitaxy of GaP on silicon wafers (0.4% lattice mismatch) is described.

4.3.2 RESULTS AND DISCUSSION

Low growth rates were used in order to obtain epitaxial films by lowering the concentrations of the precursors and using low-power, multiple laser scans. Typical deposition parameters for epigrowth were as follows: the substrate temperature was 200°C , laser power of 0.4 W, scan speeds of 50-125 $\mu\text{m/s}$, TMG partial pressure of 2 Torr and V/III ratio of 15. The thickness of the deposits was controlled with the laser power, scan speed and the number of scans, where the growth was about 0.1 $\mu\text{m/scan}$. The general trends of the relationships between the epitaxial growth and the growth parameters were similar to those obtained for homoepitaxial GaP. Smooth continuous lines and pads (by raster scanning the lines) were deposited in the path of the moving focused laser spot. Auger analysis of the structures grown under the above conditions were found to be stoichiometric (50% atomic Ga and 50% P). Incorporation of carbon was found to be negligible.

Two examples of GaP microstructures are presented in Fig.23 and 24. Scanning electron micrograph of the 'direct-write' lines is shown in Fig.23. By raster

scanning these lines, a pad can be grown, which is illustrated in the Nomarski micrograph of Fig. 24. The crystalline properties of these microstructures was determined using XTEM. An example of the transmission electron diffraction pattern of the film is shown in Fig.25. The streaking along the (111) plane indicates that it has some degree of polycrystallinity. Extra spots observed could be due to double diffraction. These results indicate that the heteroepitaxial film has some defects.

In summary, laser induced homo- and heteroepitaxy of GaP on silicon has been demonstrated. Growth of microstructures was obtained without the use of photolithographic processes. However, it is evident that the process was slow because of the repeated scanning involved in the growth. Also only a single structure at a time could be fabricated. The objective was to achieve selective area processing with much higher throughput. Hence the use of excimer lasers for selective epitaxial growth was investigated, since the laser has a large area output. The results from this investigation are discussed in the following sections.

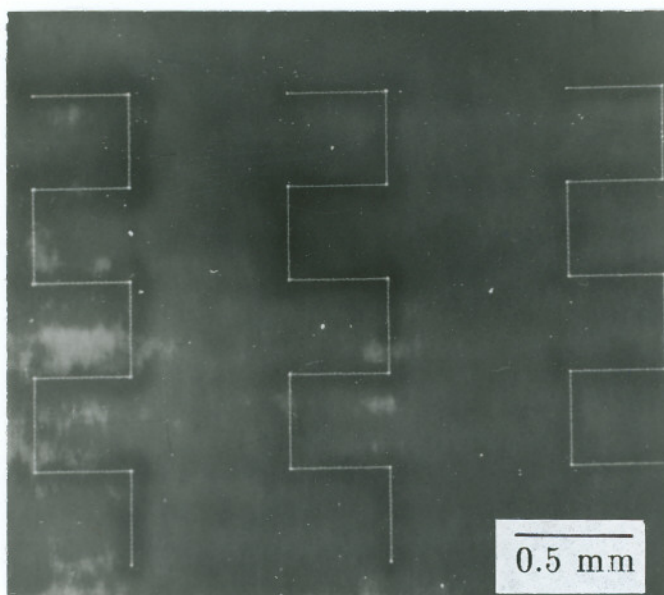


Figure 23. SEM micrograph of laser deposited GaP lines on Si

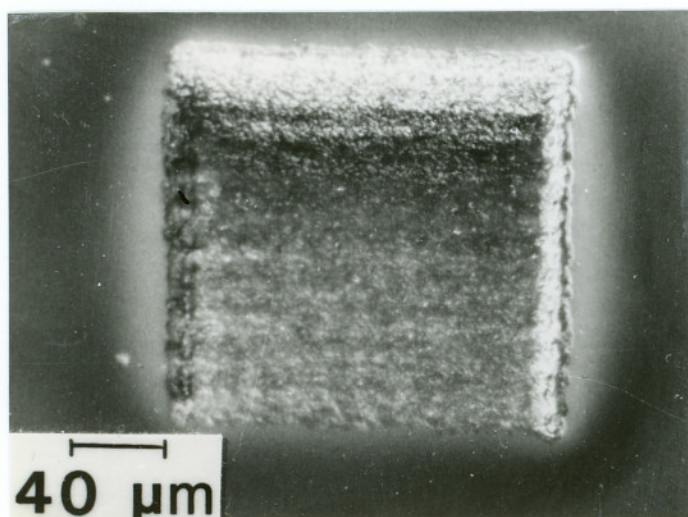


Figure 24. Nomarski micrograph of a GaP pad grown on Si. The pad thickness is about 3 microns.



Figure 25. TEM diffraction pattern of a GaP microstructure on Si showing epitaxial alignment. The zone axis is [110].

4.4 EXCIMER LASER ASSISTED SELECTIVE EPITAXY OF GaP

Excimer lasers can be used to selectively grow compound semiconductors with high throughput because of their large beam area. Also, selective area growth can be realized using different chemical process routes by varying the excimer laser wavelength. For example, when 193nm from an ArF laser is used as the photon source (under normal incidence) to deposit gallium using trimethyl gallium as the precursor gas, there are possibilities for

- a. gas phase dissociation of TMG
- b. adsorbed layer photo-dissociation/pyro-dissociation of TMG
and
- c. laser-induced heating and recrystallization; this allows lower substrate temperatures.

However, if 351nm excimer output is used (XeCl) as the photon source, photodissociation of TMG is very unlikely both in the gas phase as well as in the adsorbed phase because of its low absorption cross-section at this wavelength (36). Thus the only possibility is adsorbed layer pyrolysis which again results in a high degree of area selectivity during growth (37).

The use of UV radiation (ArF, 193nm) from an excimer laser was investigated as a photon source to achieve spatially selective epitaxial growth of GaP at low substrate temperatures compared to conventional OMVPE. Low temperature epitaxy of thin films of III-V compounds offers sharp interfaces and reduced stress due to mismatched thermal expansion coefficients during heteroepitaxy.

Reduction of growth temperature without providing sufficient energy leads to poor film quality and in worst case, polycrystalline or even amorphous growth.

Epitaxial growth at low substrate temperature was achieved by making use of the high energy laser photons (6.4eV) to assist in dissociating the precursor gases and increasing surface mobility of the adatoms on the surface for epitaxy.

The initial approach was to use very low substrate temperatures and grow homoepitaxial GaP. This approach, however, did not prove to be very useful in obtaining epitaxial film even though polycrystalline GaP was selectively grown where the laser was incident on the substrate. Hence, it was decided to sacrifice the high degree of area selectivity to some extent for improved crystalline quality by increasing the substrate temperature to 500°C. This led to some thermal deposition which will be compared with photo-thermal deposition in the following sections.

Homoepitaxial growth of GaP is discussed and compared at various operating parameters in section 4.5. In section 4.6 a unique observation made during the examination of GaP grown at high temperature (600°) is discussed. Heteroepitaxy of GaP on GaAs and comparison of defect structures in GaP/GaP and GaP/GaAs are discussed in section 4.8. This is followed by the discussion of the periodic structure formation during heteroepitaxial growth of GaP in section 4.9. Section 4.10 deals with the results we obtained during electrical conductivity measurements of GaP under laser irradiation to determine the effect of laser pulsing on substrate heating.

4.5 HOMOEPITAXY OF GaP

4.5.1 INTRODUCTION

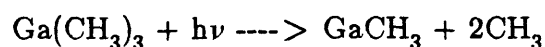
An ArF excimer laser was used to assist selective epitaxial growth of GaP. The precursor gases for gallium and phosphorus were trimethyl gallium (TMG) and tertiarybutyl phosphine (TBP) respectively. Initial experiments were carried out at atmospheric pressure with the substrate held at 300°C. Growth in the absence of laser irradiation was negligible and when the laser was focussed on to the substrate, it was fine grained/amorphous in nature.

At 300°C, neither TMG nor TBP is thermally dissociated (38,39) and when the laser is turned on, due to strong absorption at 193nm (36,40), there was photodissociation of precursor gases resulting in a film growth. However, because of low laser fluences or high gas phase nucleation of GaP molecule at high system pressure, only polycrystalline deposit was obtained. In order to achieve epitaxy, three major system parameters were changed. The first being the reactor pressure, was decreased from 760 torr to 15 torr in order to reduce specie dwell time and hence the gas phase nucleation possibility. The other two changes were increasing the substrate temperature and the laser power density. These would enhance the adatom mobility and hence favor epitaxial growth. Various system parameters were studied and are discussed below.

4.5.2 PHOTON-INDUCED DISSOCIATION

It is known that TMG strongly absorbs radiation at 193 nm resulting in the dissociation of the molecule and formation of atomic gallium through a two-photon process (36). The absorption spectrum of TMG is a continuum that starts at

260nm and peaks at 200 nm (Fig.26). The primary photoprocess at 193nm is



The secondary photoprocess is



with the absorption cross-section of $4 \times 10^{-17} \text{ cm}^2$.

There is no literature available on the UV photon absorption characteristics of TBP. Therefore, mass spectrometric studies were performed which showed that 193 nm photons do dissociate TBP molecules giving elemental phosphorous and hydrocarbon fragments. A typical spectrum of the photoproducts seem during 193nm irradiation in the presence of TBP is shown in Fig.27. However, a detailed examination of its dissociation characteristics was beyond the scope of the present investigation and hence will not be discussed further.

4.5.3 GROWTH CHARACTERIZATION

The dependence of GaP growth rate on the substrate temperature was examined first. Growth rate of GaP versus the substrate temperature at two laser power densities is shown in Fig.28. With a laser energy density of 0.06 J/cm^2 the growth rate first increased with substrate temperature up to 300°C , which is similar to the kinetically controlled regime of a conventional metalorganic vapor phase epitaxy (MOVPE) process. At higher substrate temperatures, the growth rate was uniform and then dropped above 500°C . Cross-sectional transmission electron microscope analysis of the films grown over this entire temperature range showed them to be composed of large polycrystalline columnar grains. When the laser energy density was increased to 0.1 J/cm^2 , the growth rate was higher as expected due to higher photon induced dissociation rate of the

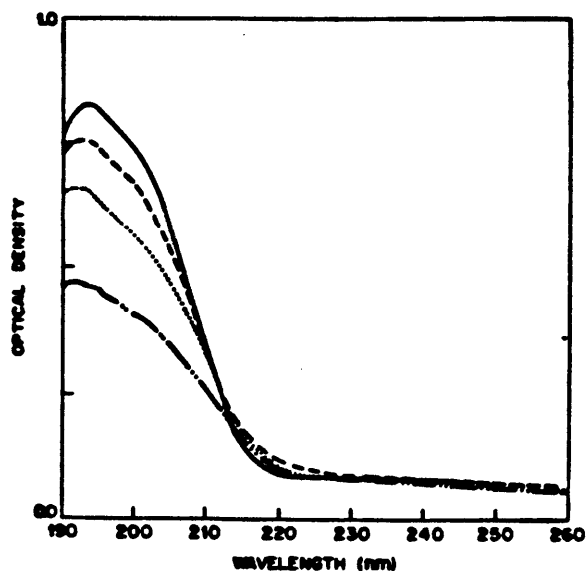


Figure 26. Comparison of trimethylgallium absorption as a function of temperature. Pressure = 0.3 Torr, path length = 7.5 cm.
 (-----) 25C, (-----) 100C, (. . .) 200C, (- - -) 300C.

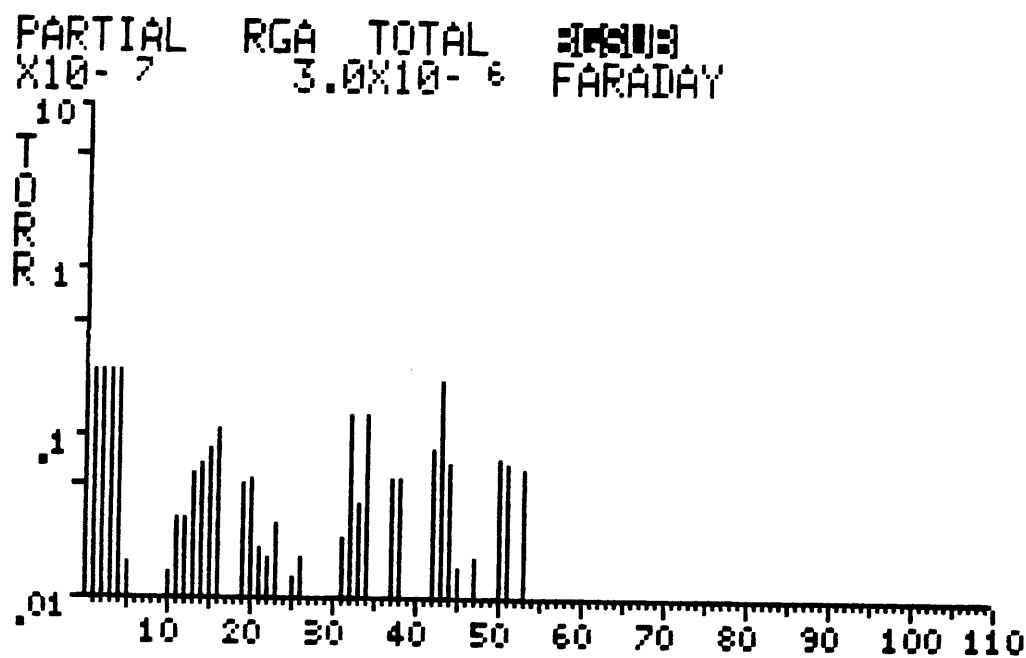


Figure 27. Mass spectrum obtained during laser irradiation in the presence of tertiarybutylphosphine. Note the absence of peak at mass 90 corresponding to TBP.

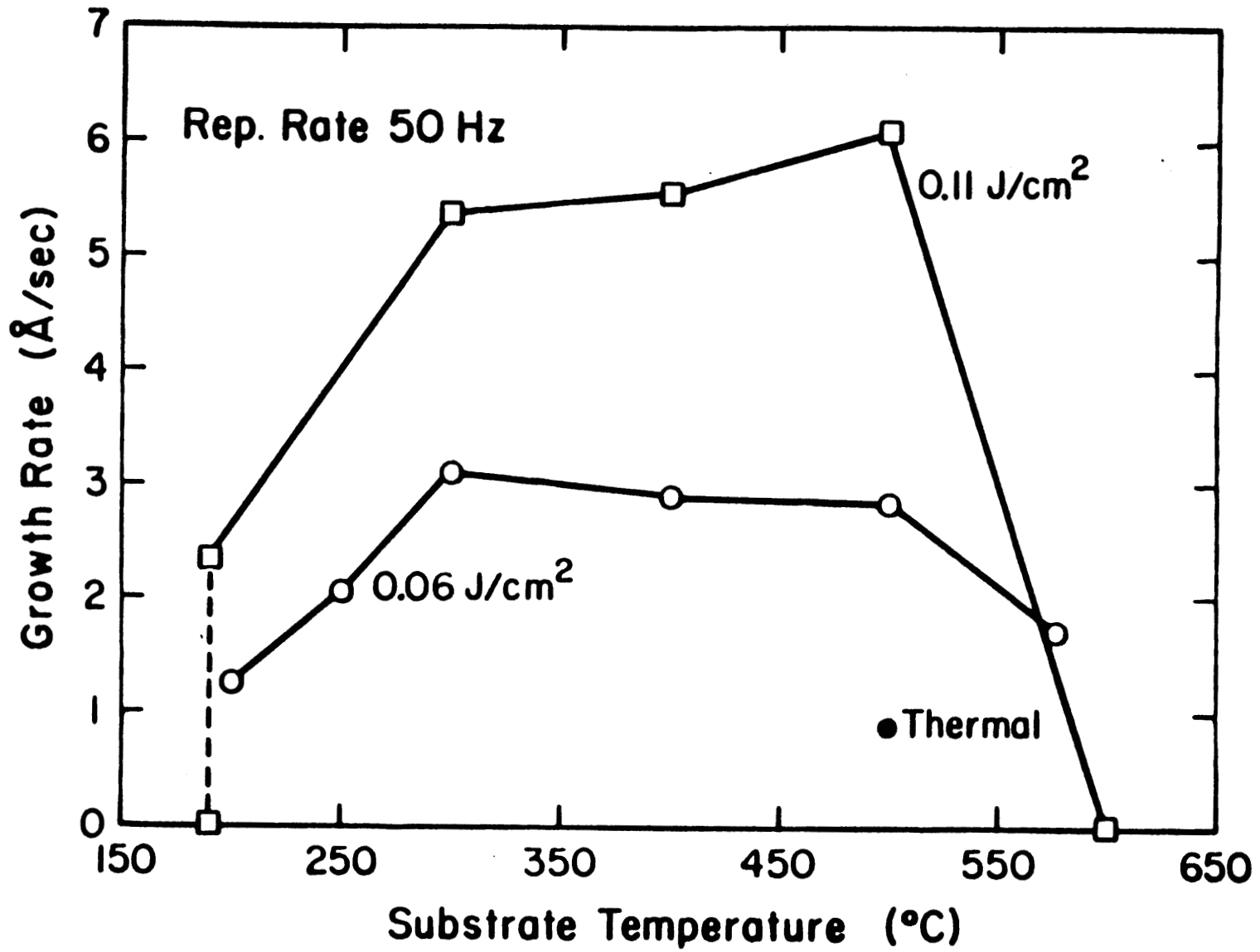


Figure 28. Plot of growth rate of GaP versus the substrate temperature at 0.06 and 0.11 J/cm² laser energy density.

precursor gases. Films grown below 200°C peeled off and at 300 and 400°C were polycrystalline. The surfaces of these growths appeared to be cracked (Fig.29) probably due to decohesion of the films from the substrate which was observed with XTEM (Fig.30). In case of silicon, time resolved x-ray diffraction measurements have shown that the surface is severely strained during pulsed laser irradiation (41). This strain is thought to be due to simultaneous normal thermal expansion and lateral clamping of the lattice (the latter due to the cool part of the sample outside the laser beam), resulting in a uniaxial stress with symmetry axis perpendicular to the sample surface. Similar stress could be responsible for the film cracking and decohesion at low growth temperatures. Moreover at low substrate temperatures, because of low migration of atoms there could be a residual stress build-up in a film deposited at relatively high rates under high laser fluences. Such residual stress could also lead to decohesion involving film cracking, followed by cracking of the substrate parallel to the interface (42). At 500°C the films were free of cracks and the growths were epitaxial. In comparison, films deposited at the same temperature but without the laser (Fig.31) had a fine grain polycrystalline morphology. At substrate temperatures above 500°C, the growth rate of the films deposited with the laser dropped. Initially this drop was believed to be due to a diffusion limited regime which is observed in conventional MOVPE. A closer inspection, however, showed these films to be sputtered (Fig.32). This kind of sputtering of different materials using an excimer laser is well documented in the literature (43). Dependence of growth rate on laser pulse rate and the power density were also investigated. The growth rate increase with the pulse rate up to 80 Hz (upper limit of the laser) which was expected due to higher rate of photodissociation. However, the growth rate per pulse dropped

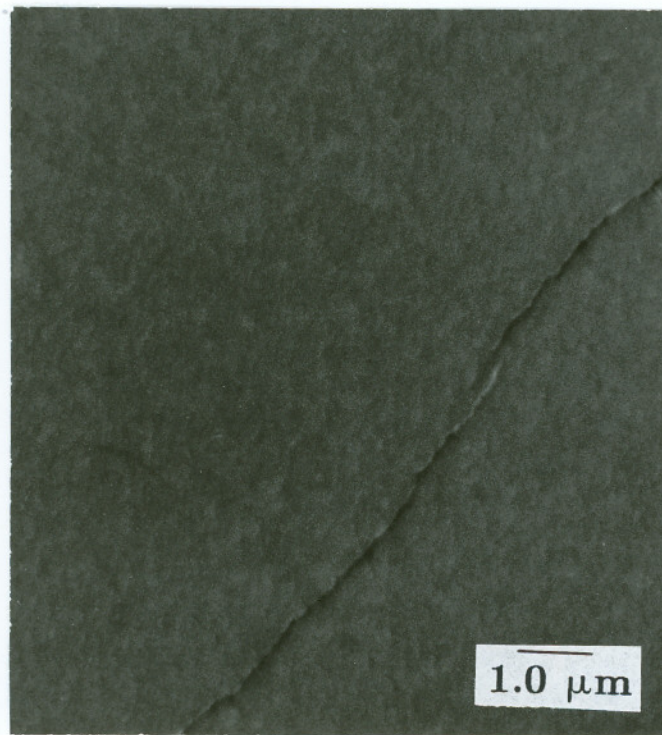


Figure 29. SEM micrograph of GaP deposited at 300°C.

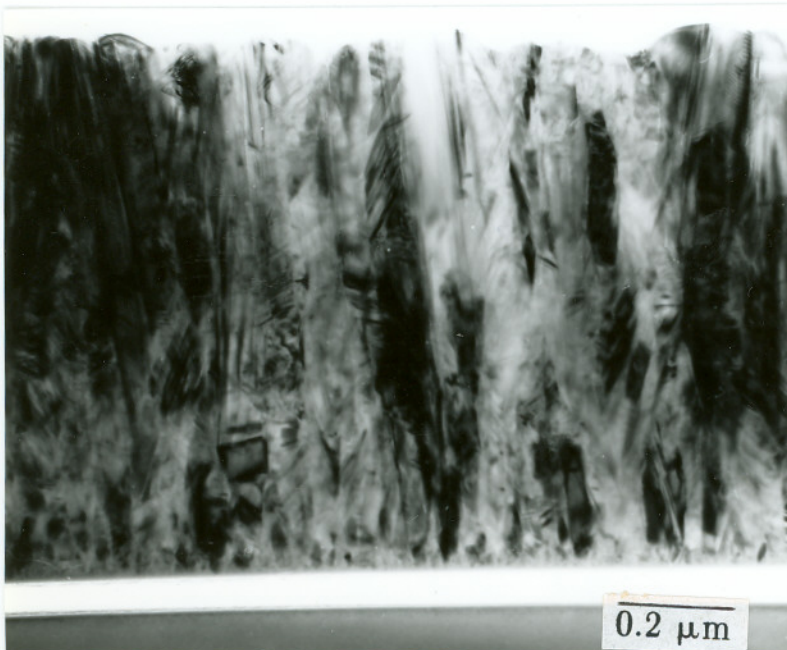
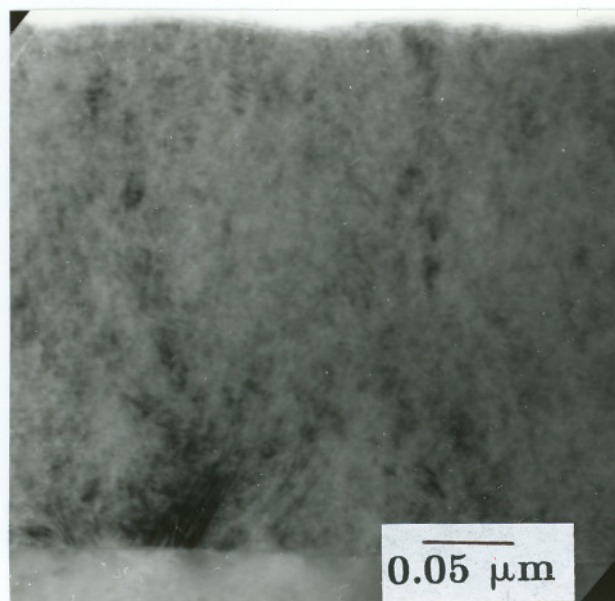
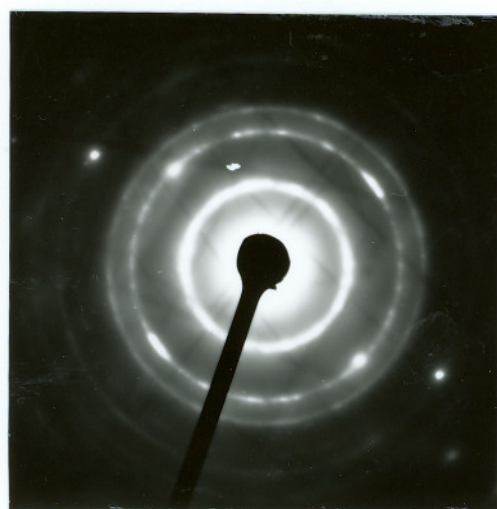


Figure 30. Cross-sectional TEM micrograph of the above deposit showing a cracked interface.



(a)



(b)

Figure 31. (a) Cross-sectional TEM view of the thermally grown (500C) GaP film and (b) its corresponding transmission electron diffraction pattern showing the fine grain polycrystallinity.

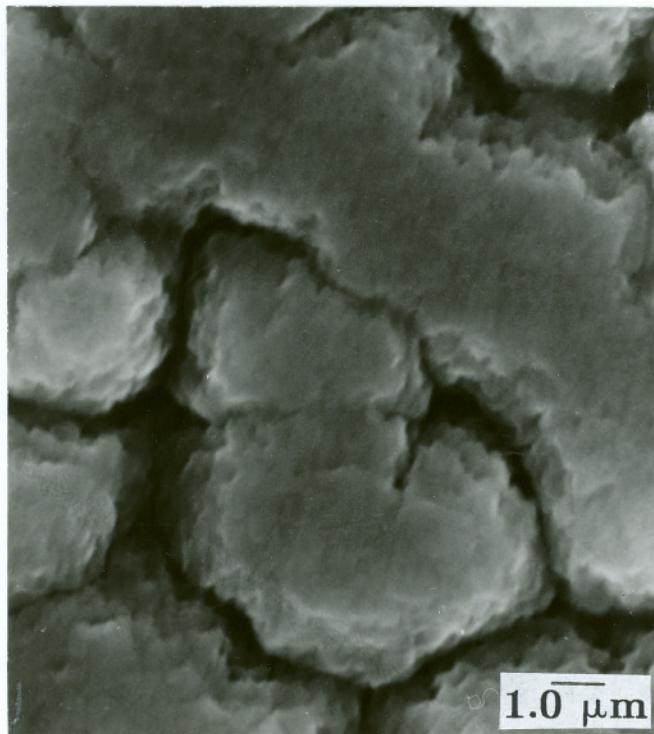


Figure 32. SEM micrograph of the laser sputtered GaP deposit.

(Fig.33) with increasing laser repetition rate indicating the limited supply of fresh gas to the photolysis volume. The growth rate of GaP versus laser power density at 500°C is shown in Fig.34. The growth rate as well as the grain size increased with laser energy. At about 0.1 J/cm^2 (substrate temperature 500°C) epitaxial growth was achieved. Beyond about 0.12 J/cm^2 , sputtering started to dominate and the growth rate dropped. The phase change from polycrystalline to single crystal was believed to be due to the transient heating by the pulsed laser radiation. This was further checked by changing the laser wavelength to 248 nm (KrF) where the absorption of TMGa and TBP was significantly lower than at 193 nm (36). All the other conditions were kept the same. However, only polycrystalline films were obtained suggesting that both photochemical and transient heating processes were responsible for assisting epitaxial growth at this temperature. No significant difference was observed when the laser power density was adjusted to compensate for the different reflectivities at the two wavelengths (experimentally determined reflectivities, 0.39 at 193 nm and 0.48 at 248 nm). It is interesting to note that even at a temperature of 600°C, the purely thermal film growth consisted of pyramid-like structures with spherical tips that were determined to be polycrystalline. A unique crystalline morphology observed in these structures is discussed in detail section 4.6.

The crystalline properties of the GaP films grown at 500°C without the laser and with 0.11 J/cm^2 laser radiation are shown in Figs.31 and 35, respectively, with corresponding growth rates indicated in Fig.28. The XTEM view of the thermal growth (Fig. 31a) shows a fine grained polycrystalline morphology. This is confirmed by the transmission electron diffraction pattern shown in Fig.31b. In the presence of laser radiation (0.11 J/cm^2) epitaxial growth was achieved as

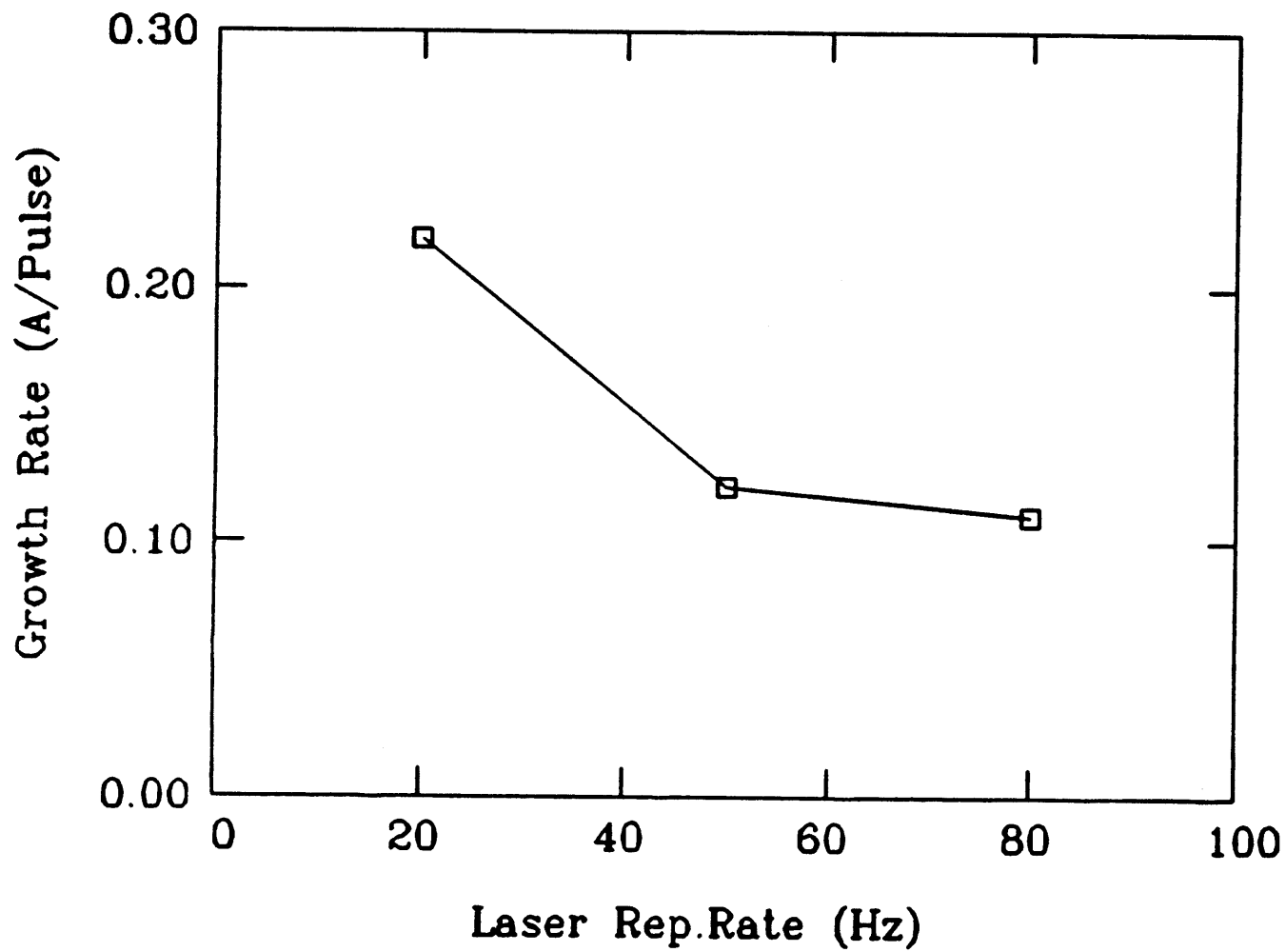


Figure 33. Plot of growth rate vs. laser repetition rate at laser energy density of 0.11 J/sq.cm and 500 °C.

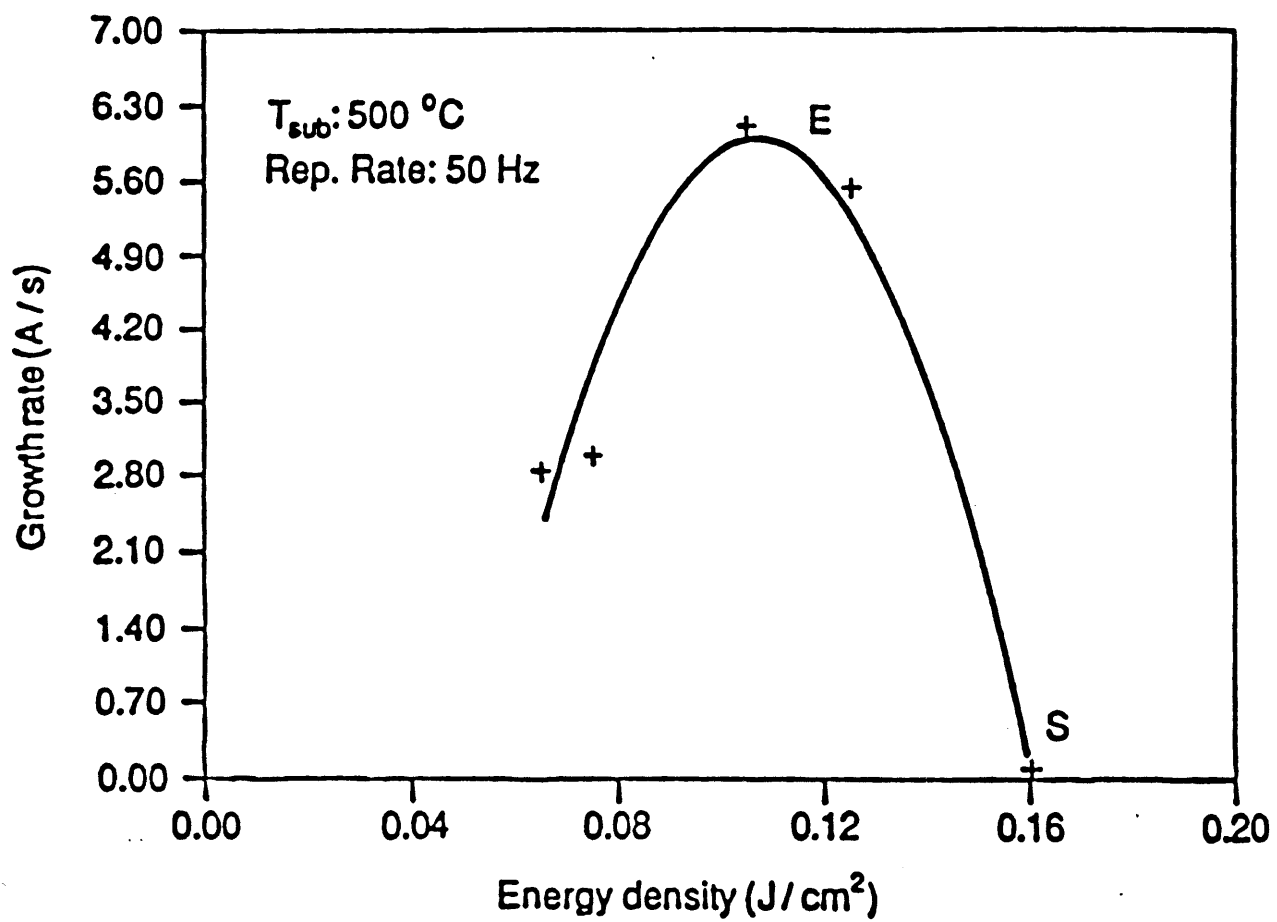


Figure 34. Plot of growth rate vs. laser energy density.



(a)



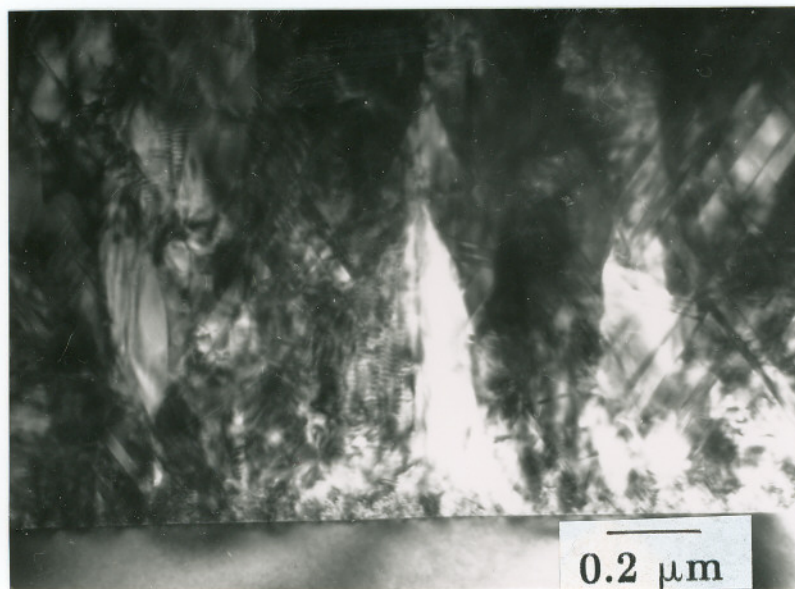
(b)

Figure 35. (a) Cross-sectional TEM view of the excimer laser assisted grown (500C) GaP film showing the epitaxial growth. (b) Transmission electron diffraction pattern along [110] zone axis.

shown in Fig.35a, which is again an XTEM view. There is a high density of twins which are thought to accommodate the stress induced during growth. Extensive twinning of the film in combination with double diffraction effects result in the appearance of the extra spots in the transmission electron diffraction pattern at $1/3$ and $2/3$ distances along $\langle 111 \rangle$ as shown in Fig.35b. Therefore, by comparing the two conditions, it is evident that the presence of laser radiation, in addition to an enhancement in the growth rate (by a factor of 6 at 500°C) also substantially improved the crystalline quality of the deposit.

However, the crystalline quality of the deposit was not uniform across the spot. XTEM diffraction pattern close to the edge of the growth showed streaking (Fig.36b) and the defect density was too high to be resolved in the bright field XTEM micrograph (Fig.36a). This can be explained based on the fact that the laser energy is not uniform across the spot; this resulted in different degrees of crystallization during growth. However, such inhomogeneity can be avoided either by masking off edges of the beam or by using a beam homogenizer.

The effect of reactor pressure on the crystalline quality of the films grown at 500°C was studied for a constant laser energy density of 0.11 J/cm^2 . At pressures close to 1 atm., polycrystalline films were obtained. This was probably due to a high rate of gas phase dissociation followed by nucleation. A reduction in the pressure to 14 torr dramatically improved the quality of the epitaxial growth. This is illustrated in Figs.37a and 37b which show the bright field XTEM micrograph and its corresponding electron diffraction pattern along $[110]$. There is a marked absence of the extra spots in the diffraction pattern which are present in Fig.35b due to twinning at 30 torr. TEM tilting analysis revealed the presence of stacking fault-like defects in addition to dislocations. A $(111)\text{-g}$, g weak beam



(a)

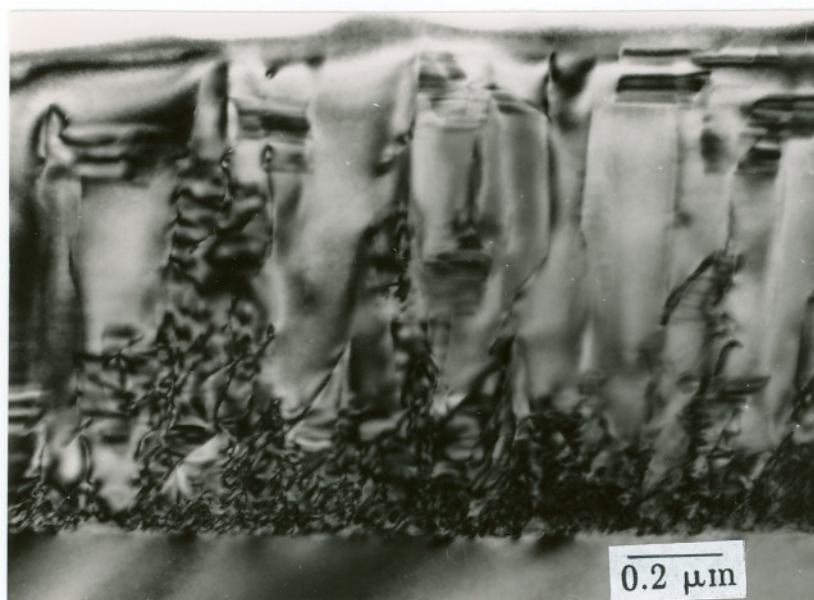


(b)

Figure 36. Cross-sectional TEM micrograph of GaP grown away from the center of the beam spot. (b) Transmission electron diffraction pattern along [100] zone axis showing a degree of polycrystallinity.

image of the film shown in Fig.38 clearly demonstrates the presence of these faults and the absence of twins on (111). The profound effect of pressure on the crystalline quality of the deposit is in direct contrast to the results reported for the excimer laser assisted epitaxial growth of Ge on GaAs, with the laser in parallel geometry (44). Such substantial improvements in the film crystalline property in the present experiments with decreasing reactor pressure could be either due to an increased laser fluence reaching the substrate, thus influencing transient annealing or the decreased cooling effect of hydrogen.

The extent of the cooling effect was investigated by monitoring the electrical conductivity of a thin GaP substrate following exposure to one or a series of laser pulses. Initially, the conductivity was calibrated with respect to the substrate temperature in the absence of laser radiation. Next, the change in conductivity during laser irradiation and at different reactor conditions (H_2 , He buffer gases, pressures) were recorded every 100 msec with a computerized system. Photogenerated voltages were also taken into account. The conductivity was first recorded at low pressure (10^{-4} torr) and then He or H_2 was introduced slowly. At a buffer gas pressure of 0.1 torr, there was a dramatic drop in the steady-state conductivity. As He or H_2 pressure was increased, the change in the conductivity at higher pressures was smaller. The difference in conductivity between 15 and 30 torr of H_2 was small compared to the change between 0.1 and 1 torr. Hence, the main reason for the difference in the crystalline property of GaP grown at 10 torr and 30 torr was not considered to be the cooling effect. The results of the above mentioned investigation are presented in detail in chapter 4.10.



(a)



(b)

Figure 37. (a) Bright field cross-sectional TEM view of the epitaxial GaP film grown at 14 Torr total pressure. (b) Transmission electron diffraction pattern along $[110]$ zone axis.

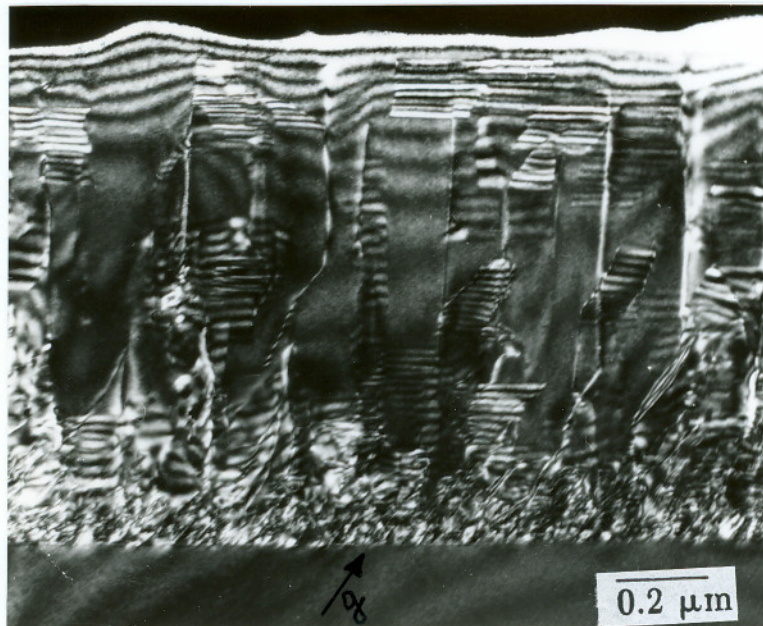


Figure 38. Weak beam (111) -g, g image of the film grown at 14 Torr showing the absence of twins on (111).

4.5.4 ELECTRICAL CHARACTERIZATION

Electrical properties of the laser grown epitaxial films were examined by characterizing p-n diodes fabricated by growing Zn doped GaP on the n-type substrates. Typically 40 sccm of 50 ppm dimethylzinc in He was flowed during the growth of GaP. After the growth of about 1.5 μm thick film, ohmic contacts were obtained by evaporating and alloying Au-5% Zn on the p-type film and Au-12%Ge- % on the n-type substrate. Contacts were alloyed at 425°C for 2 minutes in nitrogen atmosphere in a rapid thermal unit. The substrate was scribed and cleaved to 3 mm² slices. Current-Voltage characteristics were measured using a Tektronix programmable curve tracer and the capacitance -voltage characteristics were measured using a micromanipulator C-V plotter. Before going into the experimental results, the theory behind p-n junction analysis is discussed briefly in the following sections.

4.5.4.1 CAPACITANCE IN A P-N JUNCTION

When electron donor (n-type) and electron acceptor (p-type) materials of a semiconductor are joined together electrically, diffusion of charge carriers occurs because of large gradient of charge carriers at the junction. Electrons leaving from n to p region creates N_{A+} in the n region due to the remaining immobile charges. This creates a positive space charge near the p-n junction. A similar negative space charge is created in the p region because of the flow of holes. These regions constitute the depletion width, W (which is depleted of mobile carriers). Further flow of carriers is arrested by the electric field setup across the depletion region. The depletion width under an external bias is given the relation (45)

$$W = [2\epsilon_s(\phi_i - V)/q (1/N_a + 1/N_d)]^{1/2} \quad (4.9)$$

where ϵ_s is the permittivity of the semiconductor, ϕ_i is the built-in voltage, q is the electronic charge, N_a and N_d are the acceptor and donor concentrations and V is the applied external bias. It is clear that the width W decreases with forward bias. This is because the applied voltage moves majority carriers towards the edges of the depletion region where they neutralize some of the space charge. For any highly asymmetric P^+N junction (abrupt junction), with $N_d \ll N_a$, eq. 4.9 reduces to

$$W = [2\epsilon_s(\phi_i - V)/(qN_d)]^{1/2} \quad (4.10)$$

The depletion-layer capacitance per unit area is defined as

$$C \equiv dQ_c/dV \quad (4.11)$$

where dQ_c is the incremental increase in charge per unit area upon an incremental change of the applied voltage dV . For one-sided abrupt junctions, the capacitance per unit area is given by

$$C \equiv dQ_c/dV = d(qN_d W)/d[qN_d/2\epsilon_s W^2] = \epsilon_s/W \quad (4.12)$$

or

$$C = [q\epsilon_s N_d / 2(\phi_i - V)]^{1/2} \quad (4.13)$$

Equation 4.13 can be written as

$$1/C^2 = 2(\phi_i - V)/(q\epsilon_s N_d) \quad (4.14)$$

or

$$\frac{d(1/C^2)}{dV} = 2/q\epsilon_s N_d \quad (4.15)$$

It is clear from eqs. 4.14 and 4.15 that by plotting $1/C^2$ versus $-V$, a straight line should result for a one-sided abrupt junction. The slope gives the impurity concentration of the substrate (N_d), and the intercept at $1/C^2 = 0$ gives ϕ_i . Hall mobility measurements yielded an acceptor doping concentration N_a of 10^{20} cm^{-3} . A plot of the square of the reciprocal capacitance versus the bias voltage is shown in Fig.39. The linear relationship between the voltage and the square of the reciprocal capacitance indicates that the junction was abrupt. A built-in voltage of 1.78 V was obtained from the plot.

4.5.4.2 Currents in P-N junction

Diffusion of charge carriers due to concentration gradient leads to diffusion current. Space charge in the depletion region creates an electric field that induces a drift current from n to p region opposing the diffusion current. Under zero bias, there is no net current flow across the junction. The total current in a P-N junction is given by

$$J = J_s(e^{qV/kT} - 1) \quad (4.16)$$

where

$$J_s = qD_p \frac{P_{no}}{L_p} + qD_n \frac{N_{po}}{L_n} \quad (4.17)$$

Equation 4.17 is the celebrated Shockley equation (46), which is the ideal diode law. Under reverse bias, the current is simply equal to J_s . The Shockley equation adequately predicts the current-voltage characteristics of germanium p-n junctions at low current densities. For Si and III-V compound semiconductor p-n

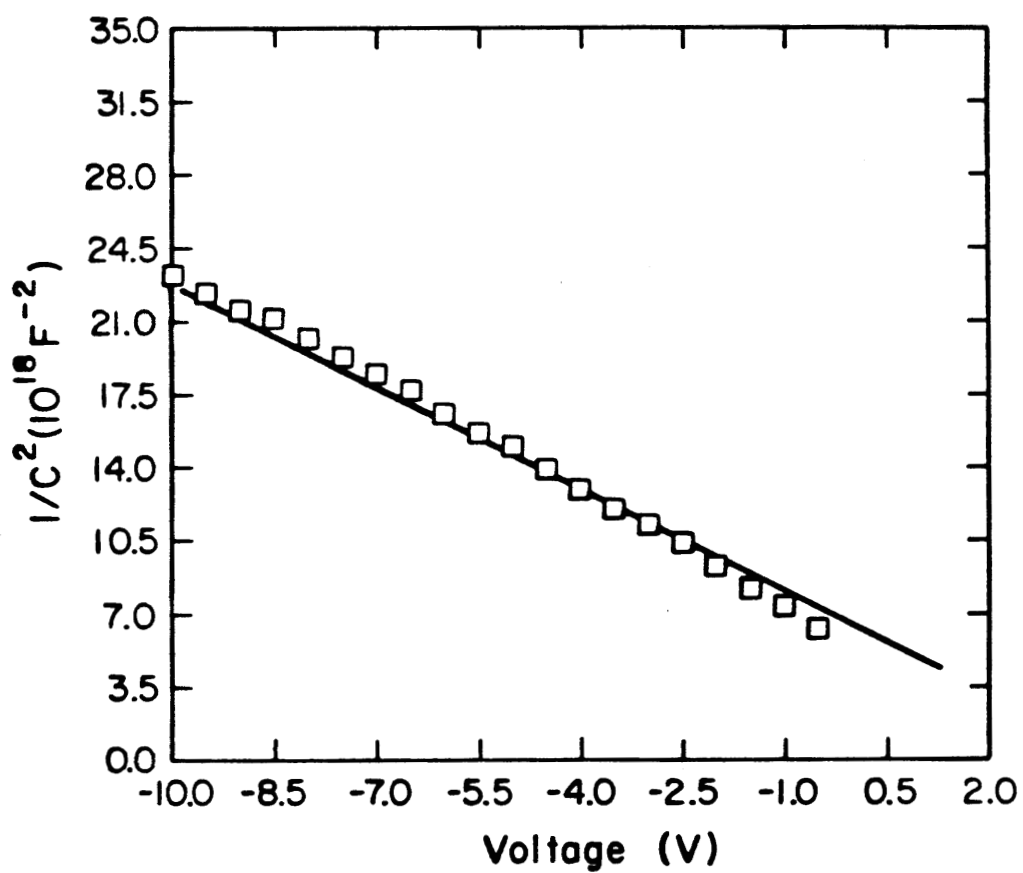


Figure 39. C-V characteristics of a p-n diode fabricated using laser epitaxy.

junctions, however, the ideal behavior can only give qualitative agreement. The departure from the ideal are mainly due to:

- (a) the surface effect,
- (b) the generation and recombination of carriers in the depletion region,
- (c) the tunnelling of carriers between states in the band gap,
- (d) the high injection condition that may occur even under small forward bias and (e) the series resistance effect.

In addition, under sufficiently larger field in the reverse direction, the junction will break down (as a result of avalanche multiplication).

The non-ideal diode equation is written as

$$J = J_s \exp(qV/nkT) \quad (4.18)$$

where q is the electronic charge, k the Boltzmann constant and n the ideality factor. The forward I-V characteristics of this diode at 300 K are shown in Fig.40. At room temperature two regions were observed; one corresponds to $n = 2$ (region I) at higher current density and another (region II) at lower current density with $n = 6.6$. In region I, the current is dominated by recombination in the depletion region, whereas region II indicates presence of tunneling current which is consistent with extreme doping concentration in the p-region (47).

The reverse I-V characteristics (at 300 K) are also shown in Fig.40, where the breakdown voltage was 39 V. In the pre-avalanche region, the current density varies as

$$J = 3.47 \times 10^{-7} V^{2.63} \quad (4.19)$$

Such a power dependence of reverse current has been shown to be due to a tun-

neling mechanism [47].

SUMMARY

In summary, excimer laser induced epitaxial growth of GaP was studied using TBP, a new phosphorous precursor. High growth rates were achieved in the presence of laser irradiation at relatively low substrate temperatures. The epitaxial growth was dependent over a narrow range of various parameters such as the substrate temperature, laser wavelength, pulse energy, and reactor pressure. Electrical properties of p-n diodes fabricated using laser epitaxy exhibited similar characteristics to those made at higher temperatures using conventional methods.

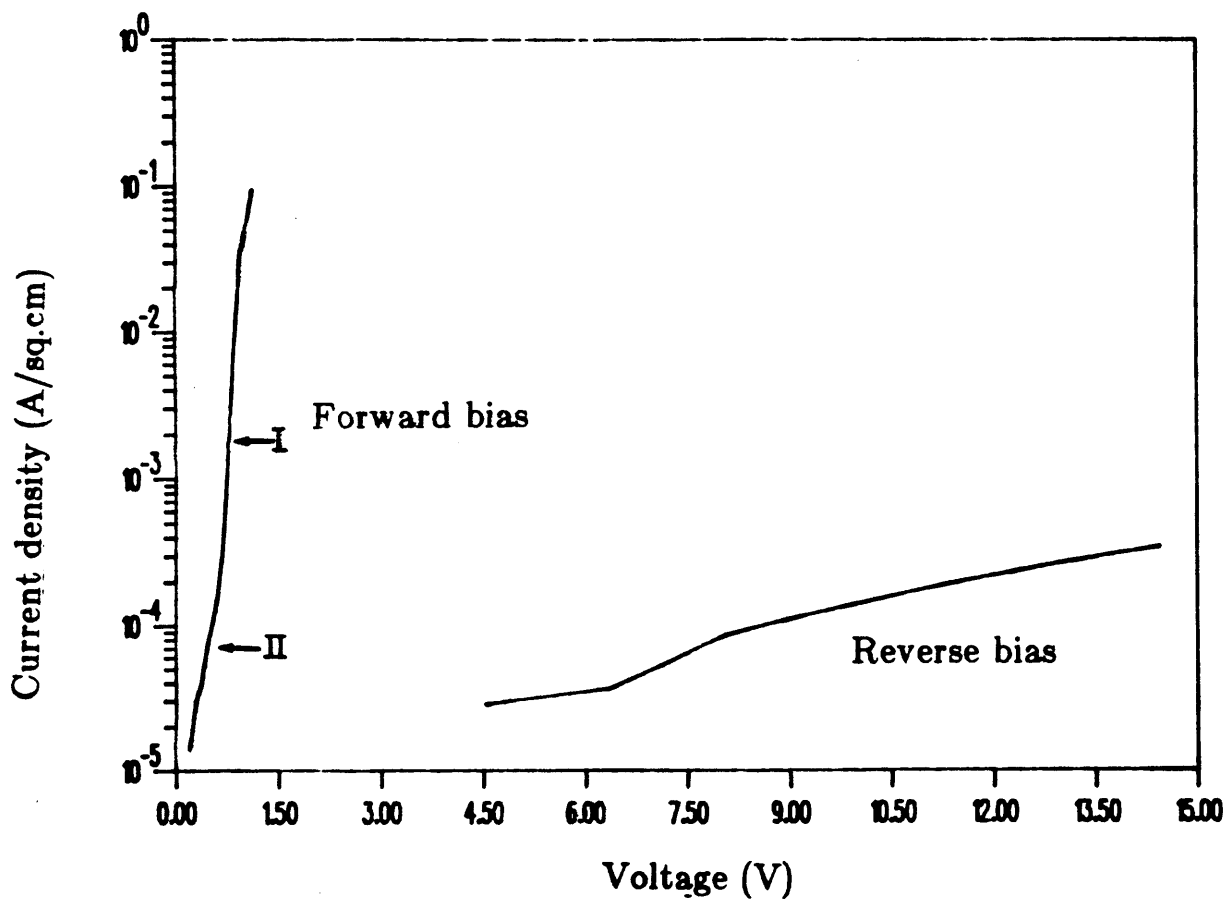


Figure 40. I-V characteristics of the p-n diode.

4.6 OBSERVATION OF PSEUDO-FIVE FOLD SYMMETRY IN GaP

4.6.1 INTRODUCTION

In the above discussion, there was a mention on the growth aspect of GaP thermally deposited at 600°C. This is presented in detail below. Transmission electron microscope diffraction patterns exhibiting five-fold-like symmetry were observed while examining GaP films grown by laser-assisted chemical vapor deposition. The five-fold-like pattern was a composite effect from multiple crystallites.

The existence of crystalline solids having five-fold rotational symmetry has been an issue of controversy since 1984 when transmission electron microscope (TEM) specimens of Al-Mn alloys were found to exhibit this phenomena (48). There are two schools of thought regarding the nature of observed five-fold symmetry. There are those who believe that certain materials exhibit icosahedral point group symmetry, i.e. five-fold coordination of atoms present in liquid phases is preserved in the solid state upon solidification (48,49). In contrast, others hold the belief that the apparent five-fold diffraction observed in Al-Mn crystals is a result of multiple twinning of cubic crystals (50,51). Investigators have also produced electron diffraction patterns that exhibit five-fold symmetry while studying alloys in the Al-Ti system (52). These researchers have demonstrated that the five-fold symmetry pattern resulted from the collective effects of multiple crystals of cubic symmetry, not from a crystal having an axis of five-fold symmetry. Here we report yet another instance in which diffraction from highly twinned polycrystals give rise to a five-fold like pattern.

When the Excimer laser-assisted epitaxial growths of GaP was conducted at

the upper end of the temperature range (i.e. 600°C, the deposition did not remain planar, and ellipsoidal 'cones' grew out of the surface. Cones, or hillocks, have been reported elsewhere for GaAs and InGaAs (53). The cones, which were 5 to 10 micrometers high, terminated in polycrystalline crests. It was during the examination of the crests that the apparent five-fold symmetry was observed.

4.6.2 DISCUSSION

A scanning electron micrograph illustrating the cones and crests described above is shown in Fig.41. Cross-sectional transmission electron microscopy samples were prepared from the specimen to allow examination of the deposited layer. Fig.42 presents a bright field TEM image of one of the cones which shows highly twinned, polycrystalline morphology. A selected area diffraction (SAD) pattern of the lower portion of the cone is shown in Fig.43 where the zone axis is along [110]. It is the SAD pattern of the polycrystalline crest shown in Fig.44a that suggests a five-fold-like rotational symmetry.

Microdiffraction studies of the individual crystallites gave no evidence of the diffraction pattern shown in Fig.44a. The absence of five-fold symmetry in the microdiffraction patterns leads to the conclusion that the five-fold pattern illustrated in Fig.44a is not inherent to the crystalline lattice, but a consequence of the twinned polycrystalline morphology of the deposited material. A diffraction pattern from a highly twinned single crystal GaP along [110] is shown in Fig.35b. It is believed that this is the basic pattern that lead to the appearance of the five-fold-like diffraction effect. To demonstrate this effect, a simple [110] unit cell is repeated five times (Fig.44b) in order to create a five-fold-like symmetry. For simplicity, the extra reflections which arise from {111} twinning and double

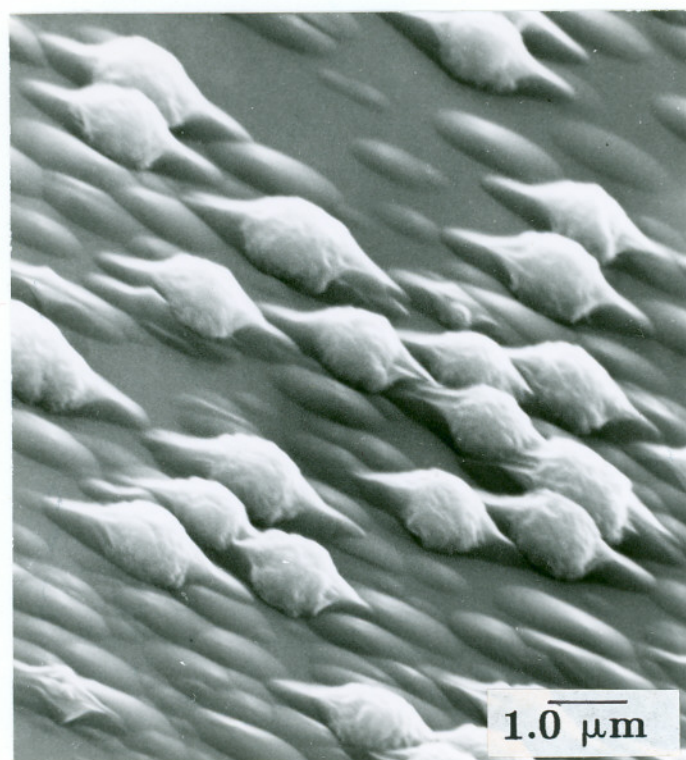


Figure 41. SEM micrograph showing the elongated pyramid-like structures with polycrystalline crest.



Figure 42. Cross-sectional TEM micrograph of a cone. The top portion is polycrystalline and the bottom is single crystal.

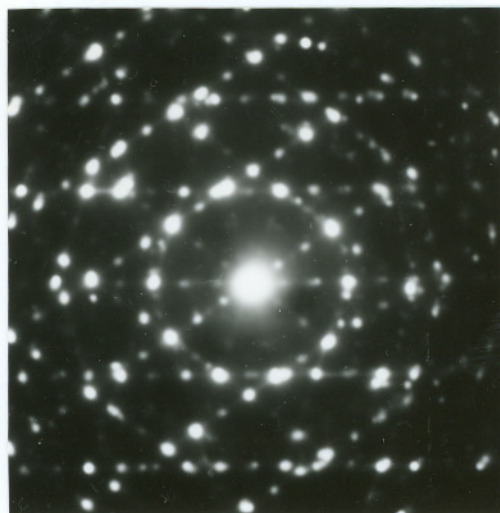


Figure 44. (a) Selected area diffraction pattern of the polycrystalline portion of the cone.

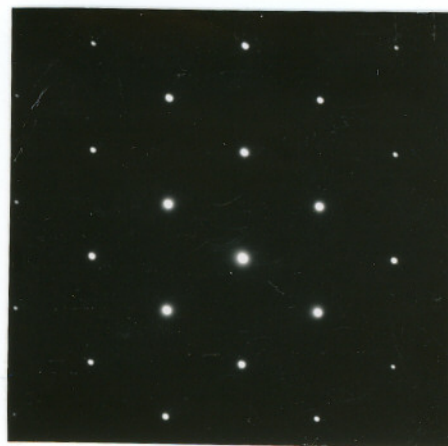


Figure 43. Selected area diffraction of the lower portion of the cone. Zone axis is $[100]$.

diffraction are omitted. The pattern displays ten-fold symmetry; the shortest reciprocal vectors are to ten 110-type reflections superimposed in pairs. Next furthest out come ten single 200 reflections with no superimposing effect and further on. It is believed that the above pattern (Fig.43b) was observed in Fig.44a during the examination of a twinned polycrystalline morphology of GaP.

The material systems previously found to exhibit pseudo five-fold symmetry were metallic, and formed either by solidification or physical vapor deposition. In the present case, the symmetry pattern was observed in a compound semiconductor formed by chemical vapor deposition. The appearance of pseudo five-fold symmetry in such disparate systems leads us to wonder if perhaps this phenomenon is commonplace.

REPEATED UNIT

94

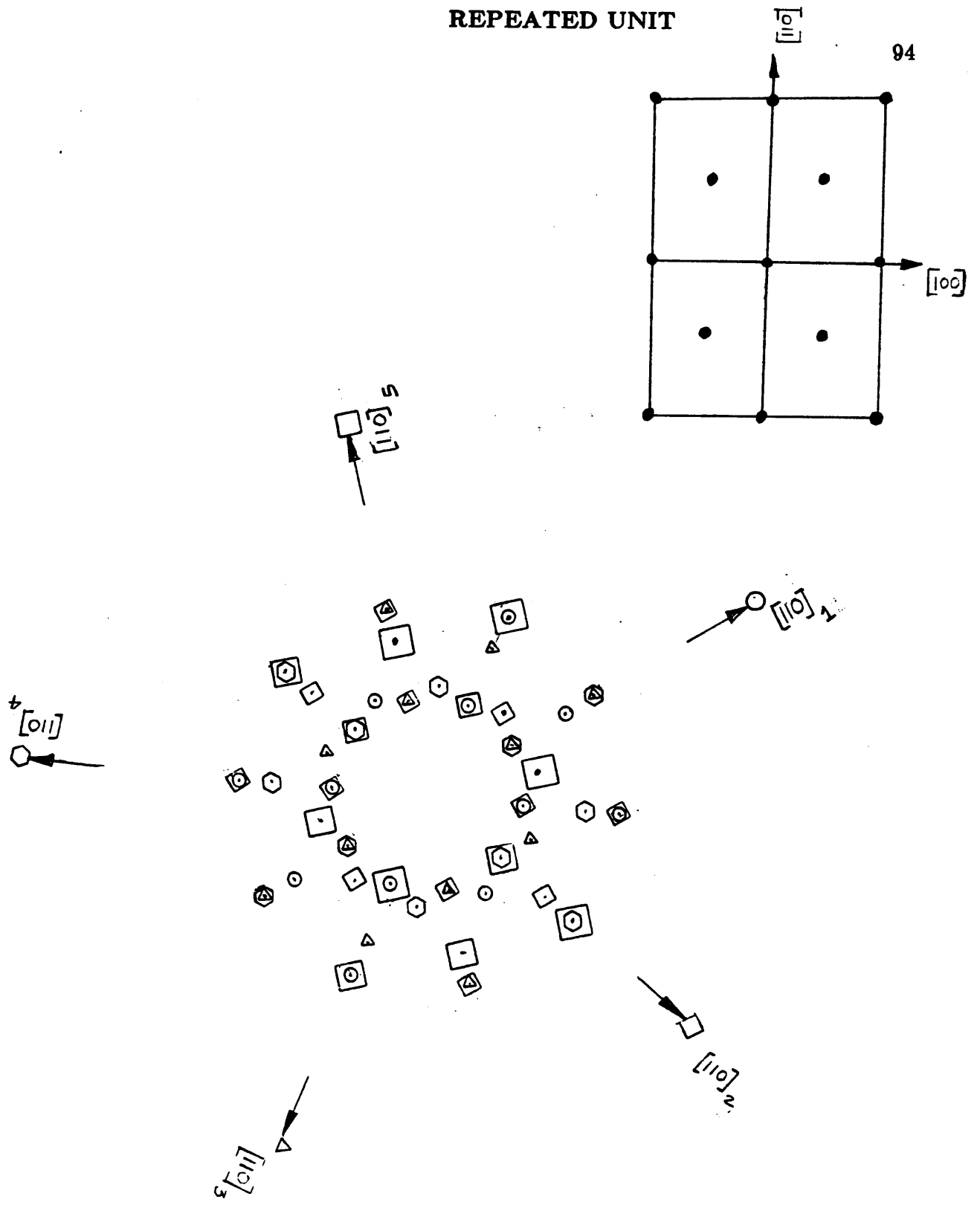


Figure 44b. Schematic of the diffraction pattern corresponding to Figure 44a.

4.7 HETEROEPITAXIAL GROWTH OF GaP ON GaAs

In order to demonstrate the low temperature nature of the process, heteroepitaxy of GaP on GaAs was attempted. The reported growth temperature for GaP in a conventional OMVPE system is about 900°C, while at this temperature GaAs decomposes because of the high equilibrium vapor pressure of arsenic. However, if GaP could be grown epitaxially on GaAs at 500°C, then the usefulness of the process will be demonstrated since at this temperature GaAs is less likely to dissociate. Growth conditions used for GaP on GaAs was same as for homoepitaxial GaP. Cross-sectional TEM was used to characterize the deposits.

Heteroepitaxial growth GaP was indeed achieved on misoriented (100) GaAs substrate. However, the growth of GaP was found to be periodic in nature, with a periodicity about the wavelength of the laser. Again both plan-view and cross sectional TEM were used to characterize the epitaxial structures. The following discussion is based on the cross-section TEM results obtained during examination of the epitaxial growth in a direction parallel to the periodic structure (referring to Fig.45, it is cross-section along AA). Results of plan-view and cross-sectional TEM in a direction normal to the periodic structure are discussed in chapter 4.9.

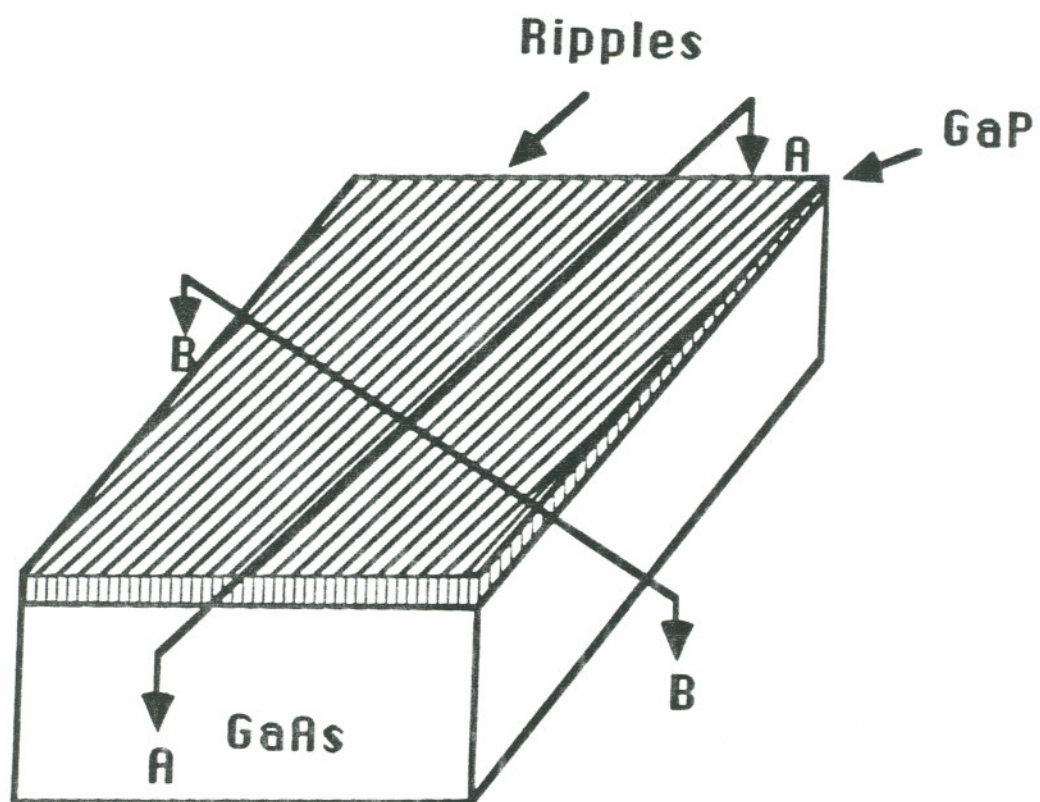


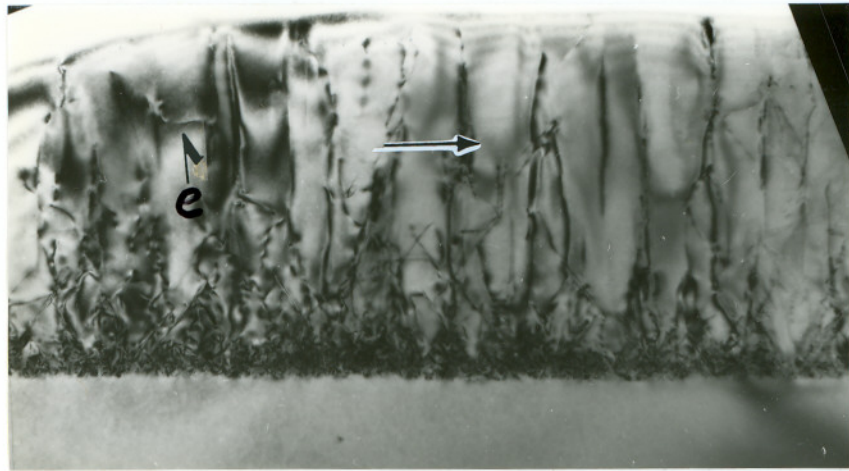
Figure 45. Schematic of TEM cross-section sample orientation.

4.8 COMPARISON OF HOMO- and HETEROEPITAXIAL DEFECT STRUCTURES

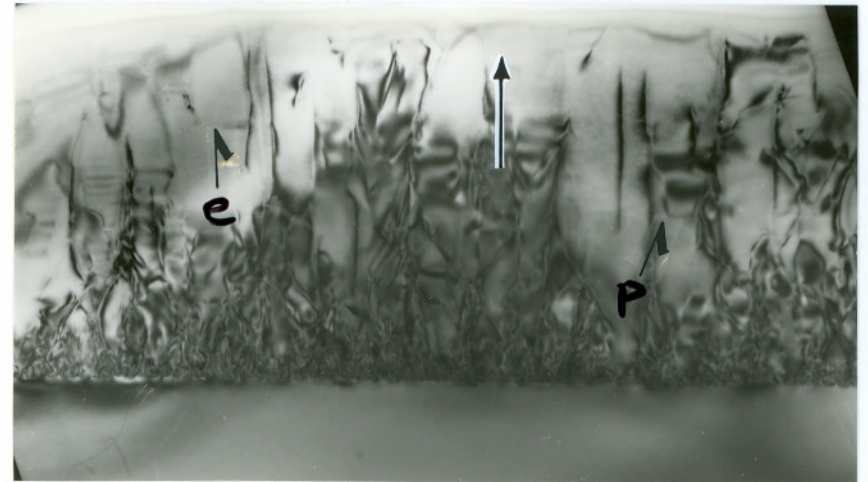
During cross-sectional transmission electron microscopic analysis of GaP/GaP and GaP/GaAs, it was observed that the homoepitaxial defect structure was different from that in heteroepitaxy. The nature of the defects and also the possible reasons for the origin of these defects are discussed in this section.

4.8.1 DEFECT STRUCTURE IN GaP/GaP:

The defect structure of the homoepitaxial GaP is shown in Figs.46a-d. The XTEM sample was viewed using four different 2-beam conditions, $[0\bar{2}2]$, $[400]$, $[\bar{2}2\bar{2}]$ and $[\bar{2}2\bar{2}]$ to analyze the defect structures. The $\bar{g}\cdot b$ criterion was used for visibility of dislocations, where \bar{g} is the diffraction vector and b the Burgers vector of dislocations (54). There was a high defect density region close to the interface which extended up to $0.08\mu\text{m}$ into the epilayer (Fig.46a). This region consisted of both line (dislocations) and planar (twins, stacking faults) defects. Above the highly defective interface region, the most dominant defect structure in the epilayer was stacking faults. The partial dislocations enclosing the stacking faults which disappeared under $[0\bar{2}2]$ beam condition had $1/6 \langle 211 \rangle$ - type Burgers vector and are indicated by 'p' in Fig.46. Pure edge dislocations of the type $\pm 1/2[0\bar{1}1]$ type, indicated by 'e' were also observed in the epilayer. These became invisible in $[400]$ direction suggesting that the Burgers vectors are lying in the growth direction perpendicular to the $[0\bar{1}1]$ direction. The threading dislocations penetrated the epitaxial film and are indicated as 't' in Fig.46d.

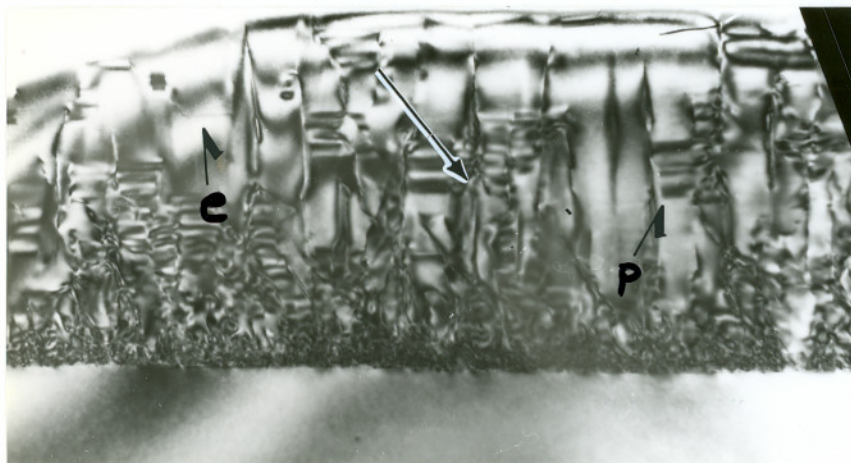


(a)

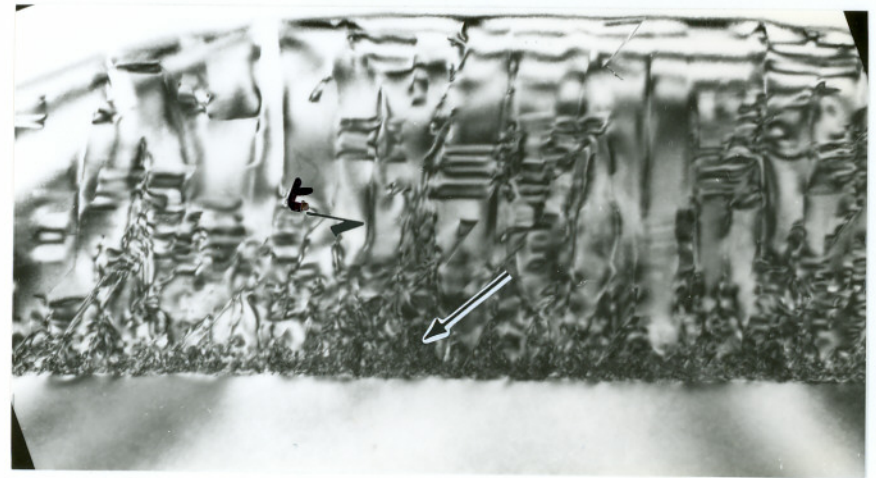


(b)

0.2 μm



(c)



(d)

Figure 46. (a-d) Cross-sectional TEM micrographs showing the defect structure in homoepitaxial GaP under four different reflections: (a) 022, (b) 400, (c) 222, and (d) 222.

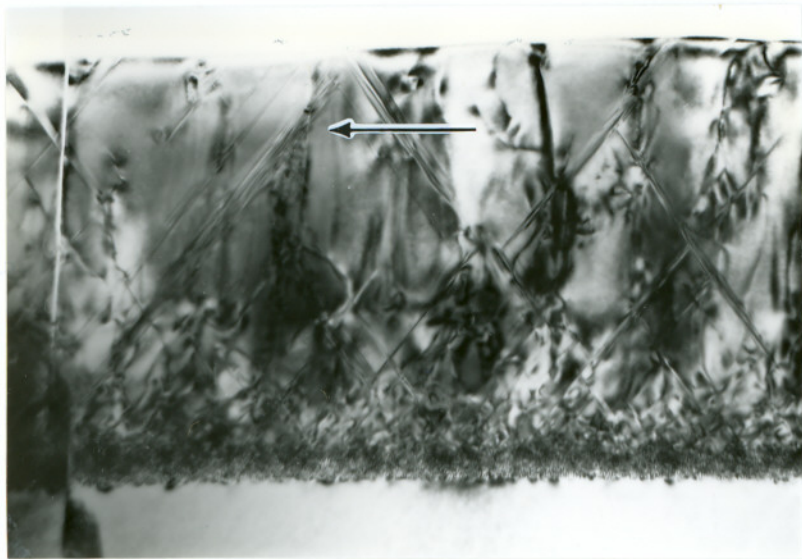
In the figures, 'p' indicates partial dislocation, 'e', pure dislocation and 't', threading dislocation.

4.8.2 DEFECT STRUCTURE IN GaP/GaAs:

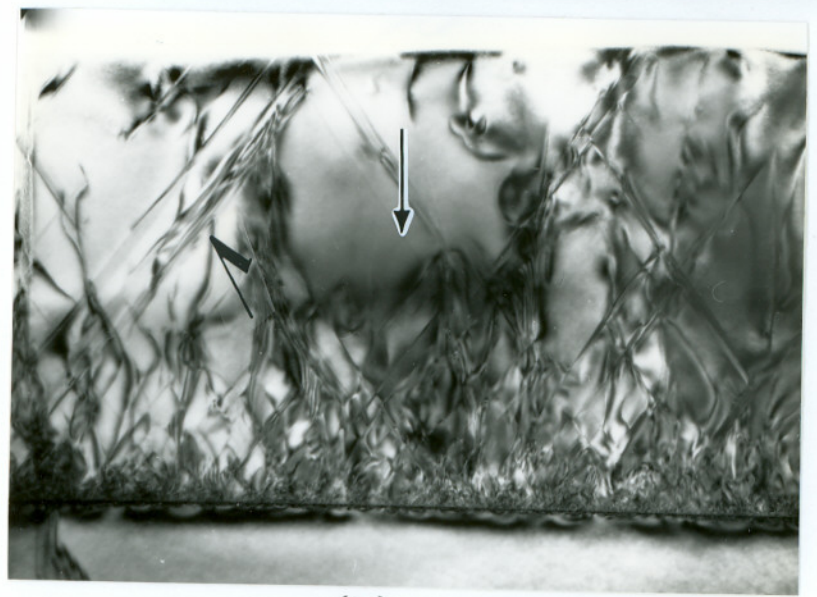
The defect structures observed in the heteroepitaxial GaP on GaAs are shown in Figs.47a-d. These micrographs were taken at four different 2-beam conditions i.e. $[02\bar{2}]$, $[\bar{4}00]$, $[22\bar{2}]$ and $[2\bar{2}2]$. It should be noted that both the homo- and hetero-epitaxial layers were grown under identical experimental conditions.

One major difference observed in the defect structures of the homo- and hetero-epitaxial layers is the presence of twins in the latter case which is indicated by arrows in Figs.47a-d. Although twins were also observed in the homoepitaxial growth, they were not the dominant defect structures, whereas in the heteroepitaxial film they extended from the interface to the top of the epilayer. From Figs.47c and 47d, it is clear that twinning has occurred along the four $\{111\}$ planes. The sample was tilted to reveal only the twin structure (Fig.48) which showed that the defects originated from the interface and propagated through the film thickness.

There was also a conspicuous absence of the partial dislocations enclosing the stacking faults under $[22\bar{2}]$ and $[2\bar{2}2]$ beam conditions (Figs.47c & d). In order to further examine the interface, the XTEM sample was tilted which revealed the presence of triangular structures that could be the pyramid-shaped dislocation tangles (PDT) (55,56). Dislocations originated from the apex of these triangular structures (Fig.49). Presence of these defects have been attributed to composition inhomogenities at the interface and 3-D island formation during nucleation stage of the film growth process (56). In contrast, tilting of the homoepitaxial GaP film failed to reveal any defect similar to the PDTs.



(a)



(b)

$0.2 \mu\text{m}$



(c)



(d)

Figure 47. Cross-sectional TEM micrographs showing the defect structure in GaP grown on GaAs, under four different reflections: (a) 022, (b) 400, (c) 222, and (d) 222. The arrows indicate twins.

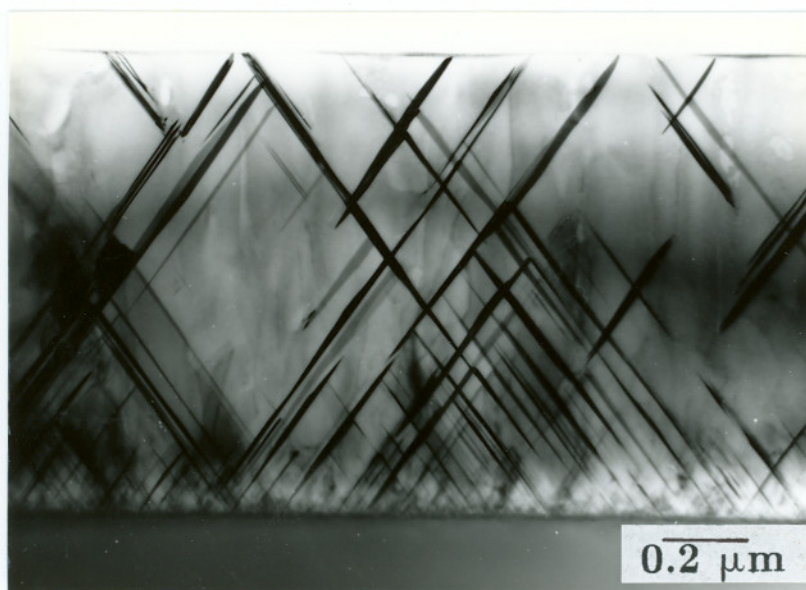


Figure 48. Heteroepitaxial GaP sample tilted to reveal twins.



Figure 49. Cross-sectional TEM micrograph of GaP/GaAs tilted to reveal the interface.

4.8.3 DISCUSSION

When a semiconductor surface is irradiated with a laser, there is a rise in temperature. In a pulsed laser irradiation, the surface is hot for a duration determined not by the temperature rise (approximately the laser pulse width itself), but rather by the temperature fall time. This fall time is in turn determined by heat diffusion into the bulk after the pulse. The dependence of temperature distribution on depth z , and time, t , assuming the pulse to be centered at $t=0$, is characterized approximately by (half) Gaussian

$$T(z,t) = T_{\text{Sub.}} + \Delta T(z=0,t) \exp \left[- \left(\frac{z}{l_0 + \sqrt{4D_T t}} \right)^2 \right] \quad (4.20)$$

with the time-dependent skin temperature change

$$\Delta T(z=0,t) = I(1-R) / (\rho C_p (l_0 + \sqrt{4D_T t})) \quad (4.21)$$

where I is the incident laser fluence (in J/sq.cm), and D_T is the thermal diffusion coefficient of the substrate, l_0 is the thermal diffusion length, C_p is the heat capacity, ρ is the density, and R is the reflectivity (21). The above equation is the analytical solution to a one dimensional heat conduction problem that assumes temperature independent thermal conductivity and specific heat properties. A laser pulse incident on a surface will induce a temperature rise which will reach a peak and then drop. The maximum temperature will therefore be achieved with approximately half the laser pulse. A plot of temperature as a function of depth and time after half the pulse on GaP is shown in Fig.50. A similar plot for GaAs showed an almost identical profile except for the maximum temperature and the duration. The maximum temperature rise from a laser pulse

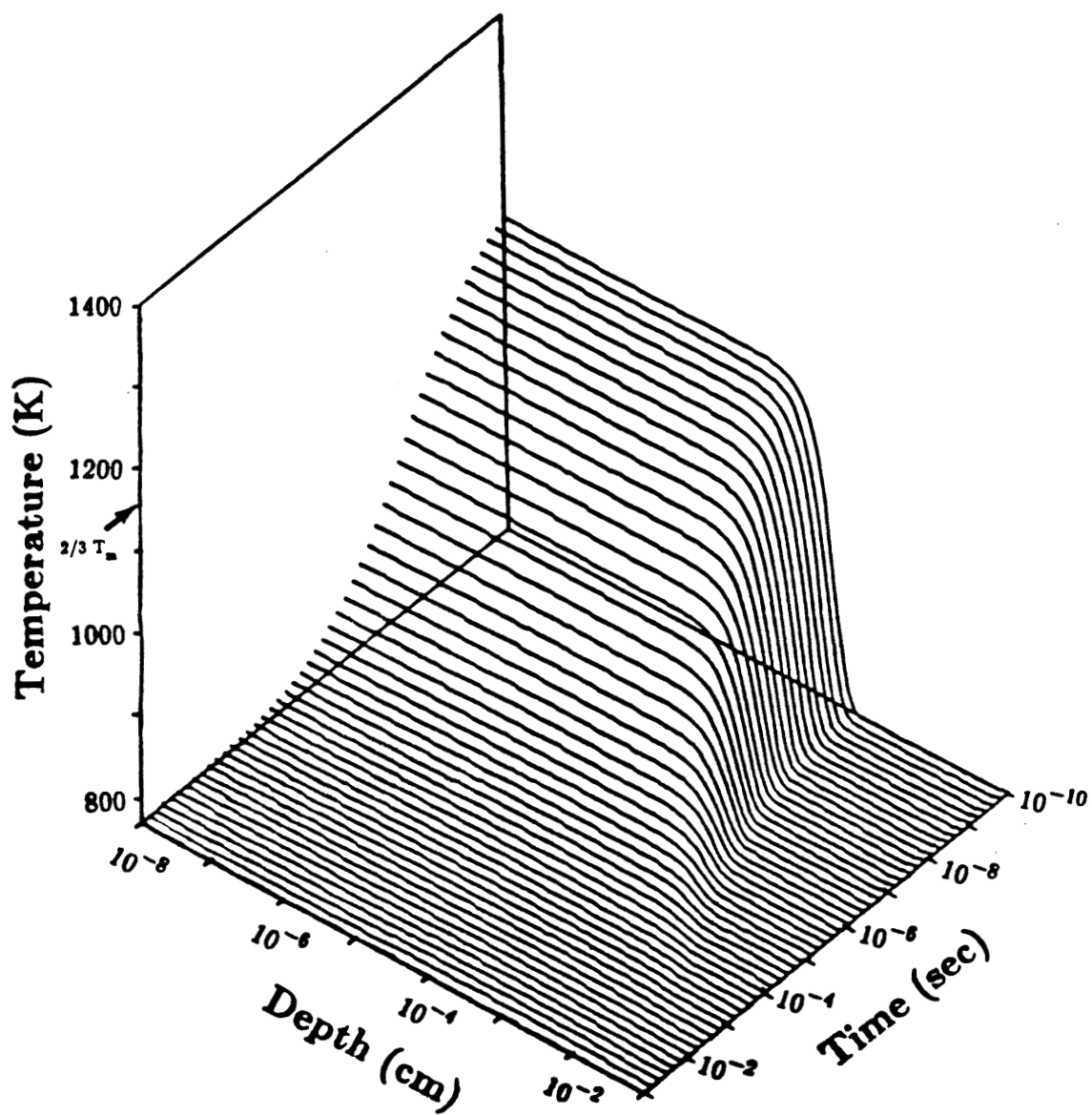


Figure 50. Plot of temperature rise for a single laser pulse on a GaP substrate at 500°C .

of 0.11 J/cm^2 in GaP was about 1150K and in GaAs about 1230K. The model also predicts that significant temperature rise occurs in GaP to a depth of under $0.1 \text{ }\mu\text{m}$, whereas in GaAs, this value is slightly over $0.1 \text{ }\mu\text{m}$. It should be noted that all the laser energy incident into the deposition reactor was assumed to reach the substrate surface, hence neglecting any absorption by the precursor gases. Moreover, any cooling effect of the gases in the reactor was also neglected. Both these factors (further discussed in section 4.9) will lower the maximum temperature predicted by this model.

For compound semiconductors, the ductile-to-brittle transition occurs around $2/3$ of T_m , where T_m is the melting point in degree kelvin (57). A temperature rise of 1200°K on the surface is more than the transition temperature of both GaP and GaAs, hence some plastic deformation is likely to occur. The amount of deformation depends on the duration of the high temperature. Growth of GaP per pulse is about 0.12\AA , and hence the effects due to plastic deformation extends through the grown layer as predicted by the above model. Plastic deformation is a phenomena that results in generation and movement of line and planar defects in materials. The movement of the line defects (i.e., dislocations) is controlled by the temperature and stress level. It is empirically known that the velocity v of a dislocation of any type in a semiconductor is, in general, well described by the expression which is a function of stress τ and temperature T :

$$v = v_0 \tau^m \exp(-Q/kT) \quad (4.22)$$

where v_0 , m are constants, Q is the activation energy and k is the Boltzman constant (58). For GaP and GaAs,

$$v_{\text{GaP}} = v_0 \tau_1 \exp(-2.2/kT) \quad (4.23)$$

$$v_{\text{GaAs}} = v_0 (\tau_2)^{1.7} \exp(-1.5/kT) \quad (4.24)$$

τ is the effective stress needed to move dislocations against intrinsic resistance of the crystal lattice (58). For GaP and GaAs, τ is approximately the same for temperatures around 1000K. Under such condition, the above two equations can be written as

$$v_{\text{GaAs}} = v_{\text{GaP}} \tau^{0.7} \exp(0.7/kT) \quad (4.25)$$

It is evident from eq.4.25 that for the temperature range considered, dislocation velocity is much greater in GaAs than in GaP. In other words, for a particular rise in substrate temperature, GaP deforms less plastically than GaAs and this is expected to introduce different degrees of cyclic stress in thin films GaP/GaAs than in GaP/GaP. Also the deformation-induced stress in the epitaxial films is very likely to produce partial dislocations which are probably responsible for large densities of stacking faults and twins. If the dislocation velocities were known, the above model can be used to calculate the temperature and duration, hence estimate the distance propagated by dislocations.

During the heteroepitaxial growth of GaP, there are at least two sources of defects at the epi/substrate interface. First, there is a 4% lattice mismatch which gives rise to line and planar defects. Most defects are accommodated at the heterojunction interface. The second source of defects originate due to initial composition inhomogenieties during the nucleation stage. These could lead to atomic deposition errors resulting in a high density of planar defects (i.e. twins) at the interface. Thus a highly defective region consisting of microtwins and

dislocations is formed near the interface during the initial stages of heteroepitaxial growth. These microtwins are believed to be sustained and grown in response to the thermal mismatch induced stress and differential plastic deformation-induced stresses due to the pulsing laser within the crystal matrix. In comparison, propagation of microtwins was not observed in homoepitaxial GaP films.

4.8.4 SUMMARY

The crystalline defects in homo- and heteroepitaxy of GaP were examined using XTEM. The dominant defects in homoepitaxial growth are stacking faults compared to twins in heteroepitaxy. It is interesting to note that although laser-assisted epitaxy is believed to be a low temperature process, its thermal contribution appears to play an important role in inducing partial dislocations and propagation of planar defects.

4.9 FORMATION OF PERIODIC STRUCTURES DURING EXCIMER LASER-INDUCED HETEROEPITAXY

4.9.1 INTRODUCTION

It has been observed that as a result of exposure to laser radiation under certain conditions, periodic structures or ripples are formed on surfaces of metals (59-61), dielectrics (62), and semiconductors (63-67). The origin of these structures has been explained as interference between the incident laser light and scattered or stimulated wave at the surface (63,67-69). Other possible mechanisms proposed include generation of capillary waves (70) and standing surface acoustic waves (65). In all cases, the direction of the periodic pattern has been dependent on the polarization of the electric field of the incident beam.

During photochemical deposition, periodic structures have been reported almost exclusively on metallic films (25,71-73) where the most frequently used ultraviolet (UV) sources employed have been doubled (257nm) argon ion lasers. The origin of ripple structure in these films has been attributed to the interference of the incident UV field and the surface plasma wave (25). The intensity variation due to this interference modulates the film growth which in turn exponentially enhances the scattering of the incident field into surface-plasma wave. A modulated surface photon flux on the surface enhances adsorbed layer photodissociation of precursor gases leading to a modulated film growth. However, if gas phase dissociation is dominant, the film growth will tend to be uniform over the substrate. Thus in a photochemical reaction, the appearance of ripples was found to be a signature of the adsorbed layer dissociation of the precursor molecules (25).

In the investigation of excimer laser induced heteroepitaxy of GaP on GaAs, ripple pattern under certain growth conditions were examined. This is interesting, since inspite of minimally polarized output of our excimer laser, a well defined periodic structure was obtained on the GaP film. The crystalline properties and the composition of these structures were examined. These results are presented below.

4.9.2 DISCUSSION

The ripple pattern observed on the focused spot (2mm X 7mm) where $1\mu\text{m}$ thick GaP films were grown on (100) GaAs substrates is shown in Fig.51. The periodic pattern was uniform and in the same direction over most of this area. Towards the outer edge, the ripples had poor spatial coherence and frequently sub-divided. This feature is illustrated in Fig.52, which is a plan-view TEM micrograph. The spacing of the periodic structure was about 186nm, which is slightly less than the laser wavelength (193nm). However, this is reasonably consistent with the fringe spacing due to interference between incident and scattered wave given by $\lambda/(1+\sin\theta)$, where λ is the wavelength and θ is the angle measured from the normal to the surface (68). The direction of these ripples was found to be dependent only on the orientation of the laser beam. Also no change in the direction of the ripples was observed when GaAs substrates with (100), (111) or (211) orientations were used. The independence of the ripple direction with respect to the substrate crystalline orientation is not consistent with what McCrary et al (74) have observed using excimer laser assisted organometallic vapor phase epitaxy (OMVPE) of GaAs. They explained the origin of the periodic structure based on the presence of microcrystalline defects oriented along a particular lattice direction on starting GaAs substrate surface. At the outer

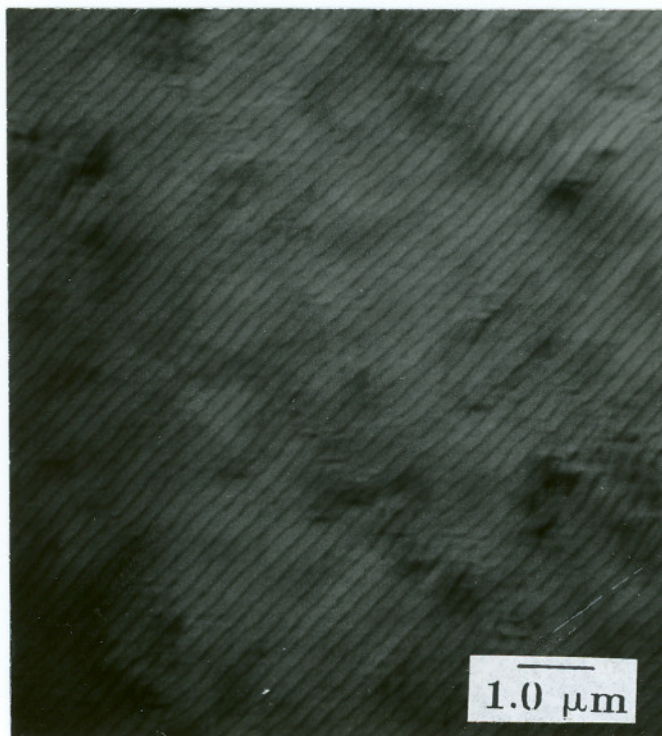


Figure 51. SEM micrograph of periodic ripple structures on epitaxial GaP grown on (100) GaAs.

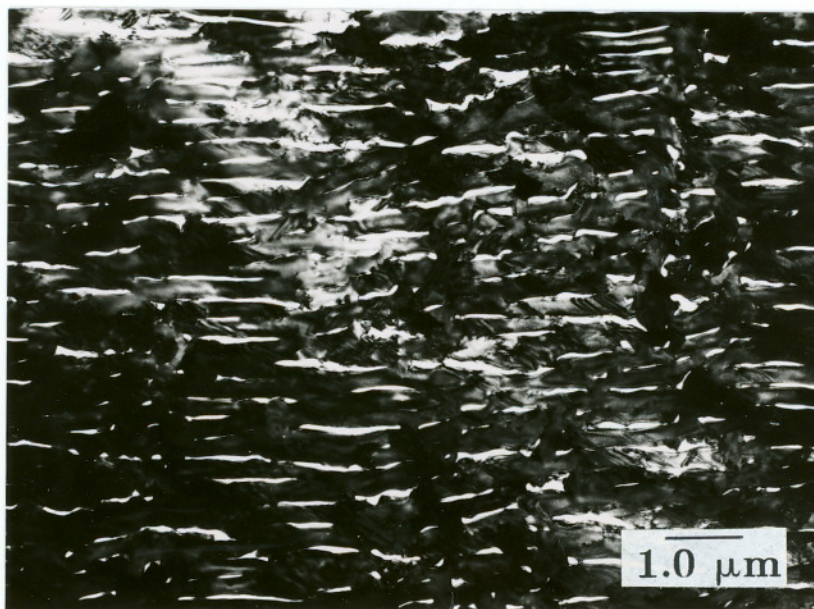


Figure 52. Plan-view TEM micrograph of GaP showing poor spatial coherence of the periodic structure.

most edge of the deposit, two sets of ripples, orthogonal to each other were seen (Fig.53). They had the same period as the standard ripples observed close to the center of the deposit.

Ripple formation was dependent on the laser energy density at a particular total pressure and the GaAs substrate temperature. At low energy density (0.07J/sq.cm), the growth was polycrystalline, hence no ripple pattern was observed probably due to the grainy (400 nm particles) nature of the film. At medium energy density (0.11 J/sq.cm), a periodic pattern was observed as shown in Fig. 51. At higher energy density (> 0.14 J/sq.cm) there was no film growth. In the case of homoepitaxial films (grown under identical conditions to heteroepitaxy) only a very faint presence of ripples was found over a narrow range of deposition parameters. The reason for this is discussed in the following sections.

The orientation of the linear periodic structures reported in the literature have been found to be perpendicular to the electric field of the laser beam. This has been found to be true in both melting-induced (68) and photolytically deposited films (25). Since the degree of polarization of excimer lasers is poor, the laser output from the excimer laser was examined in the following manner. The ArF laser beam was first passed through a pin hole and then through a single crystal calcite prism (perpendicular to z-axis) which was rotated. The image(s) of the pin hole was projected on a fluorescent screen. The pin-hole was scanned over the cross-sectional profile of the laser beam. It was found that the laser output was nominally unpolarized. The beam was estimated to be about 15% polarized, which was a result of an internal beam splitter that provided feedback for the laser power lock. This was interesting since all the periodic structure reported in literature have been related to a strong polarization effect of the laser

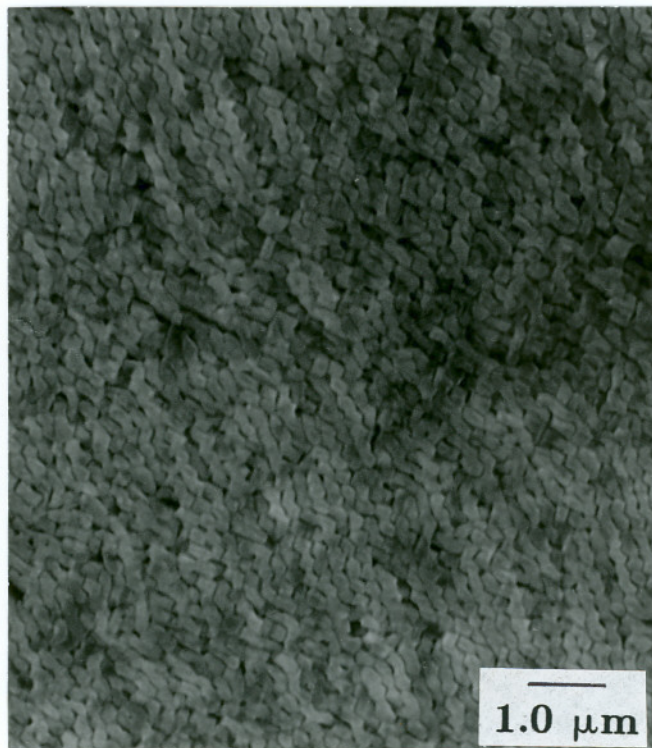


Figure 53. SEM micrograph showing the jagged ripple structure observed at the outer edge of the deposited.

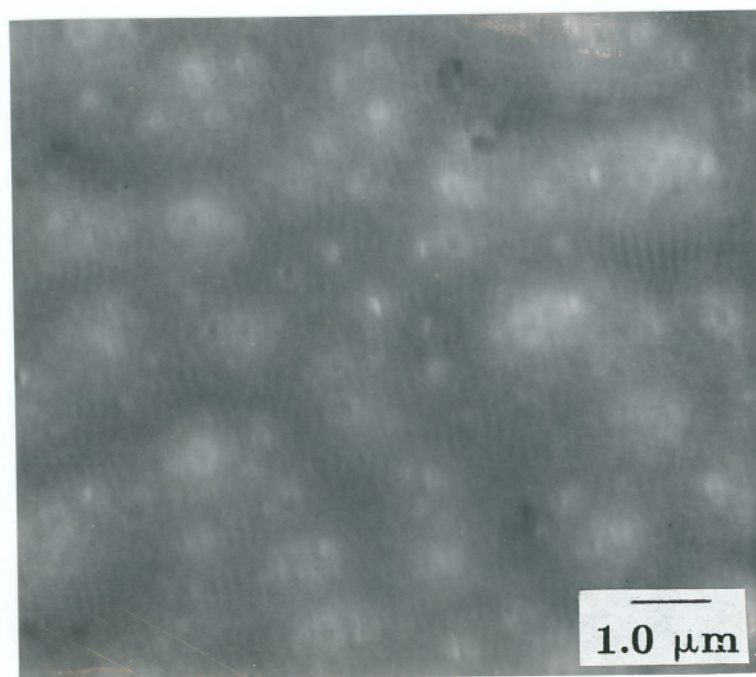


Figure 54. SEM micrograph of the faint periodic structure formed on bare GaAs.

output.

The incident photon energy of the laser (193nm) is larger than the band gaps of both the substrates that were used, hence this should result in a temperature rise and also in creation of electron-hole pairs. Thermal contribution from an ArF excimer laser incident on GaP and GaAs substrates is examined first.

The analytical solution (eqn 4.20) to a one dimensional heat conduction problem that assumes temperature independent thermal conductivity and specific heat properties was used for temperature calculations (21). A plot of temperature as a function of depth and power density after half the pulse on GaAs is shown in Fig.54. A similar plot for GaP showed an almost identical profile except for the maximum temperature. The maximum temperature rise from a laser pulse of 0.11 J/cm^2 (typical energy density used during growth) in GaP was about 1150K and in GaAs about 1230K. The model also predicts that a significant temperature rise occurs in GaP to a depth of under $0.1 \mu\text{m}$, whereas in GaAs, this value is slightly over $0.1 \mu\text{m}$.

The second consequence of the UV laser incident on the substrate surface is creation of electron-hole pairs. In the present case, it is assumed that a dense plasma is created for very short duration and a depth of about 100Å, which makes the substrate behave optically like a metal (69). This leads to surface polariton waves (SPW) propagating along the interfaces. Therefore, there are two possible sources for the formation of periodic structures. The first is the high substrate temperature for melting and regrowth and the second is the interference between the incident laser and SPW. Both these cases are considered below.

In order to determine the thermal contribution in the present case, both GaAs and GaP substrates were irradiated with 193nm laser light (0.11 J/cm^2) at

a substrate temperature of 500°C and only H_2 in the reactor. The total pressure in the reactor was the same as during deposition. After exposure to the laser, these samples were examined with a scanning electron microscope (SEM). The GaP substrate did not show any significant change, whereas the GaAs substrate showed faint periodic structures with spacings between 140nm to 190nm (Fig.55). The presence of ripples was surprising since the laser output, as discussed above, was nominally unpolarized. The direction of the periodic structures obtained without the precursor gases was the same as those on the deposited films. Under the operating condition ($0.11J/cm^2$), maximum temperatures predicted for GaP and GaAs are about $0.66 T_m$ and $0.81 T_m$ respectively, where T_m is the melting point in K. Since the temperature rise on GaAs is closer to its melting point than that on GaP, it is expected that localized fluctuations in the thermal profile could lead to temperatures close to the melting threshold in the former substrate. Interference between a surface and normally incident wave results in a standing wave pattern at the surface with the same wavelength. This mechanism most likely produced the periodic structures on the GaAs substrate.

During the photochemical-assisted film growth, gas phase dissociation plays an important role. This mechanism is expected to be quite significant in the process, since TMG absorbs strongly in the gas phase at 193nm (36). Though the absorption cross-section of TBP is not available, from mass-spectroscopic studies, the presence of atomic phosphorous during laser irradiation was determined. Thus, contribution to growth from gas phase dissociation is likely to be present during the growth runs. Therefore, one possible mechanism for formation of ripples on the epitaxial films in the present case is as follows. The interaction of the laser radiation with the GaAs substrate leads to faint ripple formation on its sur-

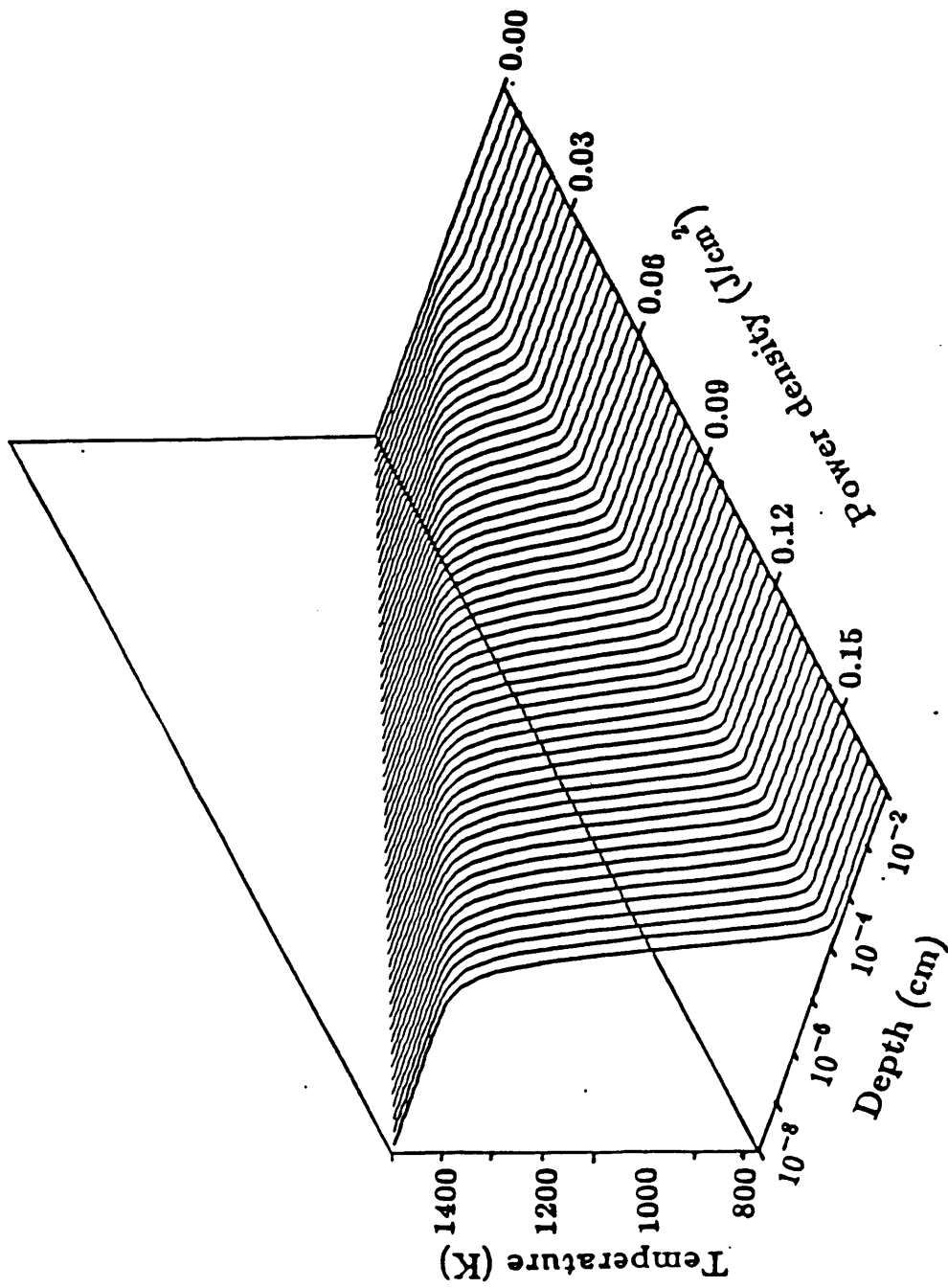


Figure 55. Plot of calculated laser-induced temperature rise in GaAs and corresponding depth vs. the laser pulse energy density.

face during the nucleation stage of GaP. When the growth occurs, the grating-like behavior of the modified surface will promote interference between incident and scattered laser radiation. This intensity profile will influence gas phase dissociation near the substrate and surface reactions, namely decomposition (both photolytic and thermal) and the mobility of the adsorbed species. With modulated initial growth of GaP, a positive feedback results that leads to a strong periodic structure. Therefore, thermal contribution from the excimer laser apparently plays an important role in the formation of ripples. This is consistent with the observation of the ripples during homoepitaxial growth of GaAs with a XeCl laser where the origin of periodic structures has been attributed to localized pyrolysis of adsorbed TMG and interference maximum of the light (37). It should be noted that in the present case, weak periodic structures were also obtained on homoepitaxial GaP. The orientation and spacing of the ripples was the same as heteroepitaxy. It is believed that this is due to a relatively higher melting point of GaP compared to the maximum temperature induced by the laser on its surface, and hence minimal initial substrate modification due to melting. The origin of the cross pattern observed at the perimeter of the laser spot (Fig. 53) cannot be explained at this time. Similar patterns have been observed during laser melting and have been attributed to surface tension (70). In the experiments, these structures were seen near the perimeter of the focused laser beam where the temperature rise was minimal (due to reduced laser intensity) compared to the center of the focussed spot. Therefore, it is less likely to be caused by melting and may be related to the nature of the electrical fields near the outer edge of the laser beam.

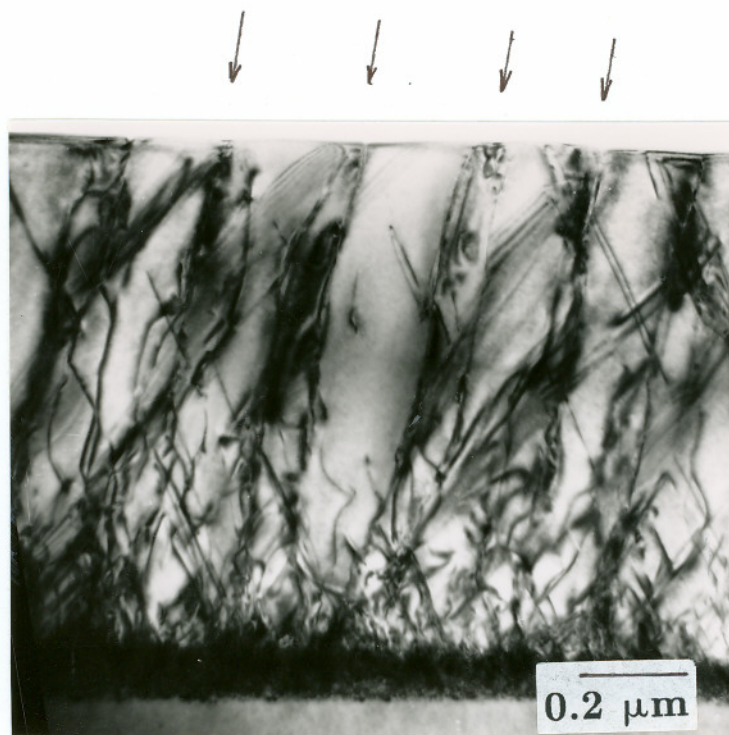
Another factor that has to take into consideration is the effect of 3-

dimensional nucleation during heteroepitaxial growth (56). During the nucleation phase the film will consist of fine particles before they coalesce into a continuous film. At this stage the 3-D nuclei can act as dipole scatterers. Interference resulting from the field setup by these structures and the incoming laser radiation can lead to the formation of ripples during the early stages of film growth which would provide positive feedback for subsequent growth.

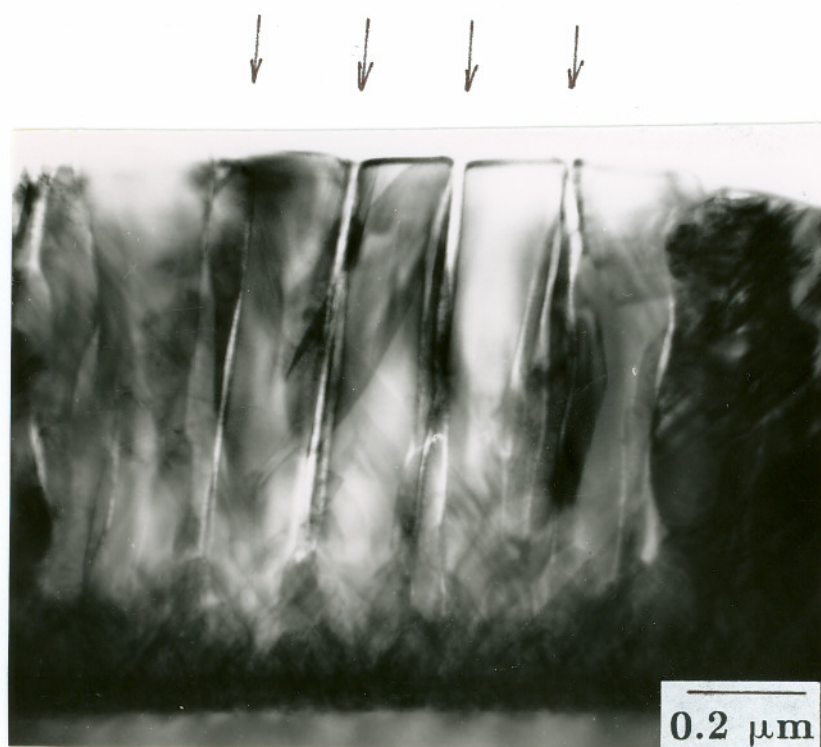
The mechanism that has been proposed to explain the ripple structure in metallic films deposited using UV photons is, as mentioned earlier, due to interference between the laser and SPW. However, this mechanism does not explain why only very weak periodic structures were observed on GaP substrates although the material properties of GaP and GaAs are similar at the operating wavelength of the laser.

4.9.3 CROSS-SECTIONAL TEM ANALYSIS OF RIPPLES

Cross-sectional TEM (XTEM) analysis of GaP/GaAs interfaces were carried out to determine if the ripple structures propagated through the film thickness from the interface or it was just a surface phenomena. Referring to Fig.45, the cross-section was along 'BB'. A typical XTEM of the heterointerface is shown in Fig.56a. The interface region consists of a high density of defects, many of which originate from the 4% lattice mismatch. In the cross-sectional profile, it can be seen that the ripples originate at the interface and propagated through the film thickness. The boundaries of the ripples are defined by the oblique dislocation structures. These dislocations originate at regions of optical interference minima. It is interesting to note that these dislocations are oblique with reference to the interface because the angle of incidence of the incoming laser beam was deli-



(a)



(b)

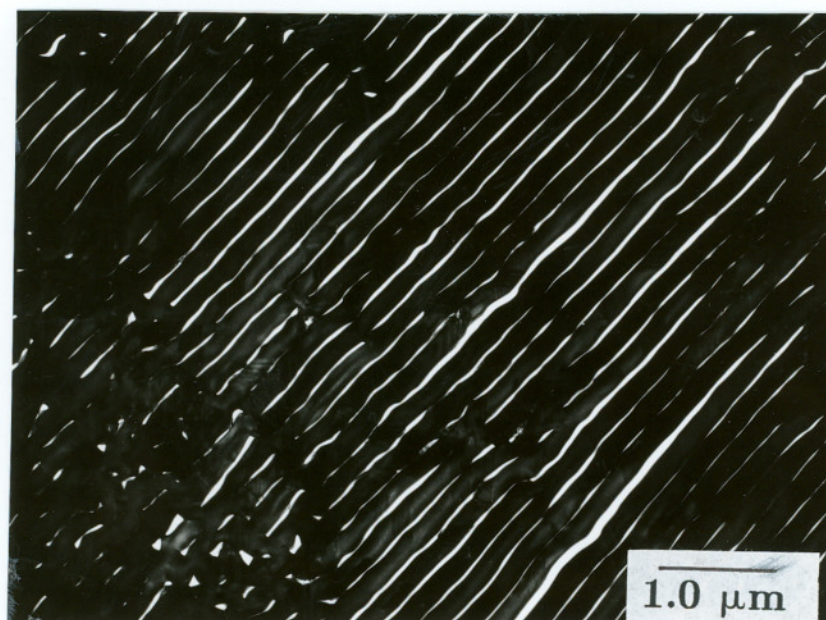
Figure 56. Cross-sectional TEM micrograph of the ripple structures showing (a) the dislocations as indicated by the arrows and (b) the voids formed at the ripple interface in the extreme cases.

berately tilted during growth. An extreme case of the inter-ripple defects is the presence of voids shown in Fig.56b.

4.9.3 PLAN-VIEW TEM ANALYSIS

Plan-view TEM of the periodic surface gave extensive information about the crystallinity of the ripple itself. A typical bright field image of the periodic structure is shown in Fig.57a. It can be seen that there are regions (upper right hand corner) where the ripples are not well defined. The origin of this perturbed region can not be accounted for at this time. The $[100]$ diffraction patterns from the rippled region and the perturbed region are shown in Figs.57b and 57c, respectively. The diffraction patterns from both the regions show identical crystalline orientation. However the pattern from the rippled region showed a strong streaking of the diffracted and transmitted spots along $[001]$, exactly at 90° to the direction of the ripples.

Bright-field and dark-field images of the ripples at higher magnification are shown in Figs.58a & 58b, respectively. The dark-field image was obtained by including just the streak from the transmitted spot as shown in Fig.57b. The region in between the ripples showed weak diffraction contrast. A close examination of these regions revealed the presence of a fine structure of spacing varying from 20A to 100A in a direction normal to the ripple. Since the inter-ripple regions were very thin compared to the rest of the area, in bright field, they transmitted more electrons, while in the dark field they showed poor diffraction contrast. When microdiffraction was attempted with a spot size of 100A, there was again spot streaking effect at about 50A from the interface (Fig.59). No other change in the diffraction pattern was observed. Because of the large spot



(a)

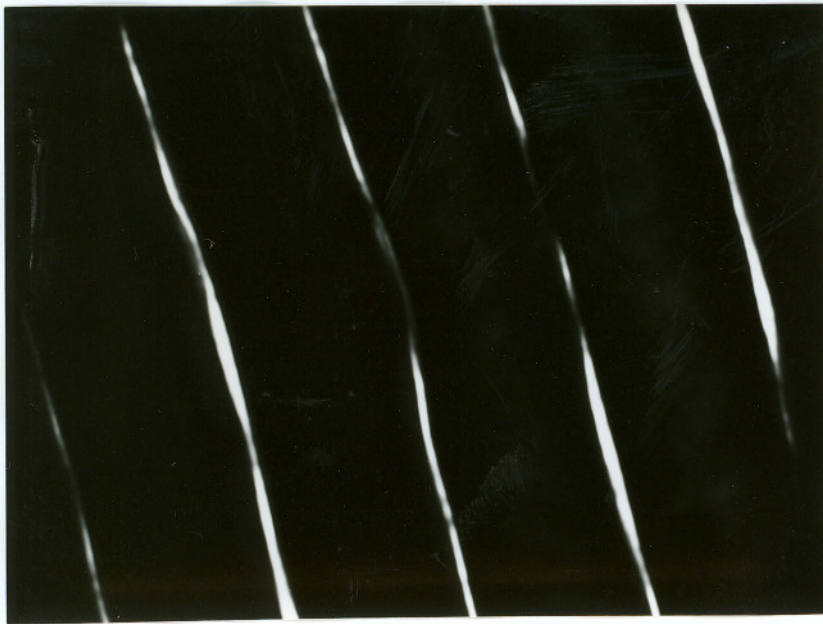


(b)

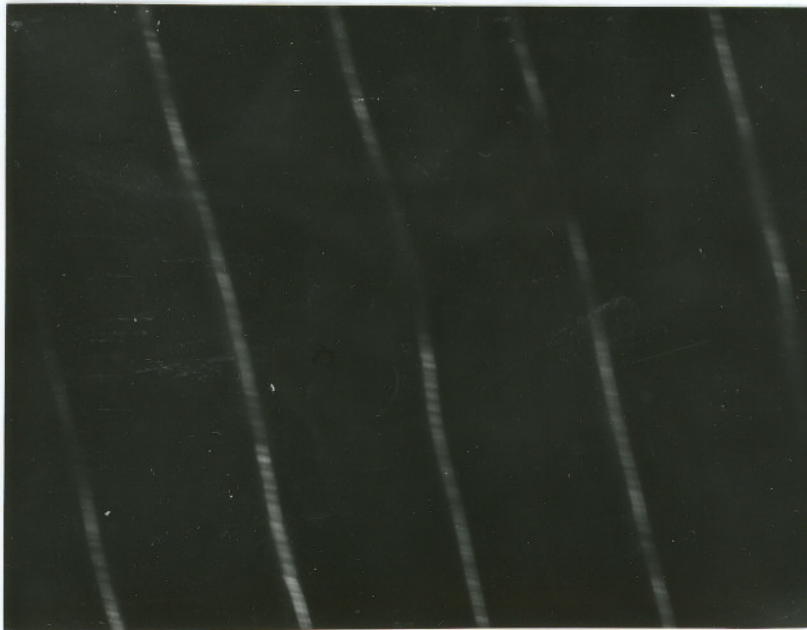


(c)

Figure 57. (a) Plan-view TEM of the ripples along $[100]$ zone axis and electron diffraction patterns from the (b) rippled and (c) perturbed regions.



(a)

 $0.05 \mu\text{m}$ 

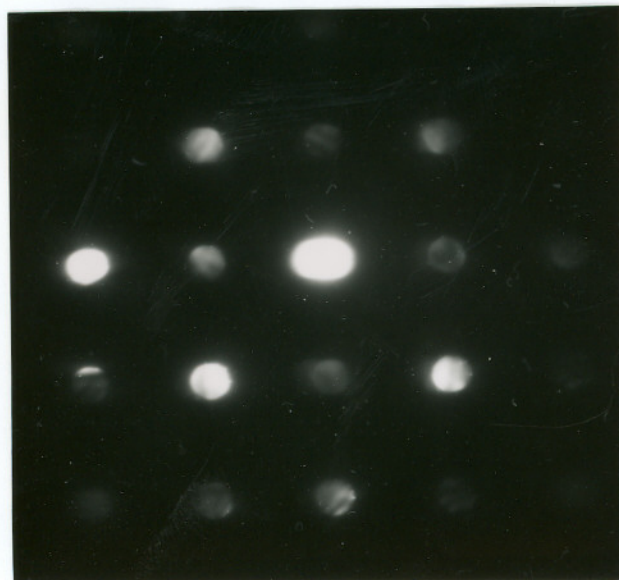
(b)

Figure 58. (a) Bright field and (b) dark field TEM image of the ripple obtained using a part of the transmitted spot streak.

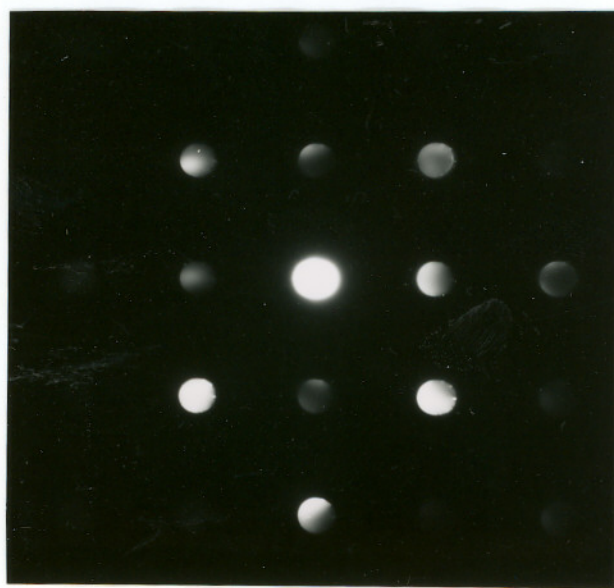
size, it was difficult to establish its precise location. The inter-ripple and region very close to the ripple contributed to the spot streaking. This probably meant that the spot streaking was due to some compositional variation of the GaP film near the ripples or at the inter-ripple region, that introduced a change in lattice parameter. A positive feedback in the coupling of the incoming photons with scattered wave from the ripples would lead to periodic heating of the surface, hence a change in composition. It is pertinent to note that the phase diagram of Ga-P system shows the presence of a single phase over a wide composition range.

Energy dispersive X-ray (EDX) microchemical analysis across the ripples was conducted with a 30A probe. Fig.60 is an example of the variation of gallium and phosphorous along the direction normal to the ripple. Little variation in the composition was observed along the direction parallel to the ripple. This is probably due to periodic temperature profiles which led to preferential vaporization of phosphorous to gallium along the hot zones created by the interference maxima, along the center of the ripple. These results, in addition to microdiffraction data suggest that the diffraction spot streaking is due to a variation in composition along the direction normal to the ripple. Fraunhofer diffraction of the electron beam due to the grating-like structure of the ripple pattern is not considered to be the reason for the spot streaking because of the very small wavelength of the electrons λ (0.027 Å) compared to the grating period (1890 Å).

Stacking faults were found to lie along $\langle 110 \rangle$ as shown in Fig.61. These defects are not likely to be responsible for streaking of the diffraction spots along [010] since they occurred along two {110} directions. In some regions the ripples were found to be attached by a dislocated interface.



(a)



(b)

Figure 59. Microdiffraction from (a) close to the edge of the ripple and (b) from the center of the ripple.

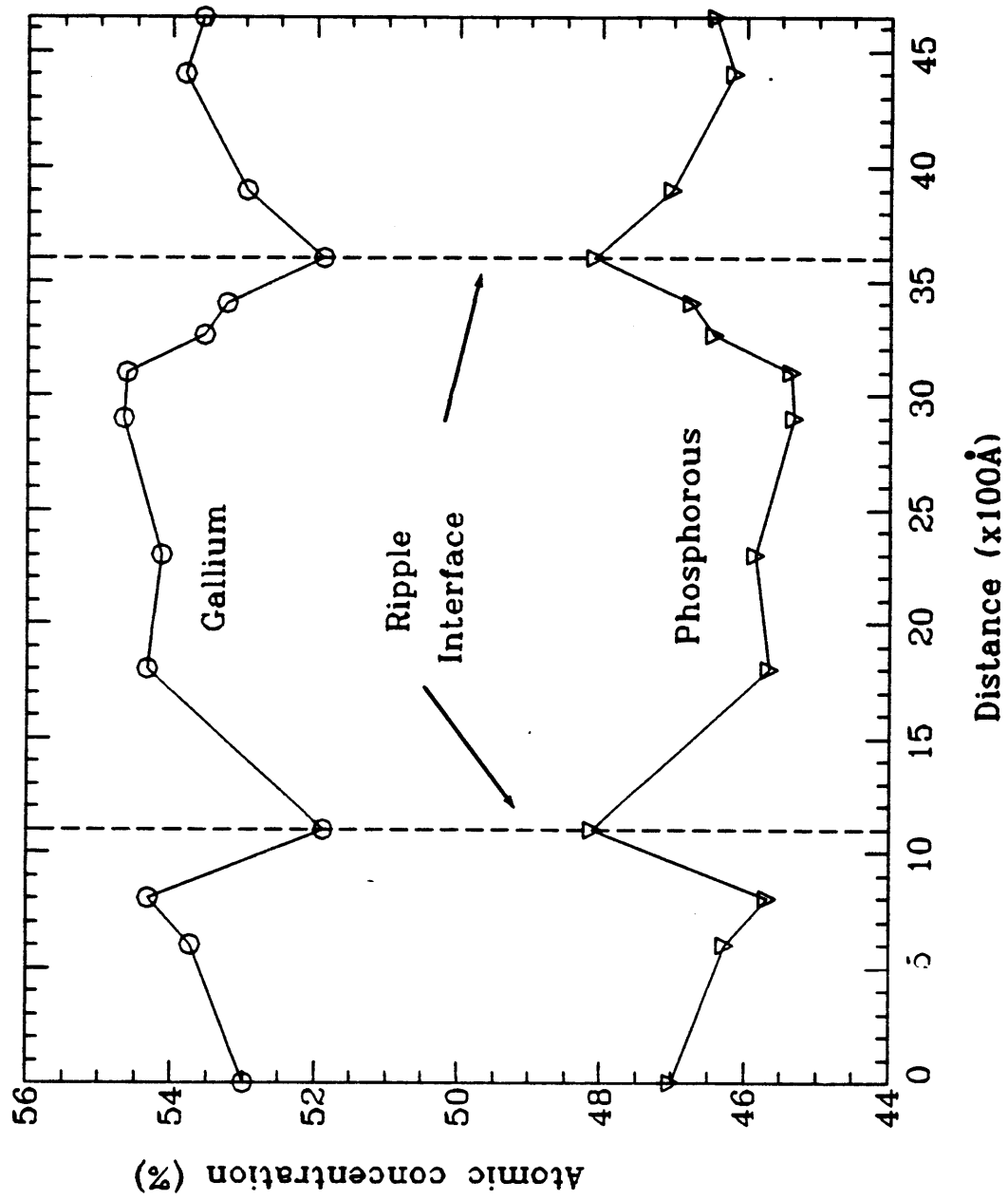


Figure 60. Plot of chemical composition across a ripple structure.

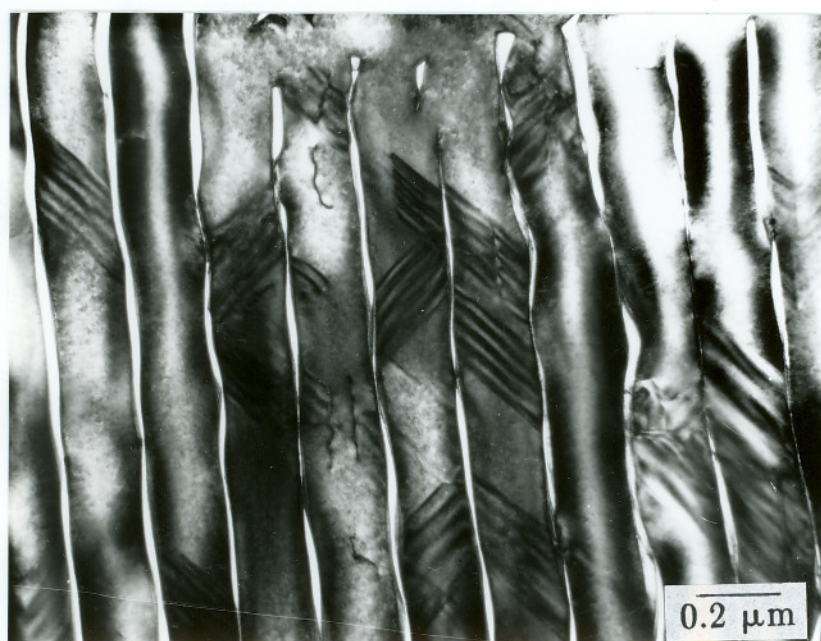


Figure 61. TEM micrograph showing planar defects across ripples.

4.9.4 SUMMARY

We have examined the ripple structure obtained during excimer (ArF) laser assisted OMVPE of GaP on GaAs and GaP substrates. The strong periodic structure observed on GaAs is believed to be due to the initial melting of the substrate during film growth. Microanalysis show variation in composition in the ripple structure resulting from the thermal variation caused by the optical interference during growth.

4.10 EXCIMER LASER-INDUCED HEATING: IN-SITU ELECTRICAL CONDUCTIVITY MEASUREMENTS

4.10.1 INTRODUCTION

In a pulsed ultra-violet laser induced chemical vapor deposition process, under normal laser incidence, part of the input photon flux is absorbed in the gas phase. The amount of energy absorbed depends on various operating parameters like the absorption coefficient of the reactant gases at the particular laser wavelength, concentration of the gases, reactor pressure and the optical path length. The flux that reaches the substrate induces electron-hole pair generation. As discussed in section 2.5.1, the UV radiation is absorbed by the electronic excitations and the energy is transferred to lattice resulting in a temperature rise. Yoffa proposed a laser-annealing model (75) in which the phonon emission rate was calculated to be $\approx 10^{-12}$ sec at carrier densities of $\approx 10^{19} \text{ cm}^{-3}$ realized in a 'standard' pulse of 10 nsec duration.

Since the heating occurs over a very short time as shown in section 4.7.3, it is not expected to influence the gas phase pyrolysis nature of the process. However, extreme heat input, though for a short time, can influence the adatom mobility and adsorbed layer pyrolysis, thus changing the growth rate and the crystallinity of the deposit. In addition to the momentary heating of the substrate, there is also an average temperature rise which depends on the laser power and repetition rate. In order to investigate the average heating effect due to a pulsed ArF excimer laser in a semiconductor (GaP), an experiment was designed to measure this by studying the electrical conductivity of the substrate under different operating conditions. These results are discussed below.

Electrical conductance measurements were performed on a n-type S-doped (100) GaP using a simple circuit as shown in Fig.62. Ohmic contacts were made to the n-GaP substrate by evaporating Au-12%Ge alloys and rapid thermal annealing at 450C for 60 sec. Lead wires were attached to the ohmic contact pads using heat setting silver epoxy. Electrical connections to the sample inside the cell was achieved using a vacuum electrical feedthrough. A constant bias voltage of 0.5V was used for most of the experiments. Voltages across the sample and the resistor were continuously monitored every 0.2 sec using an IBM compatible computer. The total collection time was varied depending on the experiment. Experiments were also carried out under zero bias conditions which will be discussed.

4.10.2 RESULTS AND DISCUSSION

4.10.2.1 MEASUREMENTS IN VACUUM

Initial experiments were carried out to measure the change in voltage drop across the load resistor for single laser pulses incident on the GaP substrate held in vacuum at room temperature. A plot of voltage across a constant load resistor as a function of time for three different pulse energies is shown in Fig.63. A sharp increase in voltage drop across the load indicates a drop in sample conductance. Also there was a non-linear increase in the peak height with laser energy. The decay time associated with the voltage change was in the order of tens of seconds. The initial conductance value of the sample was restored after about 20 minutes. If the increase in sample conductance were due to presence of photo-generated carriers, the decay would be much faster, of the order of nano- to microsecond. However, if the conductance change is due to heating of the sample,

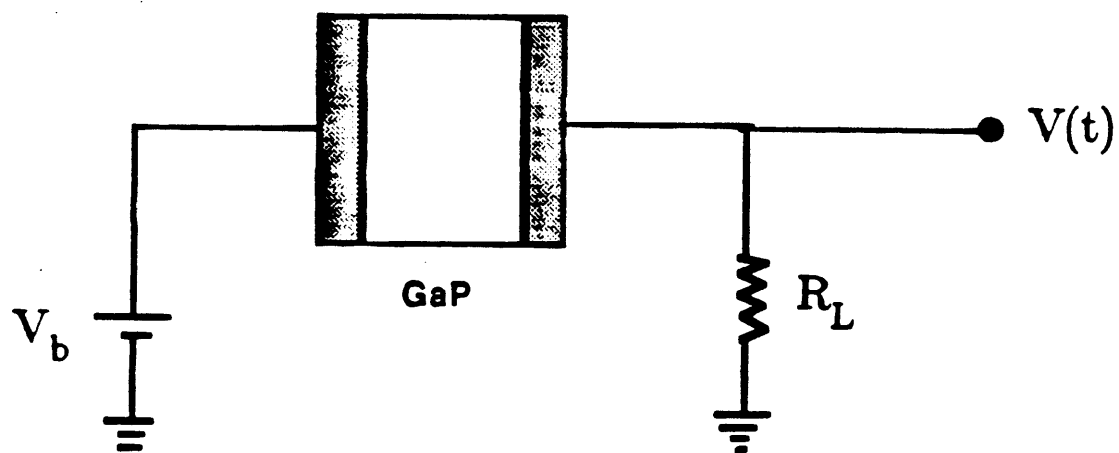


Figure 62. Schematic of the electrical conductance measurement set-up.

SINGLE PULSE AT 50, 90 & 140 mJ

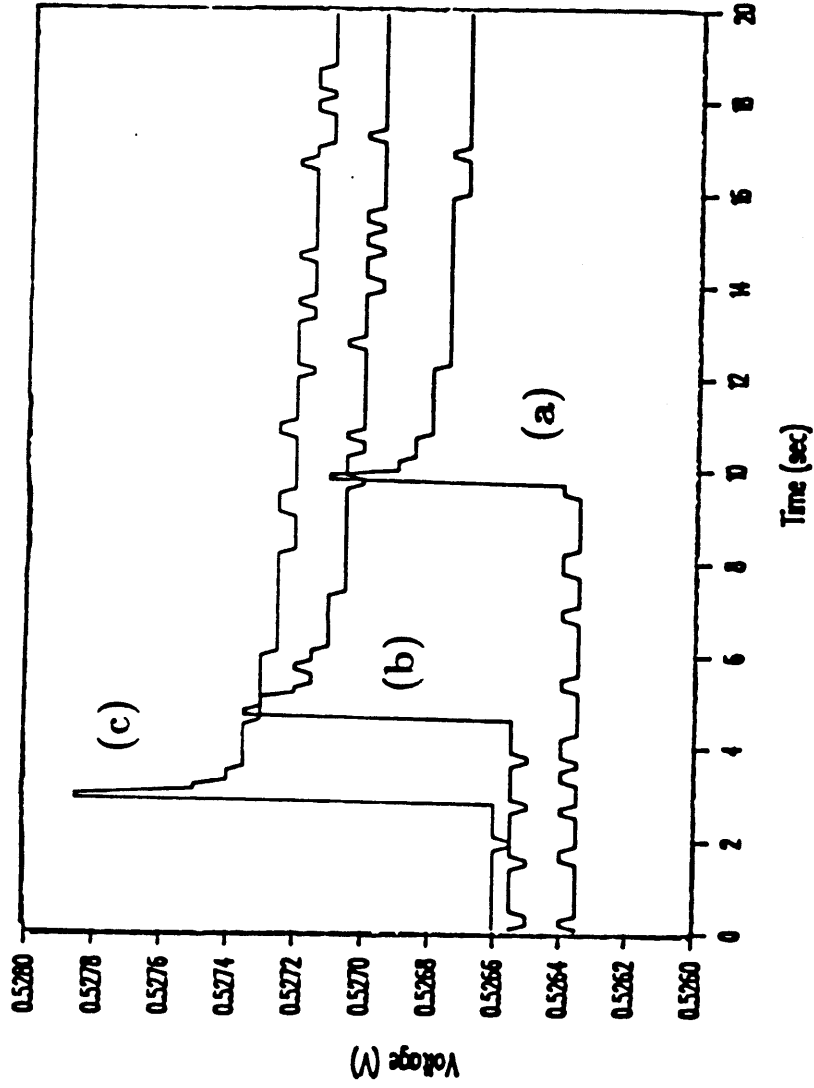


Figure 63. Plot of voltage drop across the load resistor vs. time for single pulse irradiation.

then the decay would be slow and consistent with the observed results.

In order to determine the sample conductance as a function of temperature, the substrate was heated inside the reactor and equilibrated at different temperatures and the conductance was recorded. A plot of sample conductance as a function of temperature is shown in Fig.64, which shows a maximum at about 170C. The observed conductance behavior was further examined by doing Hall mobility measurements at different temperatures. The electron mobility decreased with increasing temperature while the carrier concentration increased. Semiconductor electrical conductivity (σ) can be expressed as

$$\sigma = q(n\mu_n + p\mu_p) \quad (4.26)$$

where q is the electronic charge, n & p are the electron and hole concentration respectively and μ_i are their corresponding carrier mobilities. For $n \gg p$ (n-doped) samples, the above equation reduces to

$$\sigma = qn\mu_n \quad (4.27)$$

Going back to the observed conductivity behavior, below 170C, the carrier concentration increase was the dominant factor while above this temperature the mobility drop dominated the conductance of the semiconductor.

Laser CVD process requires the laser be operated at high pulse rates (20-50 Hz) in order to achieve high deposition rates. This necessitated conductivity measurements at different frequencies to determine the average heating behavior. The results obtained for a laser energy at different pulse rates is shown in Fig.65. The substrate was maintained at room temperature. At any laser frequency, the conductance increased and reached a steady state, and this steady state value changed with laser pulse rate for a particular energy. For frequencies ≥ 40 Hz,

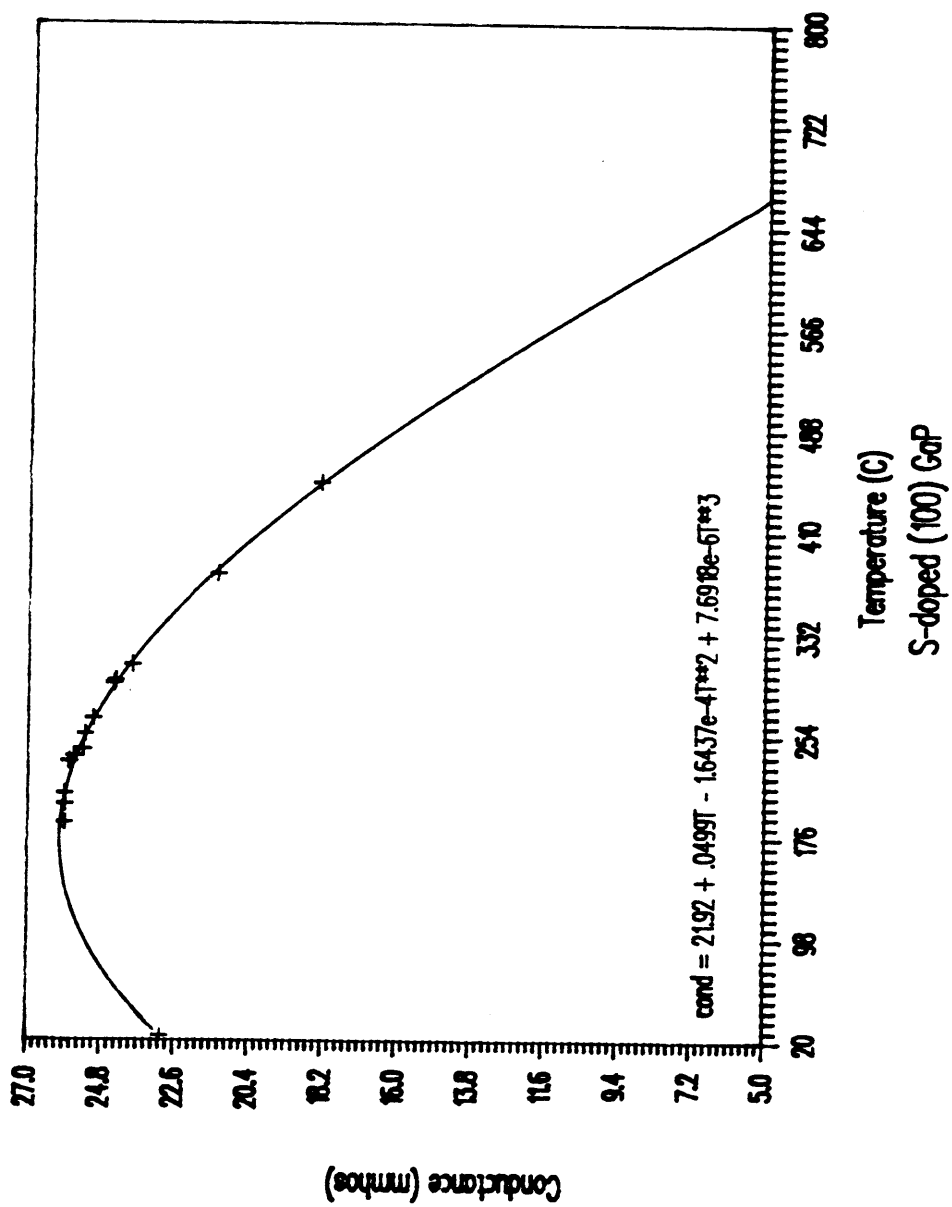


Figure 64. Conductance calibration curve.

the conductance increased, reached a peak before dropping to a steady state value. This behavior can be explained based on the change in conductance with temperature as shown in Fig.64. The average temperature rise due to continuous pulsing of the laser was obtained using Figs.64 & 65 with Fig.66 as the reference. This temperature is plotted as a function of laser pulse rate in Fig.65 and the importance of the laser pulsing rate in heating of the irradiated sample is quite obvious from this figure. This result is particularly interesting considering the fact that all the numerical and analytical pulsed laser heating models predict negligible or no temperature rise for periods more than 10^{-4} second after the laser pulse where as even for frequencies as low as 5 Hz, an average temperature rise was found.

It is evident that the semiconductor can be heated to a temperature as high as 250°C under steady state in vacuum despite the short duration of the laser pulse (15 nsec). The large increase in temperature for pulsing lasers is expected to be due to cumulative heating effect.

The substrate was heated to 160°C and experiments were conducted at different frequencies for the same pulse energy used for Fig.65. The conductivity of the semiconductor dropped, consistent with the decreasing conductivity above 170°C (Fig.67). However, the time taken to reach the steady state was much larger than that taken with the substrate at room temperature.

4.10.2.2 EFFECT OF GAS COOLING

It is fairly clear that there is a temperature rise with laser irradiation but this does not induce a CVD reaction since the above experiments were conducted in vacuum. So experiments were performed to study the heating behavior in the

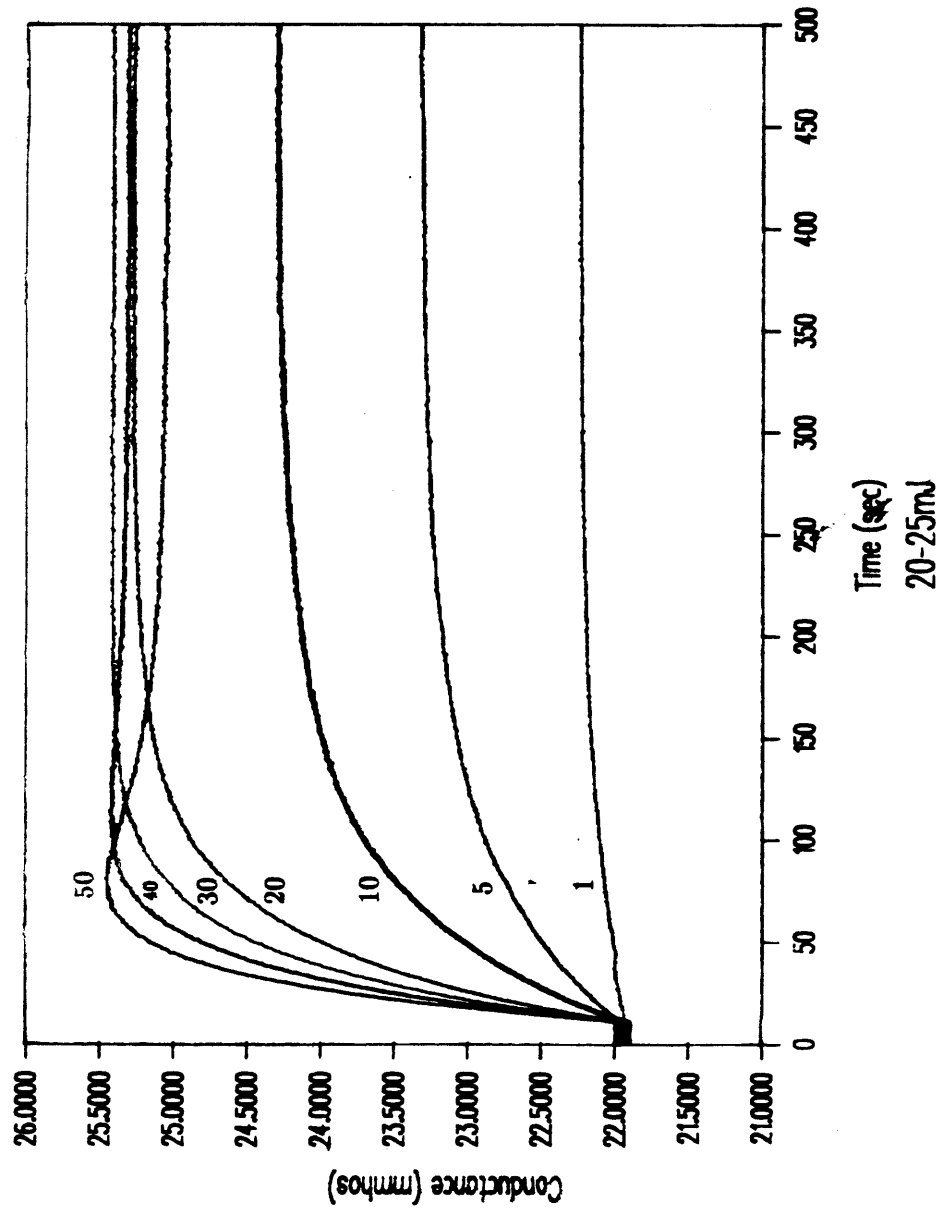


Figure 65. Plot of conductance vs. time for different laser pulse rates.

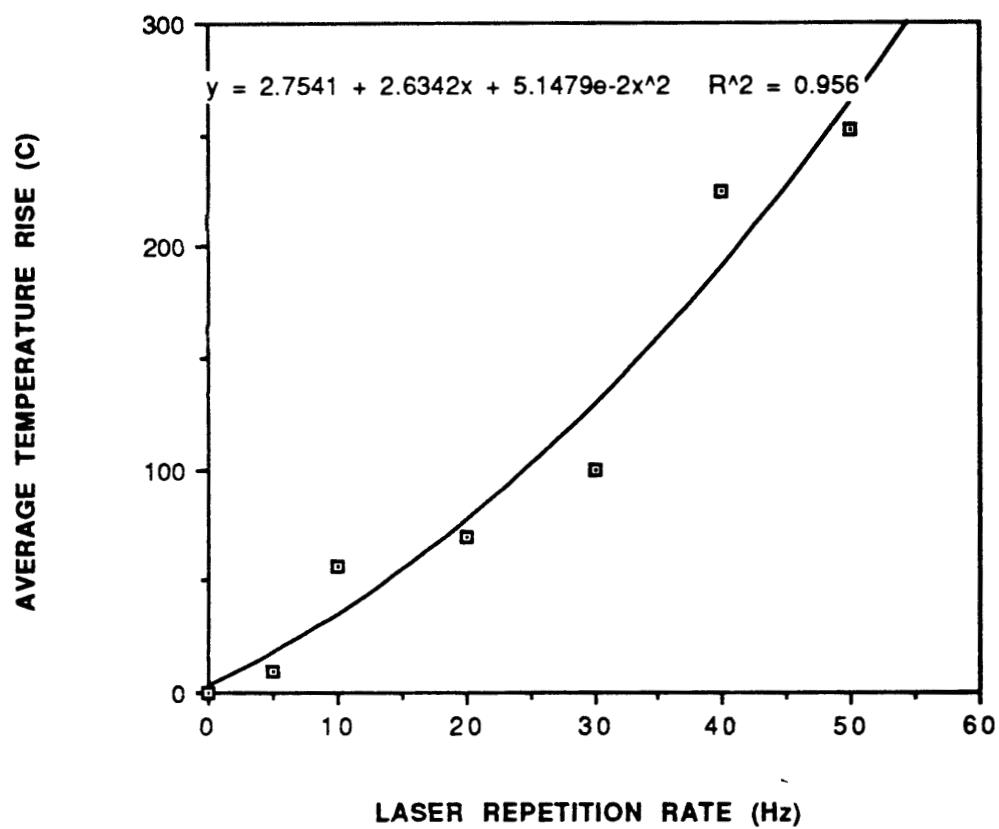


Figure 66. Plot of average temperature rise vs. laser pulse rate.

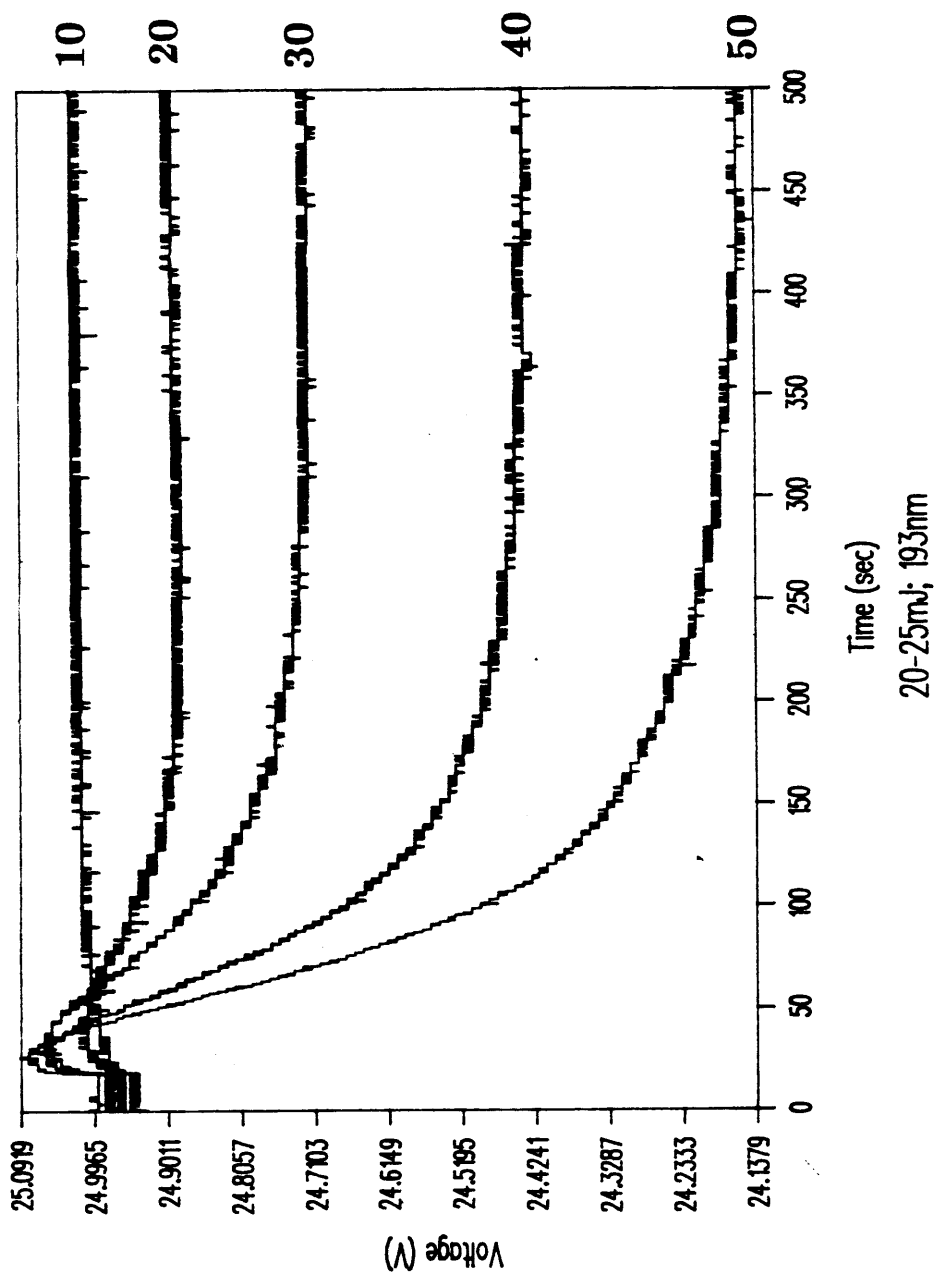


Figure 67. Plot of conductance of GaP at 190°C vs. time for different laser pulse rates.

presence of various gases. In the first set of experiments, after the conductance reached steady state, the laser was turned off and the sample was allowed to cool under two conditions; in vacuum and in the presence of flowing H_2 . The results are shown in Fig.68. It is clear that hydrogen cooling is much faster than the radiative cooling under vacuum.

The effect of He cooling at different reactor pressures was investigated as it was relevant to our investigation (refer chapter 4.5.3). Helium was flowed at different rates to achieve desired pressure before the laser was turned on. For constant laser energy and pulse rate, different steady state conductance values were achieved (Fig.69). It is evident that conductive cooling becomes a significant factor even for very low reactor pressure. However, for higher pressures the change in the cooling behavior is not very significant.

4.10.2.3 COMPARISON BETWEEN He AND H_2 COOLING

Helium is transparent to 103nm while H_2 is known to absorb weakly at this wavelength (77). More importantly, H_2 is a better thermal conductor than He (thermal conductivity difference, $(\Delta K=86 \times 10^{-6} \text{ Cal}/(\text{sec})(\text{cm}^2)(^\circ\text{C}/\text{cm}))$) which means that cooling effect due to H_2 should be more efficient than that by He. In order to investigate this, two experiments were performed in which same amount of the gases were flowed with the laser operating at a particular energy (30 mJ) and pulse rate (40 Hz). In case of He, (Fig.70), there was a sharp rise in the conductance followed by a steady state. However, for H_2 , the initial rise was about half the value reached in the presence of He. Also it was followed by a second region that showed a constant increase in conductance. If the thermal conductivity difference is the only factor, then H_2 (case) should have shown a behavior

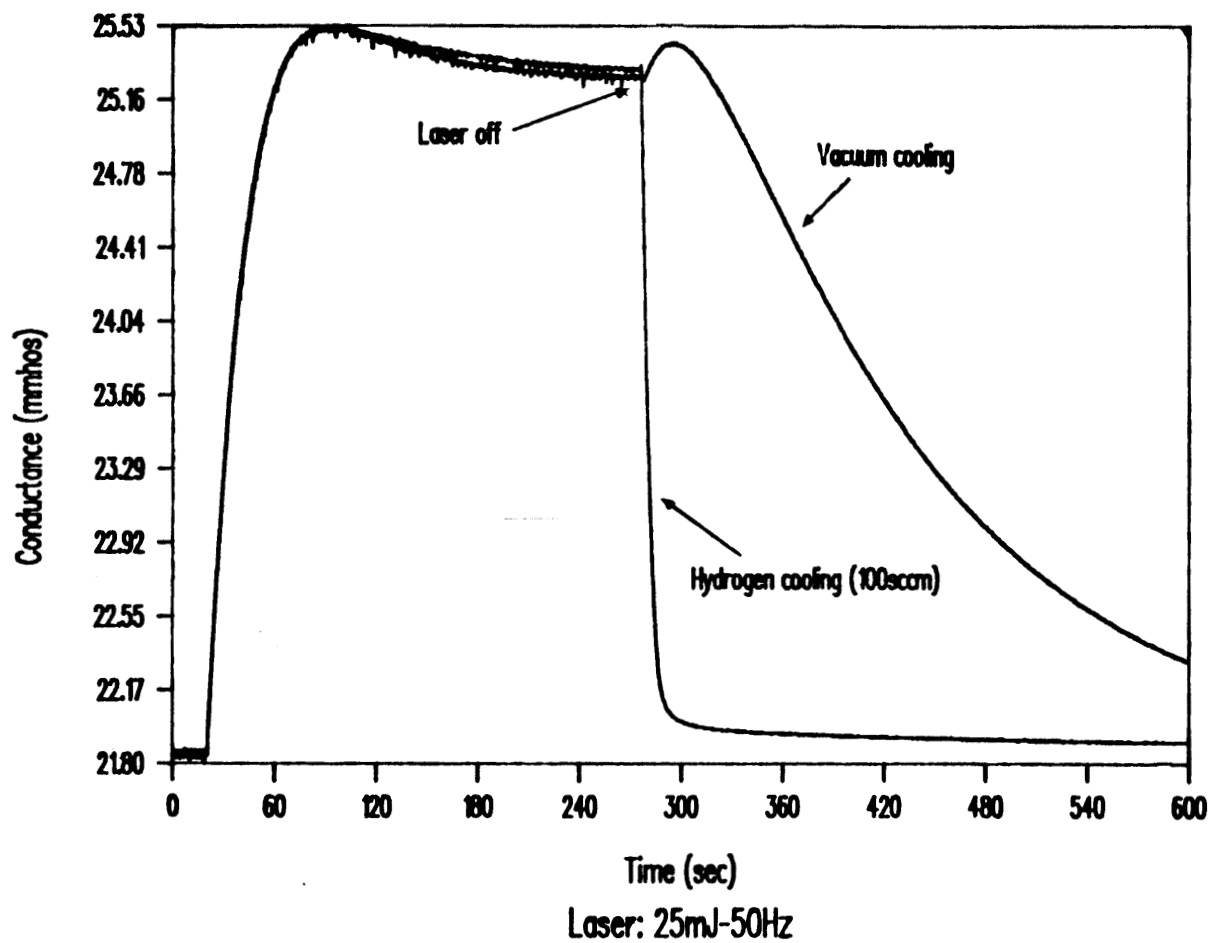


Figure 68. Effect of hydrogen cooling on GaP conductance.

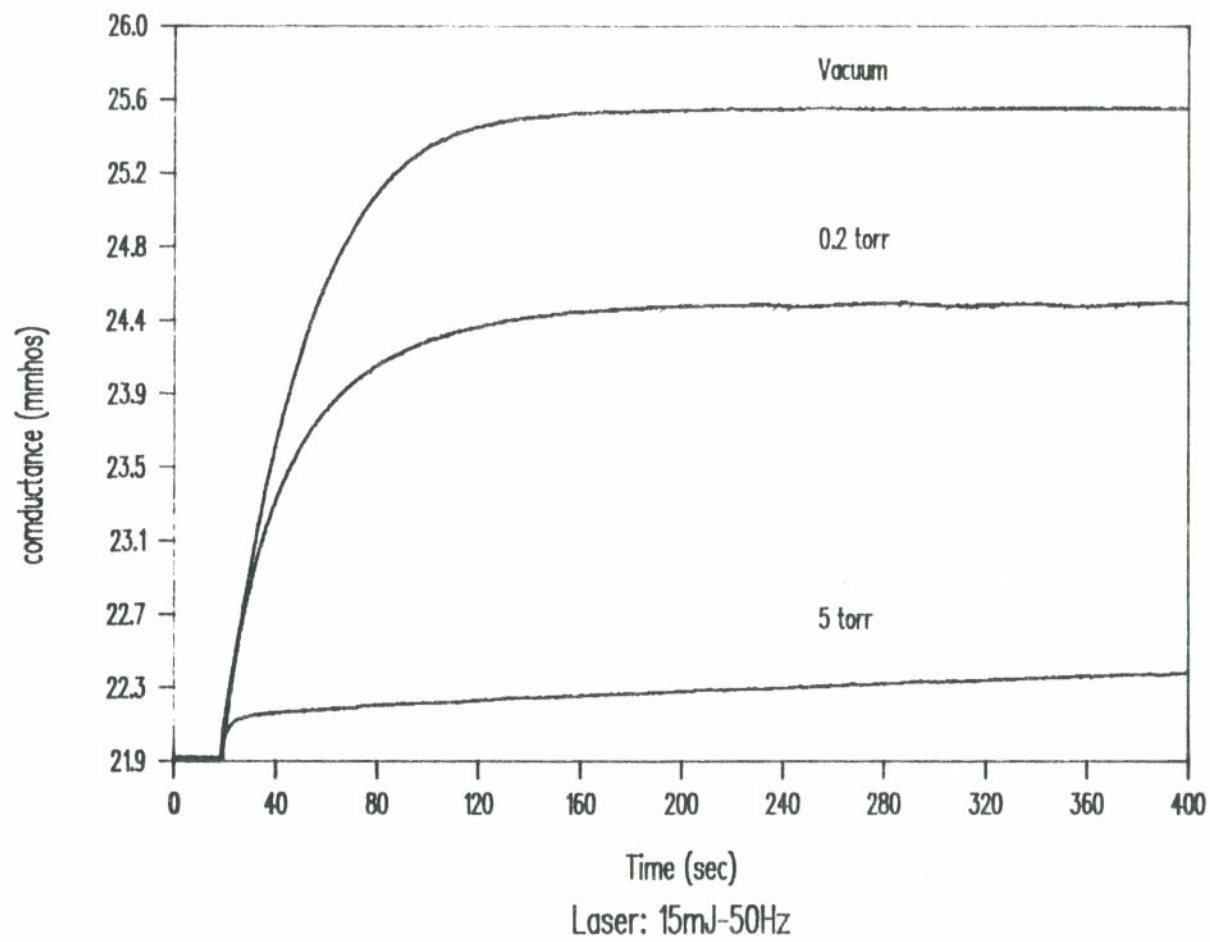


Figure 69. Effect of helium cooling on GaP conductance at different chamber pressures.

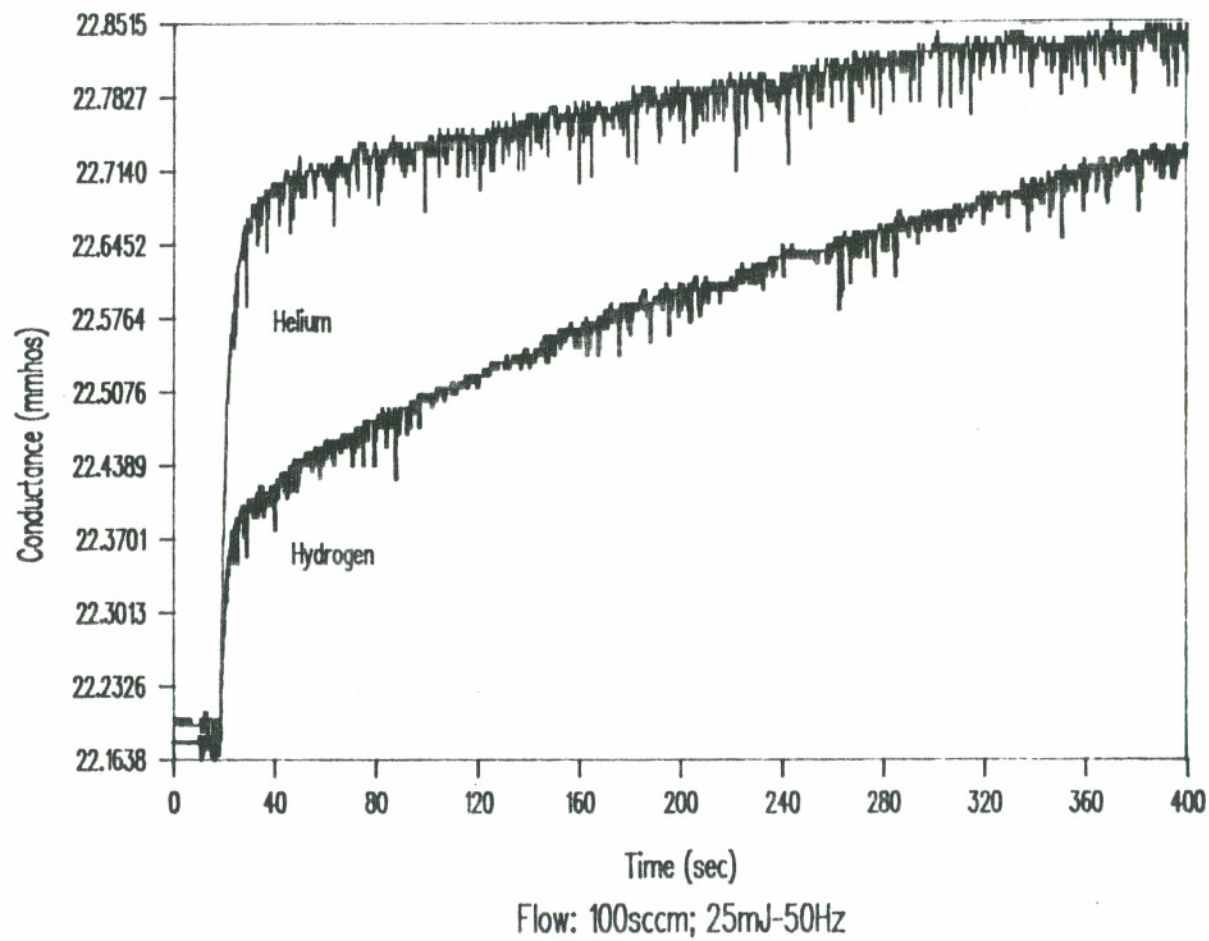


Figure 70. Comparison of hydrogen and helium cooling of GaP.

similar to that observed for He. Presently it is not clear why the conductance behavior is different in the presence of H_2 .

4.10.2.4 EFFECT OF TBP AND TMG (GASES THAT ABSORB 193nm STRONGLY)

Experiments were conducted for three different gas flows that were typical in the VPE process used for growing GaP. All the experiments were conducted at room temperature. The results are shown in Fig.71 and the gas flows are indicated below.

1. H_2 : 327sccm (manifold) + 100sccm (window)
2. H_2 : 303 sccm (manifold) + 100sccm (window)
 H_2 bubbled through TBP(5°C): 24sccm
3. H_2 : 300 sccm (manifold) + 100sccm (window)
 H_2 bubbled through TBP(5°C): 24sccm
 H_2 bubbled through TMG (-15°C): 3sccm

Condition 3 is the gas flow used in a typical growth experiment. With either TBP or TMG+TBP, the secondary region showing an increase in conductance with time was absent. TMG is known to absorb at 193nm very strongly and TBP also absorbs at this wavelength resulting in photo-dissociation. It is possible that a decrease in photon flux in the presence of the precursor gases has resulted in a decrease in substrate heating and It is possible that this technique, if properly used can give insights into the relative absorption characteristics of different metallorganic gases.

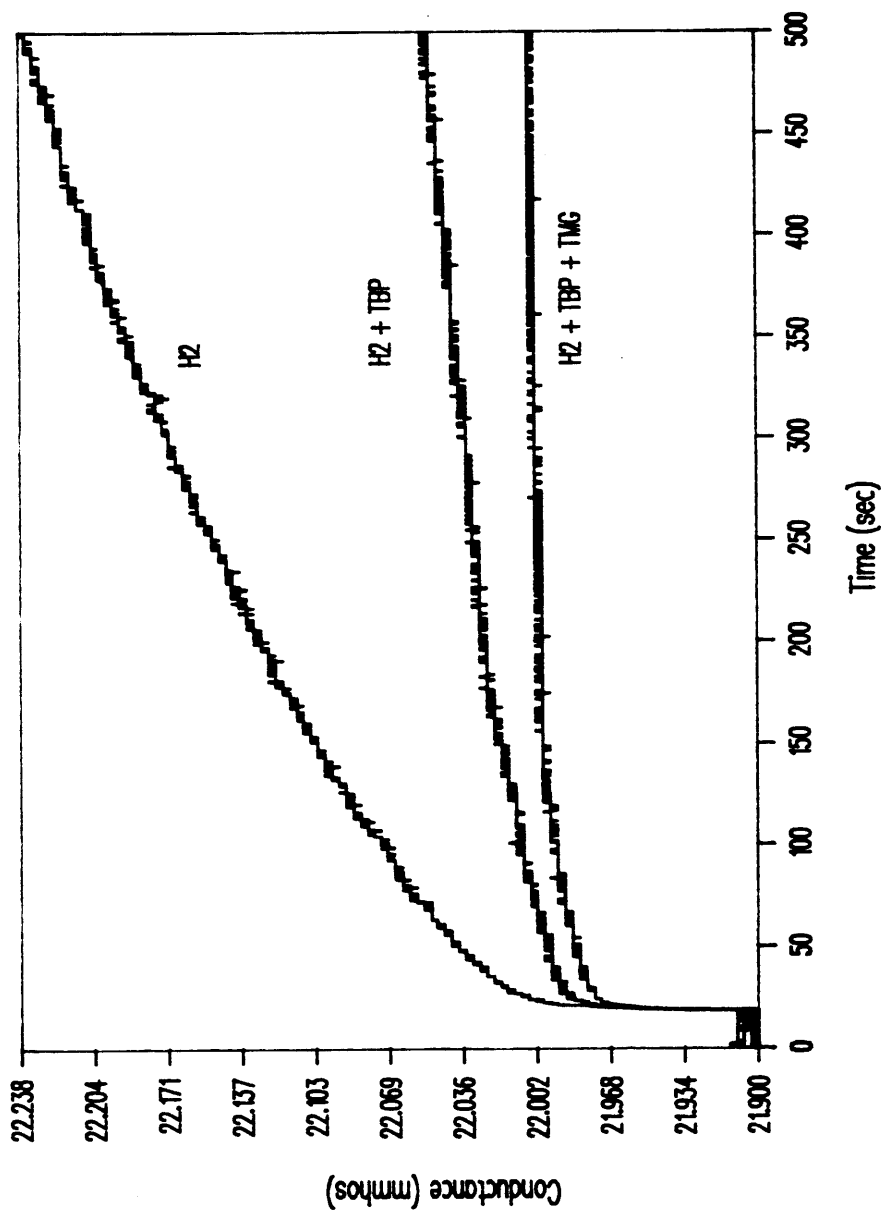


Figure 71. Comparison of presence of hydrogen, hydrogen + TBP, and hydrogen + TBP + TMG on GaP conductance

4.10.3 SUMMARY

1. In the absence of any gases, appreciable heating ($= 250^{\circ}\text{C}$) could be seen during the pulsed laser irradiation.
2. Very low quantity of gases seem to cool the substrate substantially during pulsed laser-semiconductor interaction. This suggests that average temperature rise is not an important factor in the temperature calculations used in the present investigation. The cooling effect saturates after a particular pressure is reached.
3. Cooling behavior of H_2 is different from that of He.
4. Conductance change behavior in the presence of gases (TMG) that strongly absorb at 193nm is definitely different from those that do not absorb strongly (H_2).

4.10.4 CONDUCTANCE MEASUREMENT AT ZERO BIAS

All the experiments described in the previous section were conducted with a constant bias of 0.5V. In this section, the results obtained for zero external bias are presented. The voltage drop across the sample was monitored at room temperature in an initially evacuated chamber.

As the laser was turned on, there was a sharp increase in the voltage drop across the sample (region II in Fig.72). When 100 sccm of helium was introduced through the manifold, there was a momentary drop in the voltage drop before it recovered to reach a steady state value (region III). When the He was turned off, the voltage increased back to the value corresponding to region II. When the laser was turned off, the voltage dropped back to zero and the response was very fast compared to the slow decay times observed in the conductivity

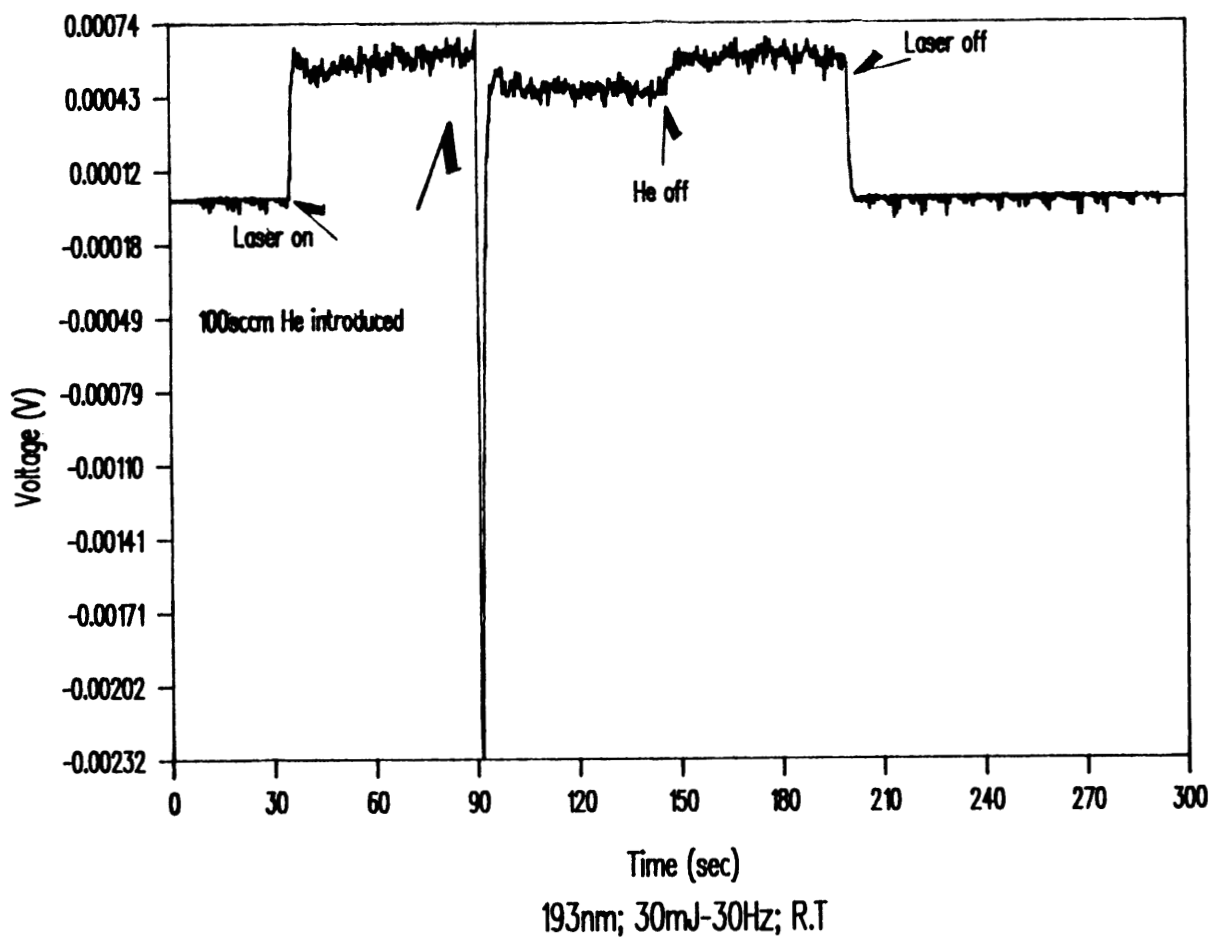


Figure 72. Effect of helium window purge at zero bias.

measurements in the presence of an external bias (Fig.68).

4.10.4.1 OTHER OBSERVATIONS

1. When the substrate was heated in the absence of laser irradiation, the voltage drop across the sample was increasingly negative and linear.
2. Voltage drop across the sample increased with increasing laser energy density (Fig.73).
3. For a constant power density, voltage drop across the sample increased linearly with the frequency of the laser (Fig.74).
4. With increasing substrate temperature, the voltage drop decreased for same input energy and frequency (Fig.75).

4.10.4.2 POSSIBLE MECHANISMS FOR VOLTAGE

GENERATION UNDER ZERO BIAS

SEEBECK EFFECT (78)

When a heated contact is applied to a semiconductor, a non-zero temperature gradient is established within the material. This gradient leads to a non-symmetrical rearrangement of majority and minority carriers. A space charge is established and consequently an electric field that eventually halts further rearrangement of carriers. It is the potential drop across this region of non-zero electric field which is measured and alternatively referred to as a thermoelectric or Seebeck voltage. Such a voltage generation is quite possible in the above measurements since the laser beam heats only a part of the semiconductor. Seebeck voltage can be estimated from the relation

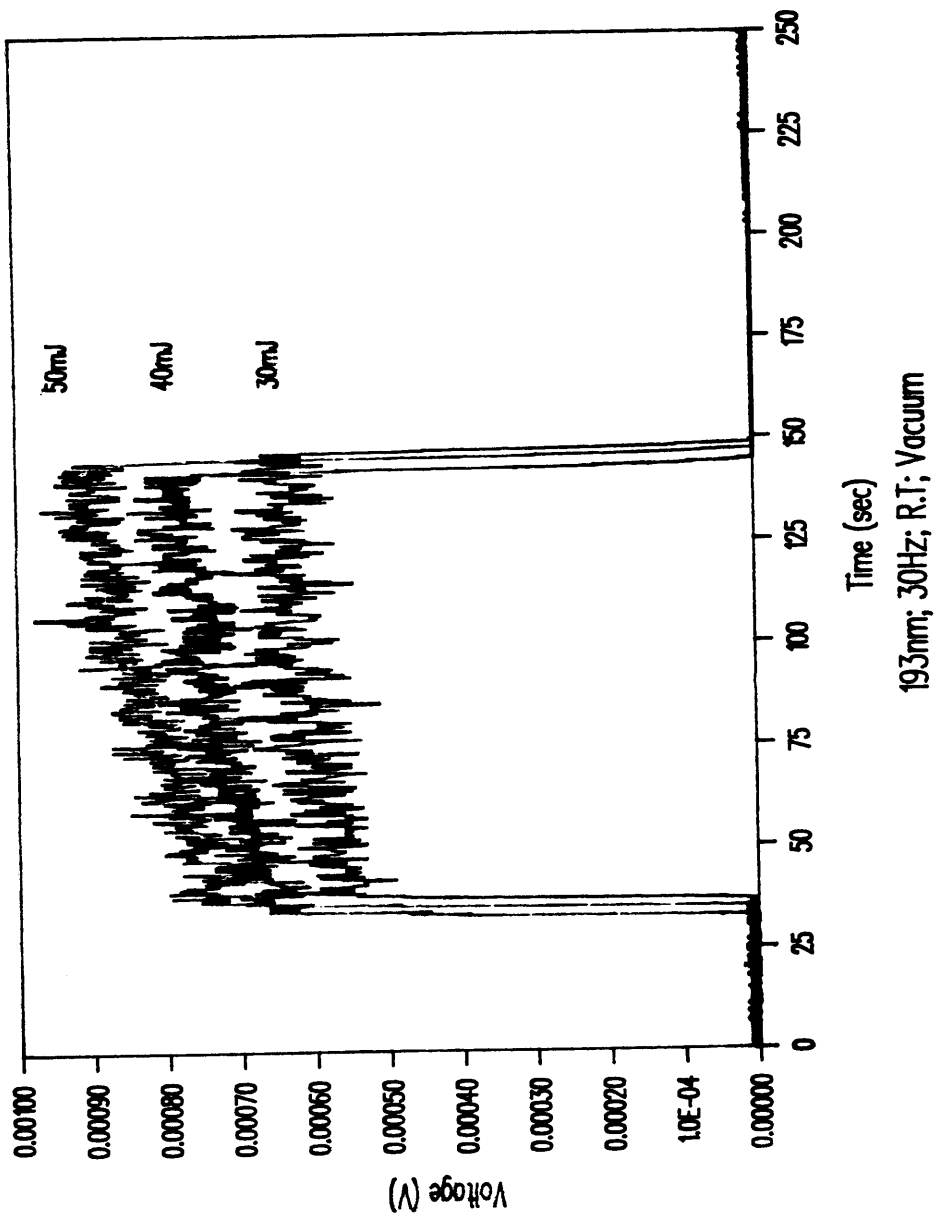
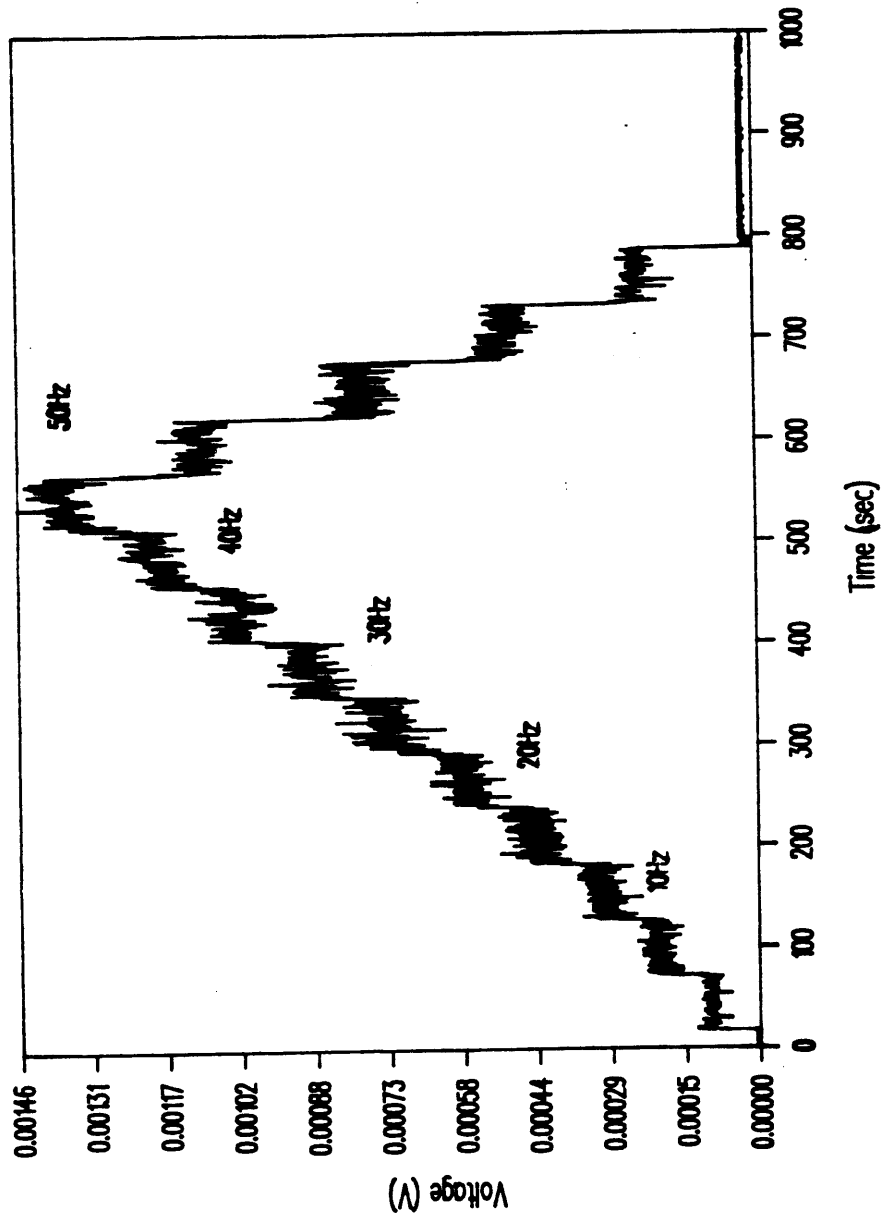
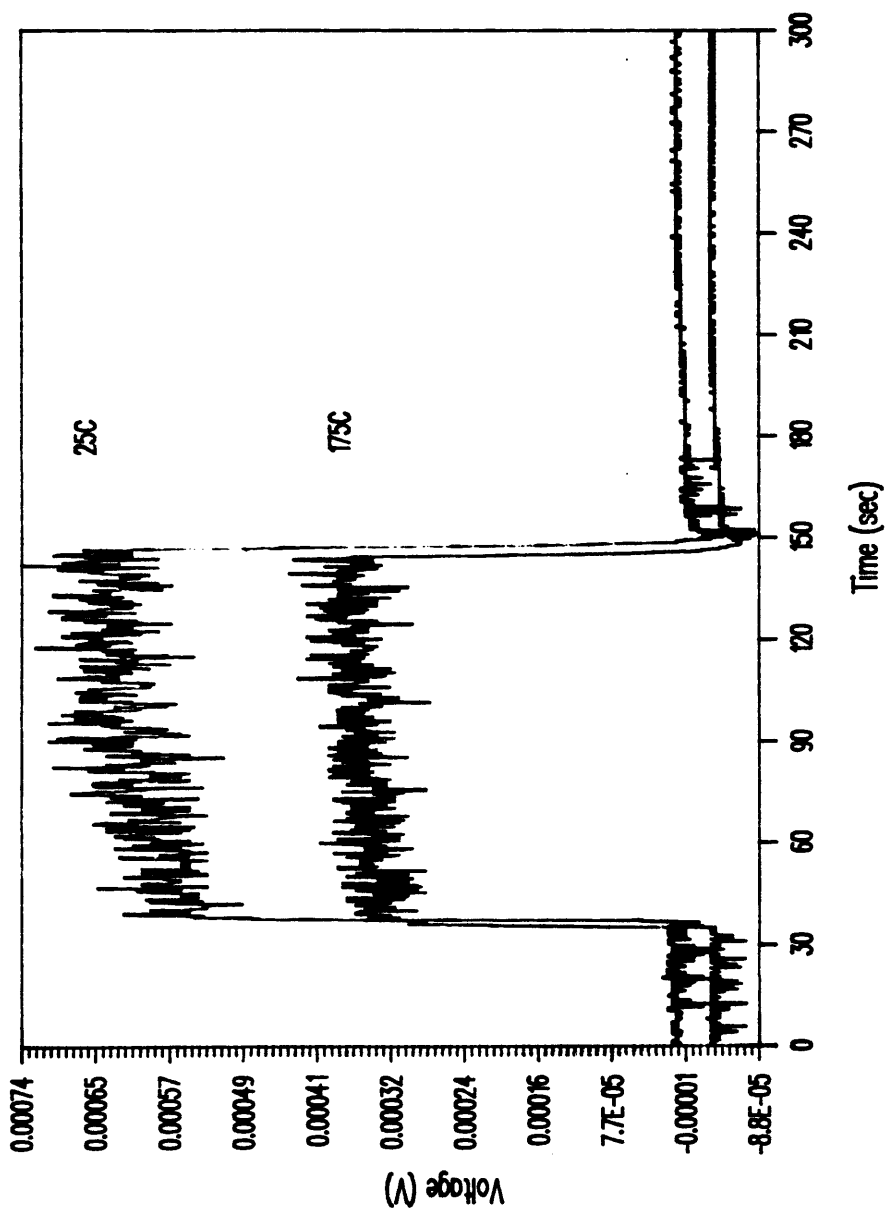


Figure 73. Effect of laser energy density at zero bias.



193nm; 30mj; Room temperature; vacuum

Figure 74. Effect of laser pulse rate at zero bias.



193nm; 30mJ-30Hz; Vacuum; Zero bias

Figure 75. Effect of substrate temperature at zero bias.

$$P = -k/e \left[(n\mu_n(5/2-S) + \ln(N_c/n)) - p\mu_p((5/2-S') + \ln(N_v/p)) \right] / (n\mu_n + p\mu_p)$$

where k is the Boltzman constant, N_c and N_v are density of states of the conduction and valence bands. For a semiconductor,

$$N_c = 4.83 \times 10^{15} (Tm_c/m_o) \text{ cm}^{-3} \quad (4.29)$$

For GaP, $N_c = 5.2 \times 10^{18} \text{ cm}^{-3}$

From Hall measurements, $n = 3 \times 10^{16} \text{ cm}^{-3}$

Also since $n \gg p$ (n-doped sample),

$$P = 8.6 \times 10^{-5} (5/2 + \ln N_c/n) V/^\circ C \quad (4.30)$$

$$P = 6.58 \times 10^{-4} V/^\circ C \quad (4.31)$$

According to the above expression, the observed voltage drop corresponds to a temperature rise of few tens of degrees, whereas the conductivity measurements in the presence of an external bias clearly indicated a much larger change in the average temperature. So it is not clear, if the observed change in voltage is due to a Seebeck effect. The other possibility is due to generation of a photovoltage. This again unlikely because of the large time scales involved in the data collection (50 msec) process compared to that of the laser pulse width (15 nsec).

DEMBER VOLTAGE (76)

Under UV laser irradiation on a substrate which is not biased, a photovoltaic voltage is induced due to a change in the carrier concentration Δn . This voltage is called Dember voltage and is represented by

$$V_D = kT/q (b-1)/(b+1) \ln \left[1 + (b+1)\Delta n / (bn_o + p_o) \right] \quad (4.32)$$

where k is the Boltzman constant. T is the temperature in K, q is the charge and 'b' is the ratio of electron to hole mobility. For GaP, 'b' is about 1.25 and

$V_D |_{\max}$ from the present experiments is about 1.46×10^{-3} V. For this voltage, the carrier concentration change (Δn) is about 10^{16} which is comparable to the carrier concentration due to doping itself. What is expected is a large change in the carrier concentration for a duration comparable to the laser pulse width (15nsec). However, this effect could not be detected due to the large time scales involved in the present experiments.

5 CONCLUSION

Laser-assisted selective area epitaxial growth of a compound semiconductor has been demonstrated using two different processes. Results from these two techniques are summarized below.

1. In the argon ion laser-assisted processing, the growth rate was found to change with increasing thickness of the gaussian shaped deposits. Also, multiple scanning of the laser was found to be necessary for obtaining thick deposits. This meant a low throughput and in order to achieve large scale selective area processing, the use of excimer laser was examined.
2. In the excimer laser-assisted processing crystallinity of GaP and the growth rate were found to be critically dependent on the laser power, pulse rate, substrate temperature and system pressure.
3. Irradiation of ArF laser onto the substrate during growth improved the crystalline quality of the deposit to a single crystal and enhanced the growth rate by a factor of 6 at substrate temperatures of 500°C.
4. Zinc doping of the deposit during growth resulted in concentration around 10^{20} cm^{-3} . C-V analysis yielded a straight line indicating that the junction was abrupt. I-V analysis showed the presence of tunneling current both in the forward and reverse bias.

5. Transmission electron microscopic analysis of homoepitaxial GaP and heteroepitaxial GaP on GaAs showed the presence of a large density of twins in the latter. This was attributed to the presence of stress, induced because of the differential plastic deformation of GaP layer and GaAs substrate during heteroepitaxy.
6. Heteroepitaxial GaP on GaAs showed the presence of strong periodic structures on the surface despite the poor polarization of the laser beam. The periodicity was about the wavelength of the laser photons. However, such ripples were not prominent on the homoepitaxial GaP. The presence of ripples on the heteroepitaxial GaP is attributed to localized periodic melting of the GaAs substrate during the initial stages of the growth. Such melting was less likely to occur on the GaP substrate because of its high melting threshold.
7. An average temperature rise as high as 280°C was observed during pulsed laser irradiation of GaP in vacuum. However, in the presence of gases, the average heating was found to be negligible. This implied that the substrate was indeed at relatively low temperatures during the duration in-between pulses.

6. FUTURE WORK

Laser-assisted processing of compound semiconductors offered several challenges during the course of present investigation. In the argon ion-assisted 'direct-write' process, the main limitation was the low throughput. However, mask projection of patterns is a possibility if an expanded continuous wave UV output from an argon ion laser (for example the frequency doubled 247nm) is used as the photon source to achieve high throughput selective epitaxy. However, the use of a low power cw UV laser necessitates higher substrate temperatures because of low thermal contribution from such sources. Another limitation of the argon ion laser-assisted pyrolytic process was the decreasing growth rate with increasing thickness of the deposit. This is particularly significant for small spot sizes. However, the problem can be overcome by increasing the spot size of the laser for a particular laser power level to achieve an optimum surface temperature rise for the pyrolytic process to occur.

Controlling the excimer laser-assisted MOVPE was a critical task since there were both thermal and photolytic contributions from the laser. The present work investigated the optimum parameters required for growth of homoepitaxial GaP. In terms of selective epitaxial growth, few attempts were made to achieve epitaxy of fairly large areas (1mm diameter) using contact masks. This area is open to investigation using more elaborate optical systems and mask sets.

At the optimum operating conditions, theoretical calculations indicated a high temperature rise in both the substrate and the film for very short duration by the pulsing laser to a depth of about $1\mu\text{m}$ from the surface. This had profound implications in the heteroepitaxy of GaP on GaAs. Differences in plastic

deformation characteristics of the substrate and the thin film can lead to large density of defects in the epitaxial layer. It makes the investigator wonder if the process is truly a low temperature process or just a pseudo-low temperature process. The usefulness of the process as a low temperature technique has to be tested in the heteroepitaxial growth compound semiconductors on silicon since any reduction in the growth temperature can lead to a reduction in stresses induced because of thermal expansion coefficient mismatch between the thin film and silicon substrate. Also, when the laser is parallel to the substrate, the unwanted rapid heating and cooling cycles can be avoided and at the same time use the UV source to photodissociate the precursor gases. This configuration can again reduce the growth temperature, however, the spatial selectivity of the process is lost.

Heteroepitaxial GaP on GaAs showed ripple-like surface. Periodic structures formed during laser assisted epitaxial growth can be employed for fabrication of optoelectronic devices that require grating structures (e.g. distributed feedback lasers). This could be achieved with a modified MOVPE reactor that allows excimer laser radiation at the growth region. Whenever periodic structures are required, the laser could be turned on during growth cycle. The periodicity could be controlled with proper selection of laser wavelength and the angle of incidence.

The average temperature of the GaP substrate during pulsed laser irradiation was investigated by monitoring its electrical conductance. The time scales involved in the measurements precluded any observation of the transient effects during the laser irradiation itself. Experiments can be designed to study such effects. For that purpose, instead of using a GaP substrate, a polysilicon thin

film (about 500-1000 Å which is about the thermal diffusion length) of a particular electrical conductivity on a silicon substrate of opposite conductivity with an intermediate silicon oxide layer is suggested. Such a geometry will give the true temperature rise during pulsed laser incidence. Caution must be taken to prevent any photoablation during laser irradiation. An alternate geometry is to use a P or N type silicon substrate with an ion-implanted thin region at/close the surface with opposite conductivity. In such a geometry, the oxide layer which is required in the polysilicon structure, can be eliminated. However, there is a possibility for dopant redistribution during laser annealing. This can pose problems in the reproducibility of the electrical conductance in the absence of laser irradiation.

REFERENCES

1. A. Yariv *Quantum Electronics*
1975, 2nd ed. John Wiley & sons, New York.
2. O. Svelto *Principles of Lasers* 1982 (D.C. Hanna, translator), Plenum Press,
New York
3. A.E. Siegman *An Introduction to Lasers and Masers* 1974, McCraw Hill,
New York
4. M.H. Hutchinson *Excimer Lasers in Tunable Lasers, in Topics Appl. Phys.*
Vol. 49 1987 (eds. L.F. Mollenauer and J.C. White) Springer-Verlog, New
York, p. 19-56.
5. Frank Wilkinson *Chemical Kinetics and Reaction Mechanisms* 1981, Van
Nostrand Reinhold Company Ltd., Berkshire, England
6. J.G. Eden, J.E. Greene, J.G. Osmundsen, D. Lubben, C.C. Abele, S. Gor-
batkin and H.D. Desai (1983).
"Semiconductor thin films grown by laser photolysis" *Mat. Res. Soc. Symp.*
Proc. 17, 185-192.
7. A. Ishitani, Y. Oshita, K. Tanigaki and K. Takada (1987) " Prebaking and
silicon epitaxial growth enhanced by UV radiation " *J. Appl. Phys.* **49**,
880-882.

8. N.H. Karam, H. Liu, I. Yoshida and S.M. Bediar (1988). " Direct writing of GaAs monolayers by laser-assisted atomic layer epitaxy " *Appl. Phys. Lett.* **52**, 1144-1146.
9. P. Balk, M. Fischer, D. Grundmann, R. Luckcrath, H. Luth and W. Richter (1987). " Ultraviolet-assisted growth of GaAs " *J. Vac. Sci. Technol.* **5**, 1453-1459.
10. A. Doi, Y. Aoyagi and S. Namba (1986). " Stepwise monolayer growth of GaAs by switched laser metallorganic vapor phase epitaxy " *Appl. Phys. Lett.* **49**, 785-787.
11. J. Kukimoto, Y. Ban, H. Komatsu, M. Takechi and M. Ishizaki (1986) " Selective area control of material properties in laser-assisted MOVPE of GaAs and AlGaAs " *J. Crystal Growth* **77**, 223-228.
12. D.W. Kisker and R.D. Feldman (1985) " Photon-assisted MOVPE growth of CdTe " *J. Crystal Growth* **72**, 102-107.
13. V.M. Donnelly, D. Brasen, A. Appelbaum and M. Geva (1985). " Excimer laser-induced deposition of InP: Crystallographic and Mechanistic studies " *J. Appl. Phys.* **58**, 2022-2035.
14. S.J.C. Irvine, J. Giess, J.S. Gough, G.W. Blackmore, A. Royle, J.B. Mullin, N.G. Chew and A.G. Cullis (1986). " The potential for abrupt interfaces in $\text{Cd}_x\text{Hg}_{1-x}\text{Te}$ using thermal and photo-MOVPE " *J. Crystal Growth* **77**, 437-451.
15. B.J. Morris (1986). " Photochemical organometallic vapor phase epitaxy of mercury cadmium telluride " *Appl. Phys. Lett.* **48**, 867-869.

16. R.N. Bicknell, N.C. Giles and J.G. Schetzina (1986). " Growth of high mobility n-type CdTe by photoassisted molecular beam epitaxy " *Appl. Phys. Lett.* **49**, 1095-1097.
17. W. Roth, H. Krautle, A. Krings and H. Beneking (1983). " Laser stimulated growth of epitaxial GaAs " *Mat. Res. Soc. Symp. Proc.* **Vol.17**, 193-198.
18. V.M. Donnelly, D. Brasen, A. Appelbaum and M. Geva (1986). " Excimer laser-induced deposition of InP " *J. Vac. Sci. Technol.* **A4**, 716-721.
19. R.F. Wood and G.E. Jellison (1984). " Melting model of pulsed laser processing " *Semiconductors and semimetals* **Vol. 23**, Academic Press Inc., Orlando.
20. M. von Allmen (1980). *Laser and Electron Beam Processing of Materials* p 6 (eds. C.W. White and P.S. Peercy) Academic Press, New York.
21. M.O. Thompson (1984). " Liquid-solid interface dynamics during pulsed laser melting of silicon on sapphire " Ph.D Thesis, Cornell University, Ithaca, New York.
22. M. Lax (1977). " Temperature rise induced by a laser beam " *J. Appl. Phys.* **48**, 3919-3924.
23. American Cyanamid, Application Note No.2
24. T.T. Sheng and R.B. Marcus (1980). " Advances in Transmission Electron Microscope Techniques Applied to Device Failure Analysis " *J. Electrochem Soc.* **127**, 737-743.
25. S.R.J. Brueck and D.J. Ehrlich (1982). " Stimulated surface-plasma-wave scattering and growth of a periodic structure in laser-photodeposited metal films " *Phy. Rev. Lett.* **48**, 1678-1681.

26. J.Y. Tsao and D.J. Ehrlich (1984). " UV-laser photodeposition from surface adsorbed mixtures of trimethylaluminum and titanium tetrachloride " *J. Chem. Phys.* **81**, 4620-4625.
27. T.H. Baum, C.E. Larson and R.L. Jackson (1989). " Laser-induced chemical vapor deposition of aluminum " *Appl. Phys. Lett.* **55**, 1264-1266.
28. T.H. Baum and C.R. Jones (1985). " Laser chemical vapor deposition of gold " *Appl. Phys. Lett.* **47**, 538-540.
29. J.B. Moylan, T.H. Baum and C.R. Jones (1986). " Laser CVD of copper: Deposition rates and deposit shapes " *Appl. Phys. A* **40**, 1-5.
30. D. Bauerle (1984). " Laser Processing and Diagnostics " (ed. D. Bauerle) *Springer Ser. Chem. Phys.* **39**, p.166.
31. P. Petzoldt, K. Piglmayer, W. Krauter and D. Bauerle (1984) " Lateral Growth rates in Laser CVD of Microstructures " *Appl. Phys. A* **35**, 155-159.
32. Y.S. Liu, C.P. Yakymyshyn, H.R. Philipp, H.S. Cole and L.M. Levinson (1985) " Laser-induced selective deposition of micron size structures on silicon " *J. Vac. Sci. Technol. B* **3**, 1441-1444.
33. D. Baerle, P. Irsigler, G. Leyendecker, H. Noll and D. Wagner (1982). " Ar⁺ laser induced chemical vapor deposition of Si from SiH₄ " *Appl. Phys. Lett.* **40**, 819-821.
34. S.K. Roy, A.S. Vengurlekar, V.T. Karulkar, A.V. Joshi and S. Chandrasekar (1987). " Characterization of Ar Ion Laser Induced CVD Silicon Films: Deposition, Crystallographic Texture and Phosphorous doping " *J. Elect. Mat.* **16**, 211-217.

35. H.H. Gilson, T. Cacouris, P.S. Shaw, R.R. Krchnavek and R.M. Osgood (1987) " Direct writing of metal conductors with near-UV light " *Appl. Phys.* **B42**, 55-66.
36. V.M. McCrary and V.M. Donnelly (1987). " The ultraviolet absorption spectra of selected organometallic compounds used in the chemical vapor deposition of gallium arsenide " *J. Crystal Growth* **84**, 253-258.
37. V.M. Donnelly and J.A. McCaulley (1989). " Selected area growth of GaAs by laser-induced pyrolysis of adsorbed trimethylgallium " *Appl. Phys. Lett.* **54**, 2458-2460.
38. C.A. Larsen, N.I. Buchan and G.B. Stringfellow (1988). " Reaction mechanisms in the organometallic vapor phase epitaxial growth of GaAs " *Appl. Phys. Lett.* **52**, 480-482.
39. S.H. Li, C.A. Larsen, N.I. Buchan, G.B. Stringfellow, W.P. Kosar and D.W. Brown (1989). " Study of tertiarybutylphosphine pyrolysis using a deuterated source " *J. Appl. Phys.* **65**, 5161-5165.
40. Y. Zhang, Th. Beuermann and M. Stuke (1989). " UV laser photofragment GaCH_3 detected by far laser mass spectrometry " *Appl. Phys.* **B 48**, 97-100.
41. D.H. Lowndes and G.E. Jellison (1984). " Time resolved measurements during pulsed laser irradiation of silicon " *Semiconductors and Semimetals Vol. 23*, p. 313 (Academic Press, New York).
42. A.G. Evans, M.D. Drory and M.S. Hu (1988). " The cracking and decomposition of thin films " *J. Mat. Res.* **3**, 1043-1049.
43. X.D. Wu, A. Inam, T. Venkatesan, C.C. Chang, E.W. Chase, P. Barboux, J.M. Tarascon, and B. Wilkins (1988). *Appl. Phys. Lett.* **52**, 754.

44. V. Tavitian, C.J. Kiely, D.B. Geohegan and J.G. Eden (1988). " Epitaxial growth of Ge films on GaAs (285-415°C) by laser photochemical vapor deposition " *Appl. Phys. Lett.* **52**, 1710-1712.
45. S.M. Sze (1989). *Physics of Semiconductor Devices* p. 74 (Wiley Eastern Limited, New Delhi).
46. W. Shockley (1949). " The Theory of p-n Junctions in Semiconductors and p-n Junction Transistors " *Bell Syst. Tech. J.* **28**, 435-489.
47. E.G. Dierschke and G.L. Pearson (1970). " Forward and reverse tunnel currents in gallium phosphide diffused p-n junctions " *J. Appl. Phys.* **41**, 329-334.
48. D. Schechtman and I.A. Blech (1985). " The microstructure of rapidly quenched Al_0Mn " *Metall. Trans. A* **16**, 1005-1012.
49. L.A. Bendersky and F.S. Biancaneello (1987). " TEM observation of icosahedral, new crystalline and glassy phases in rapidly quenched Cd-Cu alloys " *Scripta Metal.* **21**, 531-536.
50. L. Pauling (1987). " So-called Icosahedral and Decagonal Quasicrystals are twins of an 820-atom cubic crystal " *Phys. Rev. Lett.* **58**, 365-368.
51. M.J. Carr (1986). " An analysis of five-fold symmetry by microtwinning in rapidly solidified Al-Mn alloys " *J. Appl. Phys.* **59**, 1063-1067.
52. K.S. Vecchio and D.B. Williams (1988). " Convergent beam electron diffraction analysis of the $T_1(Al_2CuLi)$ phase in Al-Li-Cu alloys " *Metall. Trans. A* **19**, 2875-2891.
53. H. Saito, J.O. Borland, H. Asaki, N. Nagai and K. Nawata (1983). " Hillock defects in InGaAs/InP multi-layers grown by MBE " *J. Crystal Growth* **64**

521-528.

54. P. Hirsch, A. Howie, R.B. Nicholson, D.W. Pashley and M.J. Whelan (1967). *Electron Microscopy of Thin Crystals* (Butterworths, London)
55. S.N.G. Chu, W.T. Tsang, T.H. Chiu and A.T. Macrander (1989) " Lattice-mismatch-generated dislocation structure and their confinement using superlattices in heteroepitaxial GaAs/InP and InP/GaAs grown by chemical beam epitaxy " *J. Appl. Phys.* **66**, 520-530
56. S.N.G. Chu, S. Nakahara, R.F. Karlicek, K.E. Strege, D. Mitcham and W.D. Johnston, Jr (1986). " Defect structure in III-V compound semiconductors: Generation and evolution of defect structures in InGaAs and InGaAsP epitaxial layers grown by hydride transport vapor-phase epitaxy " *J. Appl. Phys.* **59**, 3441-3447.
57. F. Ernst and P. Pirouz (1989). " The formation mechanism of planar defects in compound semiconductors grown epitaxially on {100} silicon substrates " *J. Mat. Res.* **4**, 834-842.
58. Ichiro Yonenaga and Koji Sumino (1989). " Mechanical properties and dislocation dynamics of GaP " *J. Mat. Res.* **4**, 355-365.
59. N.R. Isenor (1977). " CO₂ laser-produced ripple patterns on Ni_xP_{1-x} surfaces " *Appl. Phys. Lett.* **31**, 148-150.
60. F. Keilmann (1983). " Laser-driven corrugation instability of liquid-metal surfaces " *Phys. Rev. Lett.* **51**, 2097-2100.
61. I. Ursa, I.N. Mihailescu, A. Popa, A.M. Prokhorov, V.P. Ageev, A.A. Gorbunov and V.I. Konov (1985). " Studies of the change of a metallic surface microrelief as a result of multiple-pulse action of powerful UV laser pulses "

- J. Appl. Phys.* **58**, 3909-3913.
62. P.A. Temple and M.J. Soileau (1981). " Polarization charge model for laser-induced ripple patterns in dielectric materials " *IEEE J. Quant. Electron.* **QE-17**, 2067-2072.
 63. D.C. Emmony, R.P. Howson and L.J. Willis (1973). " Laser mirror damage in germanium at 10.6 μm " *Appl. Phys. Lett.* **23**, 598-600.
 64. H.J. Leamy, G.A. Rozgonyi, T.T. Sheng and G.K. Celler (1978), " Periodic regrowth phenomena produced by laser annealing of ion-implanted silicon " *Appl. Phys. Lett.* **32**, 535-537.
 65. G.N. Maracas, G.L. Harris, C.A. Lee and R.A. McFarlane (1978). " On the origin of periodic surface structure of laser-annealed semiconductors " *Appl. Phys. Lett.* **33**, 453-455.
 66. J.F. Young, J.E. Sipe and H.M. van Driel (1984). " Laser-induced periodic surface structure.III: Fluence regimes, the role of feedback, and details of the induced topography in germanium " *Phys. Rev. B* **30**, 2001-2015.
 67. I.W. Boyd, S.C. Moss, T.P. Howson and L.J. Willis (1984). " Various phase transitions and changes in surface morphology of crystalline silicon induced by 4-260 psec pulses of 1- μm radiation " *Appl. Phys. Lett.* **45**, 80-82.
 68. Z. Gouosheng, P.M. Fauchet and A.E. Siegman (1982). " Growth of spontaneous periodic surface structures on solids during laser illumination " *Phys. Rev. B* **26**, 5366-5381.
 69. S.E. Clark and D.C. Emmony (1989). " Ultraviolet-laser induced periodic surface structures " *Phys. Rev. B* **40**, 2031-2041.

70. V.I. Emel'yanov, V.I. Konov, V.N. Tokarev and V.N. Seminogov (1989).
" Formation of periodic surface ripples under the action of pulsed carbon dioxide laser radiation on fused silica " *J. Opt. Soc. Am.* **B 6**, 104-114.
71. C.J. Chen and R.M. Osgood (1983). " Direct observation of the local-field-enhanced surface photochemical reactions " *Phys. Rev. Lett.* **50**, 1705-1708.
72. F.A. Houle, C.R. Jones, T.H. Baum, C. Pico and C.A. Kovac (1985).
" Laser chemical vapor deposition of copper " *Appl. Phys. Lett.* **46**, 204-206.
73. R.J. Wilson and F.A. Houle (1985). " Composition, structure and electric field variations in photodeposition " *Phys. Rev. Lett.* **55**, 2184-2187.
74. V.R. McCrary, V.M. Donnelly, D. Brasen, A. Appelbaum and R.C. Farrow (1986). " Characterization of excimer laser deposited GaAs films from the photolysis of trimethylgallium and trimethylarsine at 193nm " *Mat. Res. Soc. Symp. Proc.*
75. Ellen J. Yoffa (1980). " Dynamics of dense laser-induced plasmas " *Phys. Rev.* **B 21**, 2415-2425.
76. Jacques I. Pankove *Optical Processes in Semiconductors* 1975, Dover Publications, New York.

8. BIOGRAPHICAL NOTE

The author was born on 31 January 1961, in Madurai, India. He graduated from T.V.S High School in 1977. He pursued one year of Pre-University at Sourashtra College before joining Thiagarajar College of Engineering where he received a Bachelor of Science degree in Applied Sciences in 1981.

The author joined Indian Institute of Science in 1981 to study metallurgy. He received a Bachelor of Engineering in metallurgy in 1984. The author came to Oregon Graduate Center in 1985 and completed all requirements for the Doctor of Philosophy degree in Materials Science in April 1990. He is leaving to accept a process engineering position at Tektronix, Portland.